

CONFINEMENT AND TEXTURE IN CEMENT HYDRATES: FROM NANOSCALE
COHESION TO RHEOLOGY

A Dissertation
submitted to the Faculty of the
Graduate School of Arts and Sciences
of Georgetown University
in partial fulfillment of the requirements for the
degree of
Doctor of Philosophy
in Physics

By

Abhay Goyal, M.S.

Washington, DC
April 15, 2020

Copyright © 2020 by Abhay Goyal
All Rights Reserved

CONFINEMENT AND TEXTURE IN CEMENT HYDRATES: FROM NANOSCALE COHESION TO RHEOLOGY

Abhay Goyal, M.S.

Dissertation Advisor: Emanuela Del Gado, Ph.D.

ABSTRACT

Concrete is the most abundant artificial material on Earth, yet the physical mechanisms that control its properties are not fully understood. Cement, the main binding agent, reacts with water to produce Calcium-Silicate-Hydrate (C-S-H) nanoparticles that form a heterogeneous and porous gel which serves as the glue for the hardened material. The C-S-H building blocks are highly charged and adhere due to electrostatics mediated by the water and counter-ions produced by cement dissolution. This multiscale complexity, coupled to the non-equilibrium setting process, is the central challenge to designing better cementitious materials—for more durable infrastructure, reduced emissions and improved sustainability, and 3D printing based construction. To address this, I have developed nano- and meso-scale computational models, connecting cement chemistry to its nanoscale cohesion and the consequential effects on microstructure and macroscopic material properties.

The electrostatics governing cohesion of C-S-H nanoparticles is in the regime (strongly coupled i.e multivalent ions and high surface charge density) where the usual mean-field theories break down and a new approach is needed. By modeling explicit ions, immersed in SPC/E water, confined by charged surfaces, I demonstrate that strong spatial and dynamic correlations arise between ions and water which are responsible for the strong net attraction between the confining surfaces. This depends on surface charge and ion type, controlled by the cement chemistry, which changes over time. Coarse-graining to the mesoscale, I translate the nanoscale forces to an effective interaction between C-S-H particles. By coupling

molecular dynamics with a Grand Canonical Monte Carlo process to mimic C-S-H precipitation, I investigate the heterogeneous C-S-H growth near cement grain surfaces. These simulations demonstrate how the time-evolution of the interactions can drive the formation of a percolating gel, which limits spatial gradients and anisotropy at early hydration times but reaches high densities with large local variations—as in hardened cement pastes—at later times. Together, these models provide a framework for predicting the nanoscale electrostatics, mesoscale morphology, and macroscopic properties of cement from first principles, and I discuss how this could be applied to make predictions of rheological properties.

INDEX WORDS: multiscale modeling, electrostatics, coarse-grained model, soft matter physics, molecular dynamics, Grand Canonical Monte Carlo, percolation, dynamic correlations, virial stresses, local ordering, scattering, rheology, porous materials

DEDICATION

This thesis is dedicated to my parents, Drs. Sanjay and Madhulika Goyal.

ACKNOWLEDGMENTS

This thesis would not have been possible without the help of many individuals.

First and foremost, I would like to thank my advisor, Emanuela Del Gado, from whom I have learned so much over these past years. Her contribution to my PhD experience and work cannot be overstated.

I would also like to thank all of my collaborators over the years, who have stimulated my exploration of interesting scientific questions and helped me start my research journey. In particular, Katerina Ioannidou and Roland Pellenq have played an important role in my research from the start. Since then, Ivan Palaia, Jetin Thomas, Francis Dragulet, Scott Jones, Nick Martys, Deshpreet Bedi, Pierre Levitz, Emmanuel Trizac, Abhinendra Singh, Bulbul Chakraborty, Franz Ulm, and Henri Van Damme have all contributed.

I would like to thank my committee members, Dan Blair, Toshiko Ichiye, Amy Liu, and Roland Pellenq.

Over the years, all the faculty and students of the Georgetown physics department have taught me a great deal through classes, discussions, and seminars, and my friends, in DC and NY, have helped me stay grounded during this time. So thanks to all of you.

Finally, I have to thank my family, Sanjay, Madhu, and Anchal, for making me who I am and putting up with me.

TABLE OF CONTENTS

Introduction	1
1 Cement and physics	4
1.1 What is cement?	4
1.2 Calcium-Silicate-Hydrates	6
1.3 Electrostatics in solution	10
1.4 A non-equilibrium mesoscale model	20
1.5 Summary	25
2 Calcium-Silicate-Hydrate gelation and microstructure	26
2.1 The model	27
2.2 Simulation details	30
2.3 Clusters and percolation	32
2.4 Porosity	40
2.5 Specific surface area	43
2.6 Scattering	46
2.7 Conclusions	49
3 A semi-atomistic model for electrostatics in confined water	52
3.1 Problematic treatment of confined water	52
3.2 Explicit solvent with clays	54
3.3 Semi-atomistic approach for Calcium-Silicate-Hydrates	55
3.4 Simulations	64
3.5 Water properties in confinement	65
3.6 Summary	67
4 The nanoscale origin of cement cohesion	69
4.1 Simulation methods and parameters	70
4.2 Deviation from primitive model	72
4.3 Increasing surface charge	73
4.4 Dynamic correlations	77
4.5 Hydrated ions vs n -mers	82
4.6 The microscopic mechanism behind cohesion	84
4.7 The role of cement chemistry	88
4.8 Conclusions	93
5 From cohesion and texture to rheology	94

5.1	Experimental characterization of microstructure and rheology	94
5.2	Integrating numerical simulations	96
5.3	Investigating time evolution	101
5.4	Summary and implications	103
	Conclusions and outlook	105
	Appendix: Discontinuous shear thickening in force space	108
A.1	Introduction	109
A.2	Simulation methods	112
A.3	Correlations in force space	120
A.4	Clustering in real space and force space	123
A.5	Constructing effective potentials	128
A.6	Conclusions	135
	Bibliography	138

LIST OF FIGURES

1.1	Scattering data on cement paste and molecular model of C-S-H	8
1.2	Calorimetry and rheology of hydrating cement paste	9
1.3	AFM measurements of forces between C-S-H particles in solutions with differing chemistry	11
1.4	Electrostatic double layer and DLVO theory	13
1.5	The primitive model	16
1.6	AFM measurements and primitive model simulations	18
1.7	Atomistic simulations of C-S-H interactions	18
1.8	Interactions with competing attractive and repulsive forces	20
1.9	C-S-H precipitation in mesoscale simulations	22
1.10	Local packing in mesoscale simulations and spatial gradients in cement paste	23
1.11	Comparison of mesoscale simulations and experiments	25
2.1	Interaction potential and chemical potential in simulations	28
2.2	Volume fraction ϕ vs simulation time	32
2.3	Simulation snapshots	33
2.4	Percolation of C-S-H network	35
2.5	Internal stress distributions	36
2.6	Stress snapshots	37
2.7	Local packing of C-S-H	39
2.8	Network graph analysis	40
2.9	Pore size distribution (PSD) in C-S-H gel	41

2.10	Diffusion in C-S-H pores	43
2.11	Chord length distribution in pores	44
2.12	Specific surface area of C-S-H gel	45
2.13	Scattering cross-section	47
2.14	Scattering intensity	48
3.1	Explicit solvent model in clays	55
3.2	Water density in confinement	66
3.3	The effective dielectric constant of the confined water	67
4.1	Semi-atomistic approach deviates from PM even at low σ	74
4.2	Ion density profiles and hydration shells	75
4.3	Rising correlations and cohesion with increasing σ	76
4.4	Ion and water dynamics at low σ	78
4.5	Ion-water bond correlation	80
4.6	Ion and water dynamics at high σ	81
4.7	Formation of n -mers	85
4.8	A new analytic theory for strongly coupled electrostatics	87
4.9	C-S-H cohesion strength with different ions	90
4.10	Ion dynamics	91
4.11	Aluminum hydration shells	92
5.1	Scattering and rheology measurements of hydrating cement paste	95
5.2	Scattering and snapshots from simulations	98
5.3	Implementing shear in simulations	100
5.4	The elastic and loss modulus of the C-S-H gels	102
A.1	Flow curves	115
A.2	Phase diagram in the shear stress–packing fraction (σ_{xy}, ϕ) plane	118
A.3	Strain rate distributions	119

A.4	Force tile construction	123
A.5	DBSCAN algorithm	126
A.6	Real space DBSCAN analysis	126
A.7	Force space DBSCAN analysis	127
A.8	Coarse-graining force vertex distributions	128
A.9	Effective interaction potentials	130
A.10	State diagrams of the calculated potentials	133
A.11	Fourier analysis	134

INTRODUCTION

Nowadays cement and concrete are ubiquitous materials that make up large portions of our infrastructure and buildings. Nearly everyone is familiar with these materials and encounters them on a daily basis—perhaps even using them in personal projects. Yet most people would be surprised to learn that the fundamental mechanisms underlying cement setting continue to elude us. This is due to the incredible complexity of the material across many length scales, and it is this complexity that I have delved into over the past years. This dissertation is the culmination of that work.

A cement-water mixture starts as a relatively fluid paste that can easily be poured into molds, but it then sets into a strong solid capable of holding up skyscrapers. It is easy to use and cheaply manufactured, a combination that creates high demand. However, this all has an environmental cost as 8% of anthropogenic CO₂ emissions are associated with cement production. Also, despite the strength of concrete, it is not as durable as we would like—leading to deterioration in infrastructure and growing maintenance costs. Most current attempts to design improved cementitious materials are based on trial and error methods, as there is no framework to predict how modifications to cement composition will affect the final properties. The underlying problem is an incomplete understanding of the material because its behavior arises from an interplay of electrostatics, the non-equilibrium solidification, and multiscale heterogeneity.

Cement, the binding agent of concrete, reacts with water to produce a Calcium-Silicate-Hydrate (C-S-H) gel that is heterogeneous and porous at the nm to μm scale. The gel becomes stronger as it gets denser during hydration, and it glues together sand, gravel, and

rocks to form the hardened concrete. The C-S-H gel is the ingredient that binds everything together, and the microstructure of that gel ultimately controls the macroscopic mechanical properties. However, the gel itself is made up of C-S-H nanoparticles. These charged building blocks aggregate in the cement solution, interacting via electrostatic forces mediated by the water and counter-ions in solution. These strongly coupled electrostatics at the nanoscale are not fully understood, and the mechanisms by which cohesion emerge during setting need to be investigated.

In this thesis, I have worked to develop new scientific understanding of this complex and technologically relevant material. Starting at the nanoscale, I have developed a model of explicit ions, interacting with water and confined by charged surfaces. I have used this model to unravel how the strong spatial and dynamic correlations that arise between ions and water, due to the capability of water to restructure around ions, determine the nanoscale forces at play in the emergence of material cohesion. The framework developed here can even be applied to predict the effects of changing cement chemistry on cohesion, or to investigate systems such as clays or DNA which also rely on strongly coupled electrostatics at the nanoscale level.

I have also developed a coarse-grained mesoscale model which is able to elucidate the effect of heterogeneous growth of C-S-H at cement grain surfaces and the time-evolution of the effective interactions. The presence of the surfaces drives the formation of spatial gradients and anisotropies in the material, and these effects are limited or enhanced by the evolving forces between C-S-H nanoparticles. In these investigations, I have developed new analysis tools and explored a number of computational techniques from atomistic to coarse-grained and non-equilibrium molecular dynamics to various forms of Monte Carlo.

Thanks to these developments, we can now extract rheological data from simulations and integrate nano- and meso-scale models with experimental measurements. Rheological tests can be run on the simulated microstructures created from mesoscale models, which in

turn can incorporate different interaction potentials computed from different cement mixtures. Together, this could form a truly multiscale framework to quantitatively predict the material properties of different cement mixtures and how they develop over time from first principles.

This dissertation is organized as follows. In Chapter 1, I introduce cement, its current state of study, and the open scientific questions. In Chapter 2, I describe the growth and microstructure of the C-S-H gel that forms during cement hydration, and clarify the role of spatial heterogeneities and the interactions between C-S-H particles. In Chapter 3, I delve into the electrostatics which control the C-S-H interactions. By discussing what existing theories and models miss, I motivate and explain the development of a semi-atomistic model. In Chapter 4, I describe how I use this model to investigate the origin of cohesion in cement. Analyzing spatial and dynamical correlations, I unravel the nanoscale mechanism responsible for the emergence of net attractive forces over time during cement hydration. Finally, in Chapter 5, I discuss ongoing work to investigate the rheological properties of my simulated microstructures in connection with experimental measurements. I conclude by discussing the connection between the nanoscale cohesion, mesoscale morphology, and macroscopic rheology.

CHAPTER 1

CEMENT AND PHYSICS

Cement reacts with water to produce a gel network that rapidly grows denser and harder, creating a solid with an elastic modulus on the order of 10 GPa—the exact value depends on the specific recipe and conditions during setting. The microstructure of the final hardened material is highly dependent on the way it is formed, starting from the much softer gel at the early stages of hydration. This non-equilibrium process, of cement hydrates growing from the reaction interface between cement grains and water to form a percolating solid network, is a fascinating soft matter physics problem. At a smaller scale, that gel network is made of nano-sized building blocks whose surfaces are highly charged and immersed in a solution of water and ions from the dissolving grains. The net interaction forces between these nanoparticles are governed by electrostatics and statistical physics. Despite cement being a commonplace material, its properties are determined by uncommon and challenging physics problems at multiple length scales. I will delve into my work on the mesoscale (Ch. 2) and nanoscale (Ch. 3 and 4) problems in the coming chapters, but first I will introduce cement as a material and explain the advances and open questions in its study.

1.1 WHAT IS CEMENT?

The term cement is often colloquially used interchangeably with concrete: which is a rock-like construction material used for all manner of buildings, bridges, etc. However, concrete

is an amalgamation of cement, water with which it reacts, and aggregates such as sand, gravel, or rocks. The reaction between water and cement is responsible for the setting (during which the solidification is not caused by drying), and the produced hydrates are responsible for gluing together the various components that went into the mixture. This process, while complex and still not completely understood at the physical-chemistry level, is very effective in delivering an incredibly strong and cheap material, which is the foundation of our built infrastructure and the most used synthetic material on Earth.

Hydraulic binders of this type have a very long history. In fact, a type of cement is known to have been used by the ancient Romans, over 2000 years ago, in structures such as aqueducts and the Pantheon—which still stand today. The recipe was based on volcanic rocks in the south of Italy, and its use did not become widespread. The modern formulation, called Portland cement after the similarity of the hardened product to Portland stone from the Isle of Portland, was pioneered in the mid 1800's, and its use quickly spread around the world. Today, the most common version is still Ordinary Portland Cement (OPC), though often mixed with various additives.

OPC is made mostly of Calcium-Silicates. The exact formulation may vary between sources, but tri- and di-Calcium Silicate (C3S and C2S in cement literature) make up over 80% of cement by mass [138]. Calcium-Silicates are made from natural, cheap, and globally abundant ingredients such as limestone (CaCO_3) and clay (a source of Silicate). These are ground into powder and heated in kilns at high temperatures. This process releases the Carbon as CO_2 and sinters the Calcium and Silicon to form the Calcium-Silicates in rock-like objects called the clinker [138]. The clinker is ground up and mixed with small quantities of additives to produce OPC. The cheap ingredients, combined with the early workability of the concrete mixture (which is a relatively fluid paste before setting) and the high strength reached upon setting make it an ideal construction material.

The development of cement has facilitated rapid construction of new structures which became necessary with increasing urbanization since the industrial revolution. Currently, cement production is only expected to increase as demand for new buildings continues to grow—mainly in developing countries, with China and India leading the pack [62]. This all comes with an environmental cost, as about 8% of global CO₂ emissions arise from cement production [7]. Most of this is associated with the decarbonation of limestone when creating the clinker.

The greenhouse gas emissions could be reduced by improving cement strength so less is needed or by using alternative compounds, which do not produce as much CO₂, to make the cement. Having a better control of cements properties during setting is hard and mainly achieved through additives which can modify the properties and durability of the final material. However, it is crucial for a wide array of construction applications: from controlling setting time for 3D printing concrete to modifying the final mechanical properties for stronger, longer-lasting structures. New technologies, advanced material design, and more sustainable processes are all hindered by the incomplete understanding of the fundamental mechanisms that govern the setting of cement: from the nanoscale electrostatic cohesion, to the mesoscale gel network formed out of equilibrium, to the microscopic underpinnings of the macroscopic material properties.

1.2 CALCIUM-SILICATE-HYDRATES

The chemistry of cement hydration is complex, with multiple processes (dissolution, diffusion, adsorption, nucleation, precipitation) happening simultaneously [22, 110, 138]. The kinetics of these different processes and the formation of multiple hydration products make it difficult to isolate and characterize any individual part of the hydration. To limit this complexity, most studies focus on the hydration of alite (an impure tricalcium silicate, Ca₃SiO₅,

or C_3S in cement chemistry notation) which is the main constituent of the cement powder and is responsible for the formation of the Calcium-Silicate-Hydrate (C-S-H) gel. C-S-H, in turn, is the main product of cement hydration, and the gel it forms has been recognized as the principal contributor to the macroscopic strength of the material [109]. The various components of cement are thoroughly discussed in the literature [22, 138], but in this thesis I mainly focus on C-S-H.

As the progressive dissolution of cement raises the concentrations of Calcium and Silicon in solution, the saturation of these species leads to the precipitation of C-S-H. The precipitated C-S-H is amorphous and its exact form debated: the two main ideas are that it is formed of large but defective sheets/ribbons of silicate layers [47] or that it is an assembly of lamellar nanoparticles [4, 27, 97, 106]. Both concepts draw comparison to the minerals Tobermorite and Jennite, which are crystalline calcium silicate hydrate minerals with different Ca/Si ratios. Neutron scattering experiments [4, 27] provide evidence of a characteristic size of 5nm corresponding to the thickness of platelet-like objects (Fig. 1.1, left).

The measured mean Ca/Si ratio of C-S-H produced by the hydration of OPC is approximately 1.7 [4], though the distribution in the values is wide [115]. This Ca/Si ratio is notably higher than the values for Tobermorite (0.83) and Jennite (1.5), which could explain why the C-S-H does not form a large-scale crystal. As a consequence, a major advance in terms of molecular models for C-S-H was achieved by starting from these crystalline phases and introducing defects which increase the Ca/Si ratio. This approach, pioneered by Pellenq et al [106], has provided the first realistic molecular model of C-S-H in the hardened paste (Fig. 1.1, right) that produces, as a result not input, features such as the density of C-S-H particles as measured by scattering experiments [4]. In this model, Calcium-Silicate chains form layers with water and Calcium ions confined between them, with a high surface charge due to the ionized Silanol groups in the Silicate chains [106]. At earlier times, the C-S-H

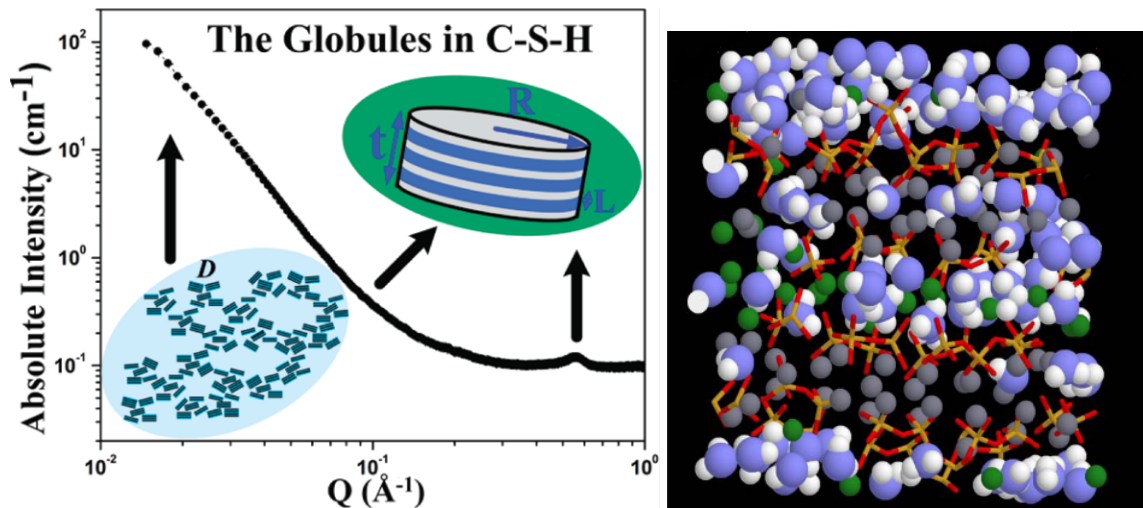


Figure 1.1: Scattering data on cement paste and molecular model of C-S-H. Left: Small angle neutron scattering of cement paste shows a bump at high q corresponding to the typical size of C-S-H nanoparticles [27]. Right: A molecular model for C-S-H where the blue-white particles are water, the gray and green spheres are intra- and inter-layer Calcium ions, and the yellow and red sticks are Silicon and Oxygen atoms in Silica tetrahedra [106].

structure may be different as the solution chemistry changes during the course of hydration, and the surface charge is known to change with pH [77].

The nanoparticles aggregate into a gel network, and the larger-scale microstructure of the C-S-H gel is coupled to the non-equilibrium reaction kinetics that govern C-S-H precipitation. As the hydration is an exothermic process, measuring the total heat flowing in or out of the system gives us insight into how the reaction proceeds. Calorimetry curves show that, after an initial burst, the system appears dormant for a period of time (Fig. 1.2, left). This is followed by an acceleration in the reaction rate up to a peak typically reached at approximately 9 hours. After this peak, the reaction slows down but continues indefinitely [22].

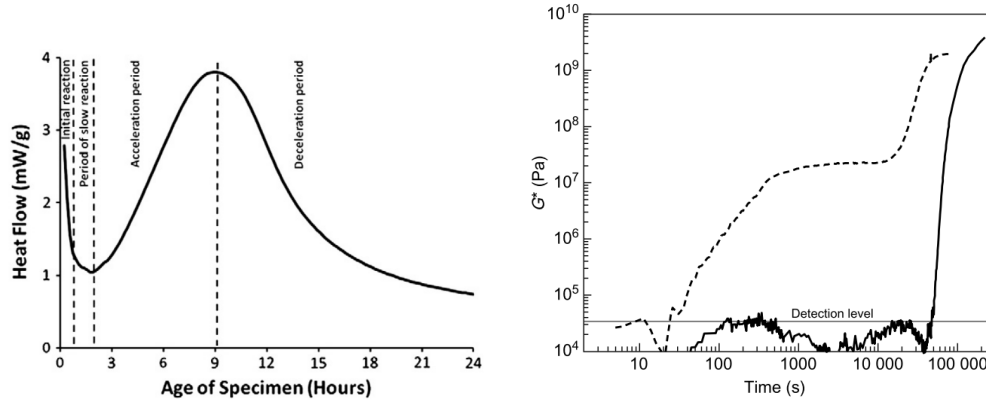


Figure 1.2: Calorimetry and rheology of hydrating cement paste. Left: Calorimetry curves measuring the heat released by the exothermic hydration of cement [22]. The heat flow serves as an indicator of the rate at which the reaction is progressing, and this turns out to be non-monotonic. After an initial reaction, the system is nearly dormant for a period, before the main setting occurs during an acceleration and deceleration period. Right: Shear modulus of cement with (solid) and without (dashed) plasticizers [80]. The non-uniform reaction leads to a non-linear development of mechanical strength, and the macroscopic properties are strongly sensitive to changes in the chemistry.

The macroscopic properties that emerge from this process develop non-linearly during the setting (Fig. 1.2, right). Rheology of the cement shows an early solid response that stays constant for a period before jumping up to the final value. The measured modulus is also highly dependent on the chemistry as the addition of plasticizers was seen to suppress the early plateau entirely [80]. When it sets, the hardened paste is very dense, but still porous and heterogeneous at small scales. Measurements with NMR, neutron/x-ray scattering, and gas sorption have demonstrated the complex pore structure of the cement paste [145], which affects the mechanical strength and durability of the material. The final texture is clearly still out of equilibrium and continues to age/creep [148].

While it is clear that the micro- and macro-scale properties arise from the non-equilibrium aggregation and gelation of the C-S-H building blocks, the connection between

the molecular level description of C-S-H and its microstructure is not fully understood. Mesoscale simulations [63, 64, 65] based on coarse-grained colloid-like C-S-H particles, modeled via molecular dynamics with an effective interaction potential and a Grand Canonical Monte Carlo process to mimic precipitation, have made significant strides here. As I will discuss further in Sec. 1.4, these models incorporate the nanoscale forces between C-S-H particles through an effective interaction potential.

C-S-H particles are highly charged and in solution with ions, hence electrostatic forces govern their net interactions. This is demonstrated in experiments by Plassard et al [107], who measured the force between an AFM tip coated with C-S-H and a C-S-H substrate in a Calcium-Hydroxide solution (Fig. 1.3). The measured forces extended several nanometers beyond contact and were strongly affected by the concentration and pH of the solution. At low concentrations, when the surface charge density of the C-S-H and the number of Calcium counter-ions are both low, the net force was repulsive. However, upon increasing concentration, an attraction between the C-S-H surfaces was observed. This trend runs counter to the expectations of classical mean field theories for surfaces forces in solution, like the theory by Derjaguin, Landau, Verwey, and Overbeek (DLVO) [66], which predicts that an increased surface charge would lead to increased repulsion. Due to the presence of multivalent counter-ions in strong confinement between highly charged surfaces, in fact, the electrostatics in cement solutions is not accurately described by DLVO, and a more in-depth study is required.

1.3 ELECTROSTATICS IN SOLUTION

Interactions between charged surfaces in an electrolyte solution are at play in many biologically and technologically important materials. Mean-field analytic theories, such as DLVO, can quite accurately describe the cases of “weak coupling” (low surface charges,

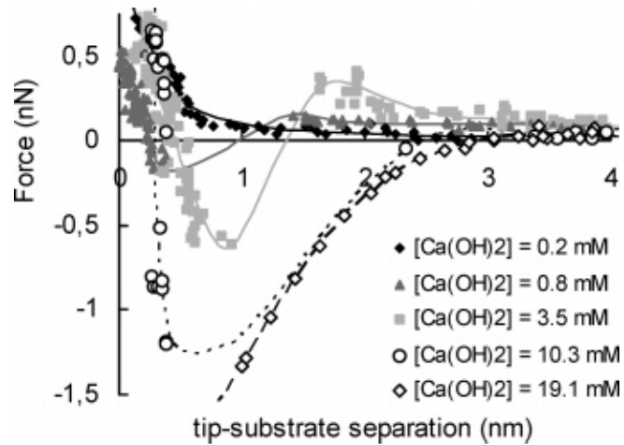


Figure 1.3: AFM measurements of forces between C-S-H particles in solutions with differing chemistry. The increasing concentration is one change that occurs with increasing cement hydration time [107]. These measurements demonstrate a complex evolution of the interactions over time during setting.

monovalent ions, large separations). Outside of this regime, the discrete ion size, interactions between ions, the solvent properties, and even the molecular nature of the surface can dramatically alter the overall surface-surface interaction. C-S-H falls into this second category. The physics underlying the strong coupling regime have been studied extensively, and in this section I will describe the progression of previous studies and the currently open questions.

1.3.1 MEAN FIELD THEORIES

Over 100 years ago, Gouy and Chapman independently proposed a theory that brings together the exact Poisson equation for electrostatics with the assumption that ion concentration in a solution depends on the Boltzmann factor related to the electrostatic potential

[66]. This gives a second order differential equation that can be solved to calculate the electrostatic potential φ .

$$\nabla^2 \varphi = -\frac{\rho}{\varepsilon} \quad (1.1)$$

$$\rho = \rho_0 \exp[-q\varphi/k_B T] \quad (1.2)$$

Here ρ is the charge density, ε the dielectric permittivity (vacuum times relative), q the charge of ions, and T the temperature. The theory treats the ions in solution as an ideal gas. The ion size is not considered, and there are no direct interactions between ions—they only interact with the mean field defined by φ . This approximation works well if the ion concentration is dilute and ion valency low, such that ion-ion correlations are not significant. This gives rise to the electric double-layer [66], which consists of a Stern layer, set by ion size, and a diffuse layer where the ion concentration is lower (Fig. 1.4, left).

An analytic solution of the Poisson-Boltzmann equation requires an approximation to be made. Debye and Hückel truncated the Taylor series for the exponential to first order so $\exp[-q\varphi/k_B T] \approx 1 - q\varphi/k_B T$ [66], valid for $q\varphi \ll k_B T$. Given a net neutral system, this approximation reduces the PB equation to:

$$\nabla^2 \varphi = -\kappa^2 \varphi \quad (1.3)$$

where the Debye length is $\kappa^{-1} = \sqrt{\varepsilon k_B T / 2\rho q}$, which gives the electrostatic screening distance. In this framework, the electrostatic interactions between two like-charged surfaces are purely repulsive. Due to the presence of screening ions, this force falls exponentially with distance.

Derjaguin, Landau, Verwey, and Overbeek extended this treatment to include attractive Van der Waals forces [37, 149]. In DLVO theory, dispersion interactions between atoms in a surface (with the form r^{-6}) are integrated to give a net attraction between surfaces of

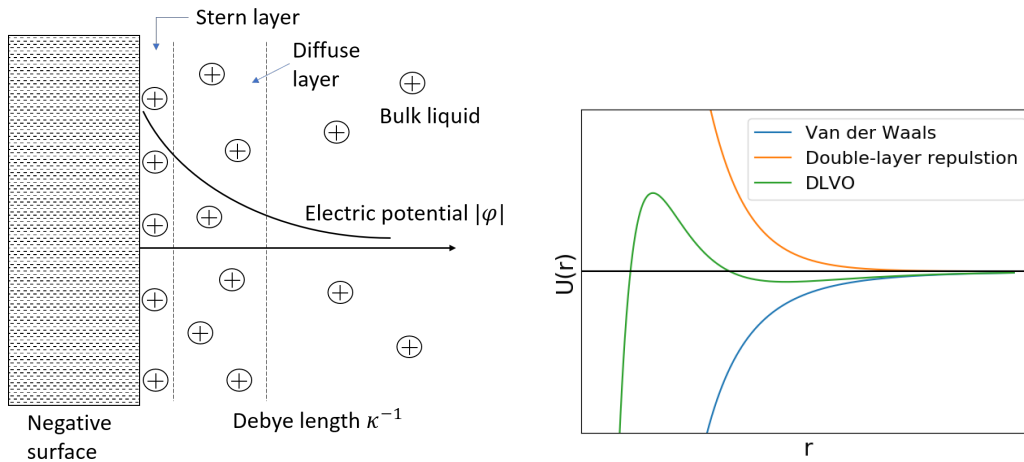


Figure 1.4: Electrostatic double layer and DLVO theory. Left: Schematic representation of the Poisson-Boltzmann based double-layer that forms near charged surfaces in electrolyte solutions. The accumulation of counter-ions near the surface screen the electrostatic potential over a distance given by the Debye length κ^{-1} . Right: Example potential energy between two like-charged particles via DLVO. Included as a demonstration of the typical DLVO behavior. Axes are dimensionless. The competition between an electrostatic repulsion and a Van der Waals attraction can give a repulsive barrier and non-contact attraction.

$F_{VdW} \propto -z^{-2}$, where z is the distance between the surfaces and the proportionality constant depends on the atomic polarizabilities and densities in the two surfaces. Combining the dispersion term with the electrostatics gives competing attractive and repulsive forces (Fig. 1.4, right).

The weak coupling mean field approach has been very successful. It has significantly advanced our understanding of electrostatics in a wide range of materials, especially relevant to soft matter and biophysics. However, the approximations made are expected to hold in systems with low surface charges, ion concentrations/valency, and confinement. Beyond this limit, ion-ion correlations may become significant and the ideal gas picture may break

down. However, a different mean field approximation can also be applied at the other end of the spectrum, for strong coupling.

In the strong coupling regime, ions can self-assemble into a lattice. This idea is traced back to Wigner, who predicted the crystallization of electrons under certain conditions in 1934 [151]. While an electron cloud is by no means the same as an ion solution, parallels can be drawn. In the case of electrons, quantum fluctuations can be suppressed if their density is low and the potential energy gain for localizing into a lattice is less than the entropic cost. In the case of ions, a similar effect can happen in the strong coupling regime because of the high electrostatic potential energy relative to thermal fluctuations, and it has been used to explain the attraction between DNA molecules [116]. More generally, the ground state crystal configurations of confined ions can be calculated [119], and the interactions of ions with a mean field produced by this ion crystal can be used to obtain an expression for the pressure induced between the surfaces within which these ions are confined [120].

The mean field theories help to frame the problem of electrostatics in solution. In either the weak or strong coupling limit, reasonable analytic predictions can be made, but how does one go from one limit to the other? For cement, experiments (Fig. 1.3) have shown that the forces can change from repulsive to attractive with the solution chemistry—perhaps passing from weak to strong coupling limits. It is not clear which specific conditions are adequately described by which limit, and the “intermediate” scenario does not seem to be captured by the mean field approach at.

1.3.2 PRIMITIVE MODEL

A major advance from mean field approaches was made with the primitive model (PM) [72]. The PM is, in principle, very similar to the mean field theories. One considers infinite, planar, uniformly surfaces which confine ions in a dielectric continuum. The key distinction

is that now each ion is treated individually, with finite size, not as part of a continuous density function. Consider the Hamiltonian for such a system:

$$H = -\frac{\sigma^2 AD}{2\epsilon} + \sum_i \left[U_{\text{short-range}}^{\text{surface}}(z_i) + \frac{1}{2}mv_i^2 \right] + \sum_{i,j} \left[\frac{q_i q_j}{4\pi\epsilon r_{ij}} + U_{\text{short-range}}^{\text{ion}}(r_{ij}) \right] \quad (1.4)$$

In the above equation, D represents the distance between the charged surfaces, σ the surface charge density, and A the surface area. The various terms correspond to surface-surface energy, ion-surface energies, and ion-ion energies. The short-range interactions are unspecified but could range from hard-spheres to a Lennard-Jones potential. This can be, in principle, the same underlying Hamiltonian as for the mean field theories, but in those approaches approximations was made so that the ion degrees of freedom could be integrated out analytically. With the primitive model, instead, one can use numerical simulations so that each ion degree of freedom can be tracked, equilibrium states sampled, and the net pressure calculated as the average of a microscopically fluctuating quantity.

The advantage of adding all this complexity is that one should obtain, in principle, the full spectrum of behaviors (low to high coupling). If temperature based entropic effects dominate, the weak-coupling mean field behavior should be recovered, with fluctuating ions behaving like an ideal gas. If the electrostatics based energetic effects dominate, one expects the ion crystallization of the strong-coupling limit. Most importantly, this approach should provide information on what happens in between, when both energetic and entropic effects are important.

Early work with the PM used Monte Carlo simulations and a hard-sphere short-range potential. Pellenq et al studied the effect of surface charge density σ , surface separation D , and ion type on the pressure between two parallel surfaces confining counter-ions [101]. They found that, for a large range of σ and many ion types, it was possible to develop one or more attractive wells in the electrostatic pressure between the surfaces. While like-charge

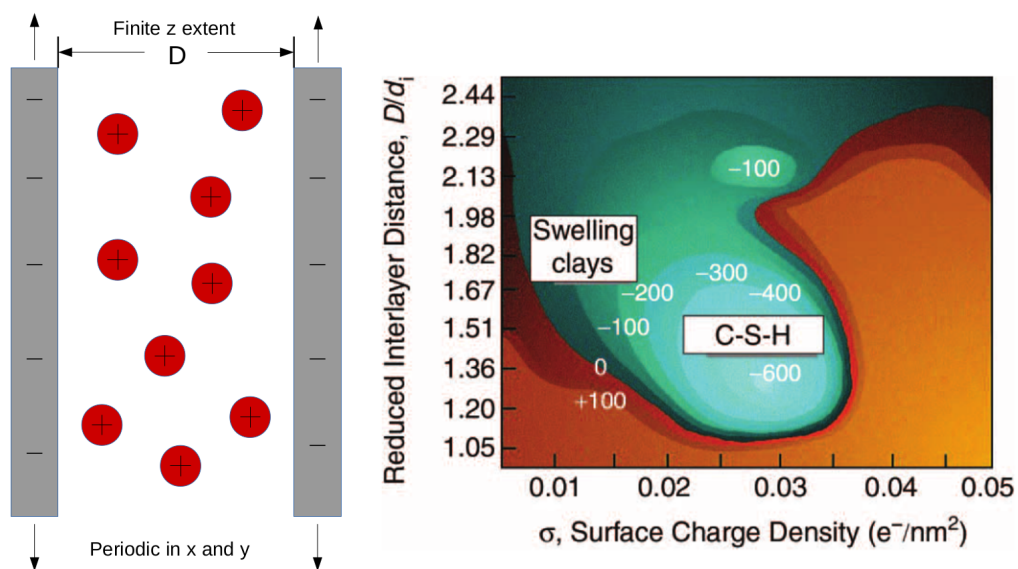


Figure 1.5: The primitive model. Left: A schematic of the PM system. Infinite, uniformly-charged walls confine ions to a slab, finite in the z direction. The ions are treated individually, introducing many degrees of freedom, but accounting for their finite size and ion-ion correlations. Right: A plot of the pressure (contours, in atmospheres) as a function of surface charge and surface separation [102]. This is for Calcium (divalent) counterions. Also labeled are regions that correspond to the physical systems of swelling clays and C-S-H.

attraction had been predicted by strong-coupling theories and observed experimentally, this work demonstrated systematically the large variety of phase behaviors that could arise in real materials. Specifically focusing on Calcium ions, which are abundant in cement, they found multiple areas of attractive pressure in the surface charge density/surface separation plane (Fig. 1.5), including for the surface charge corresponding to C-S-H in the hardened cement paste ($\sigma \cong 3e/\text{nm}^2$).

Later work by Jonsson et al focused more specifically on the interactions between C-S-H particles [73, 74], in particular in connection with the AFM measurements of the surface forces in C-S-H by Plassard et al [107]. This study included salts—i.e. both co-ions and counter-ions. In the counter-ion only case, the number of ions is exactly set by the electroneutrality condition. With salts, there is an additional parameter as the ion numbers are not entirely specified by the surface charge density. Jonsson et al used a grand canonical ensemble to determine ion concentrations, which requires as an input the total chemical potential μ of the salts—determined via the Widom insertion technique [150]. They went on to compute an estimate of the force between a C-S-H coated AFM tip and a C-S-H substrate, which showed good qualitative agreement with experimental results (Fig. 1.6).

1.3.3 A MISSING LINK

While the PM provides a way to numerically probe all kinds of situations beyond mean field, and related studies demonstrated the possibility of attraction at finite coupling, in the case of C-S-H the cohesive strength predicted by PM simulations is on the order of $\approx 60\text{MPa}$ for the hardened paste [102]. This value is too small compared to the elastic modulus of hardened C-S-H, which is measured to be greater than 10GPa in nanoindentation experiments [93, 148]. Macroscopically, 60MPa is more consistent with the modulus of rubber than of concrete—what is missing?

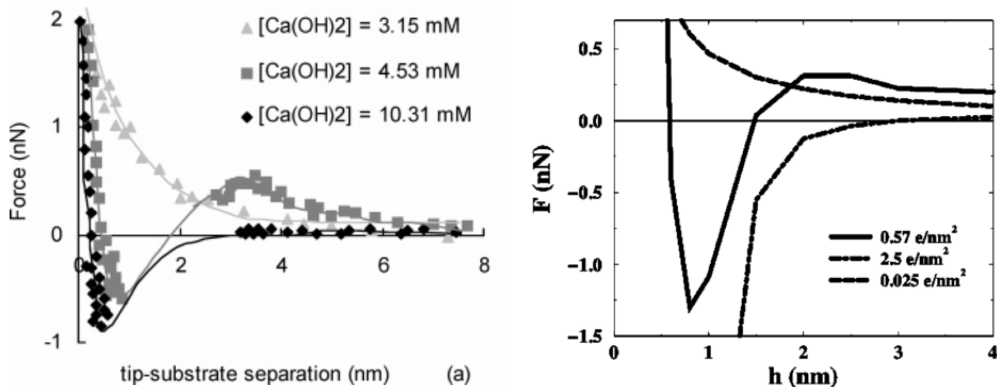


Figure 1.6: AFM measurements and primitive model simulations. Left: AFM measurements of force as a function of pH (which controls surface charge) [107]. Increasing surface charge increases attraction, which is at odds with the behavior predicted by DLVO. Right: Estimates of these forces using the primitive model [73]. Increasing correlations between ions can be a mechanism for electrostatic attraction.

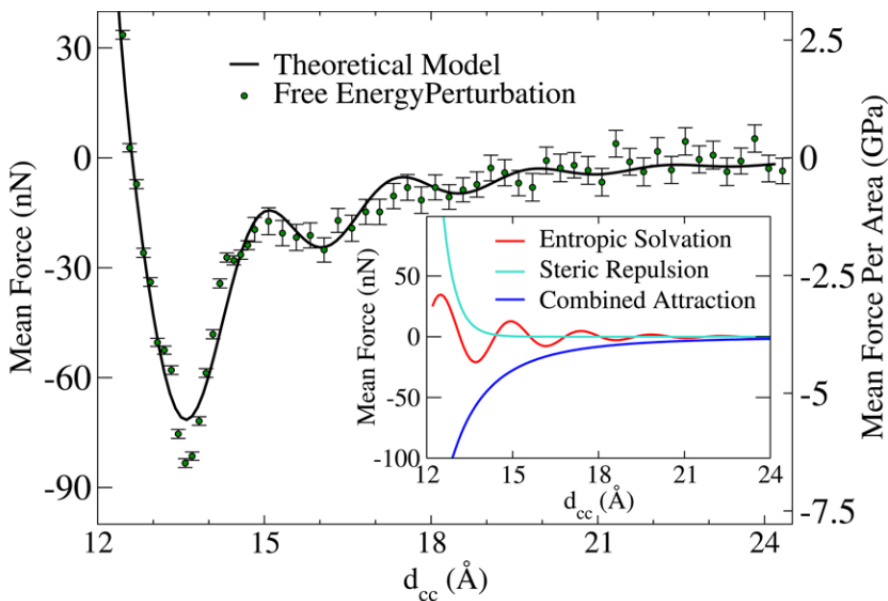


Figure 1.7: Atomistic simulations of C-S-H interactions. The force between two crystalline C-S-H layers, computed from atomistic simulations [89]. The minimum pressure of ≈ 6 GPa is almost two orders of magnitude stronger than what is predicted by PM simulations [102].

More detailed atomistic simulations show a drastically stronger cohesion between two layers of Tobermorite, considered as a first approximation for hardened C-S-H (Fig. 1.7). Treating the surfaces and solvent (water) in full atomic details, the mean pressure between the surfaces at small separations is found to approach ≈ 6 GPa, which is about 100 times stronger than what was predicted with the PM. In Ch. 3 I will discuss the source of this discrepancy and develop a new, semi-atomistic model that captures the most important ingredients. Using this model, in Ch. 4 I will describe the microscopic mechanisms behind cohesion of C-S-H and how it develops during hydration.

1.3.4 EFFECTIVE INTERACTIONS THAT EVOLVE WITH TIME

AFM experiments [107] indicate that the higher ion concentrations in the late stages of hydration produce effective interactions with an increasingly deeper attractive well. On the other hand, the interactions at early stages seem to have an additional repulsion at intermediate separations. Interaction potentials with competing attraction and repulsion have been studied in a variety of contexts [28, 156] and been shown to have complex phase diagrams containing a variety of microphases (Fig. 1.8). I myself have also studied the phase behavior of a similar potential in a rather exotic scenario: as a tool to describe the correlations of points in force space for shear thickening suspensions (see Appendix). During cement hydration, the precipitation of C-S-H and the evolution of their interactions may create a specific pathway through these phase diagrams.

In the context of gels, the final interactions and densities are rarely sufficient to describe the morphology—the history of the material plays a significant role [15]. Thus to model the mesoscale morphology of C-S-H, the explicit time evolution of the nanoscale interactions needs to be considered in conjunction with the C-S-H precipitation and in the context of their aggregation and gelation. This has been done through the development of a non-equilibrium mesoscale model.

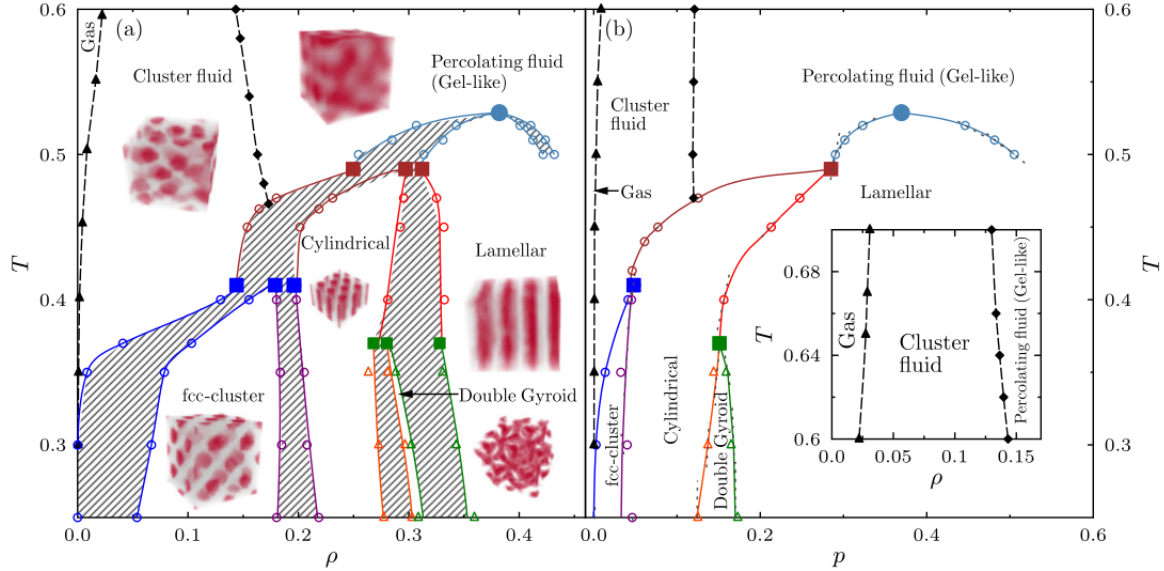


Figure 1.8: Interactions with competing attractive and repulsive forces. An example phase diagram for a system with competing interactions, where ρ is the density, p is the pressure, and T , the effective temperature, is the inverse interaction energy [156]. The precipitation of C-S-H and the evolution of their interactions drives the system through different regions of this diagram, affecting the morphology of the final material.

1.4 A NON-EQUILIBRIUM MESOSCALE MODEL

To study the microstructure of cement in the context of C-S-H precipitation and evolving effective interactions, Ioannidou et al developed a computational model combining molecular dynamics of C-S-H particles with pairwise interactions and a Grand Canonical Monte Carlo scheme of adding/deleting particles [63]. In the GCMC framework, the system is linked to a fictitious reservoir of particles that have a chemical potential μ . By imposing a large μ , particle creation is energetically favorable in the simulations without explicitly accounting for the chemical conditions that make it so in the real system. The GCMC process allows them to mimic the C-S-H precipitation in a coarse-grained approach that can effectively model the mesoscale C-S-H gelation.

Through this model, it is possible to explore the dynamics and morphology related to a specific interaction potential in non-equilibrium conditions. Starting with only a few particles, the GCMC exchanges tend to add particles. Although the final equilibrium state corresponding to the chosen μ is unknown, this state is never reached in practice. As the system becomes very dense, particle addition becomes a slow process, and the system gets trapped out of equilibrium. In reality, this is comparable to what happens in real cement where C-S-H keeps precipitating and there are signs of continued, albeit excruciatingly slow, reaction years after it has hardened.

1.4.1 THE ROLE OF THE INTERACTIONS

Ioannidou et al examined in detail the features associated with a potential that has an attractive well and repulsive shoulder in non-equilibrium conditions, inspired by the experiments of Plassard [107]. By varying the height of the shoulder, they considered potentials that reproduced the potentials seen at early and late stages of cement hydration. While the GCMC scheme is obviously a large simplification of the precipitation process, it allowed them to deal with a simpler system which only included the C-S-H particles instead of all the different atomistic species. This approach was found to produce accelerating/decelerating regimes, akin to the calorimetry measurements in experiments, due to formation of a space-filling gel (Fig. 1.9) [63].

In these non-equilibrium simulations, the gel morphology was found to be strongly dependent on the interaction. Their results indicated that the Early Stage (ES) interactions favored rapid growth/gelation and early mechanical properties, while the Late Stage (LS) interactions favored densification [64]. The early gelation promotes a more uniform densification because the pore size distribution in the gel tends to be more uniform and thus plays an additional important role in the final mechanical strength of the material. The differences in local structure were quantified using the bond orientational order (BOO). Introduced by

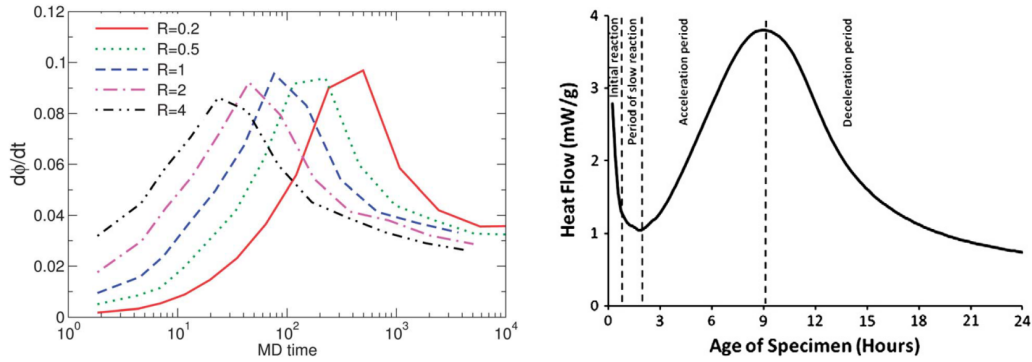


Figure 1.9: C-S-H precipitation in mesoscale simulations. Left: Evolution of volume fraction ϕ with MD time for different MC rates (MC steps/MD steps) obtained in the simulations of [63]. Acceleration and deceleration regimes arise naturally due to the formation of a space-filling gel. Right: Calorimetry curves measure the heat flow which is proportional to the rate of the exothermic reaction [22].

Steinhardt in 1983, this method of examining the orientation of bonds between particles allows one to precisely determine the local ordering and packing in amorphous systems [133]. The rotational invariants, computed from the projections of the bond angles onto the spherical harmonics, allow one to differentiate between the locally crystalline ordering of the late stage potential and the Bernal spiral-based ordering of the early stage (Fig. 1.10, left). The latter corresponds to face-sharing tetrahedra that are prevalent in the fibrillar gel typical of ES interactions.

The large differences that arise from changing the interaction potential in these simulations, considering the changing interactions in the real system, suggest that said change plays an important role in cement hydration. In this scenario, the formation of elongated, Bernal Spiral structures in the early stages leads to early percolation of a load-bearing structure across the sample and the reduced repulsion at late stages promotes strengthening the existing framework, forming locally dense, compact, and stiffer structures.

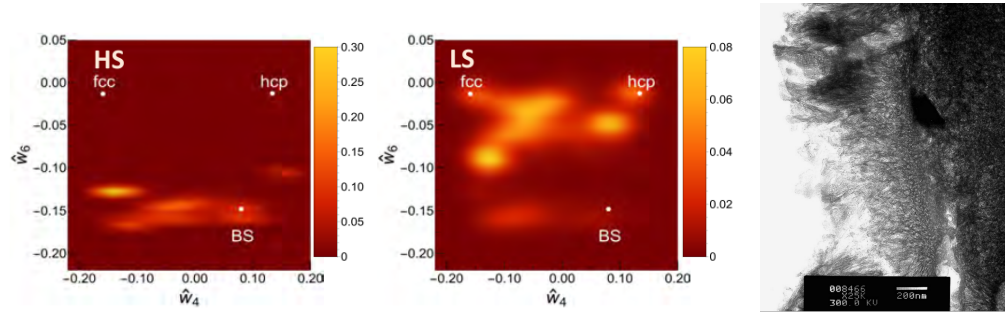


Figure 1.10: Local packing in mesoscale simulations and spatial gradients in cement paste. Heat maps of the rotational invariants (\hat{w}_4, \hat{w}_6) for the early stage (left) and late stage (center) potentials from Ref [64]. Values corresponding to fcc, hcp, and Bernal spiral ordering have been labeled. Right: TEM images of the early stage C-S-H gels show clear anisotropy as they grow from cement grain surfaces [35]. There is also a density gradient as the darker regions at the right (near the cement grain surface) are notably denser than the regions to the left.

The specific way in which C-S-H forms has a clear impact on the overall morphology of the final material, and these studies have demonstrated how the heterogeneous C-S-H growth happens in conjunction with the changing interaction potential (due to evolving chemistry). While this approach captures several aspects of the C-S-H growth and gelation, it does not consider that during cement hydration there are typically strong spatial gradients in C-S-H formation—for example, due to the ion concentrations being higher close to the surface of the dissolving cement grains. In the literature, these effects are recognized by distinguishing between “inner product” and “outer product” [32], or in terms of “low density” or “high density” C-S-H [139]. TEM images in the right panel of Fig. 1.10 show an example of the spatial density gradients and structural anisotropy induced by the heterogeneous growth of C-S-H during hydration [35]. I have built on the work of Ioannidou et al [63, 64, 65] to investigate the role of these spatial gradients in the development of the gel morphology, also considering the effect of different interactions as cement hydration

proceeds. The new model, the investigations performed, and the outcomes of my study will be discussed in Ch. 2 and Ch. 5.

1.4.2 MECHANICAL AND STRUCTURAL PROPERTIES

The mesoscale texture of the C-S-H obtained from the simulations of the Ioannidou approach [65] have been analyzed in terms of structural and mechanical properties to compare with experiments. Continuing precipitation to high volume fractions allowed Ioannidou et al to reach conditions comparable to the hardened paste starting from the softer gels [65]. By doing nanoindentation tests, they measured a modulus that was consistent with experimental measurements at high volume fraction (Fig. 1.11), and this model with progressively increasing density also allowed them to measure the mechanical strength of the initially less dense gel where experimental measurements are challenging. Performing a similar comparison with scattering data, they observed a $I(q) \propto q^{-3}$ scaling, consistent with experiments, over the range of $0.1\text{nm}^{-1} < q < 1\text{nm}^{-1}$. At smaller q , the finite simulation volume disrupted this trend, and at larger q they observed a Porod q^{-4} scaling, consistent with the effects of their particle size. This indicates that their simulations exhibit structure across a wide range of length scales, much like that found by experimental scattering data.

These comparisons demonstrate that this mesoscale modeling can be used to probe the mechanical and structural properties of hydrated cement. An advantage of these models that can be explored further is the ability to quantitatively study these properties during earlier stages of hydration, when experiments are more challenging due to the rapid changes in the material. This is crucial for advanced material design that requires precise control of the flowability and strength of the hydrating cement paste. In Ch. 5, I will discuss my ongoing work to develop a quantitative understanding of the rheology of cement pastes in connection with the nanoscale cohesion of C-S-H and their mesoscale morphology.

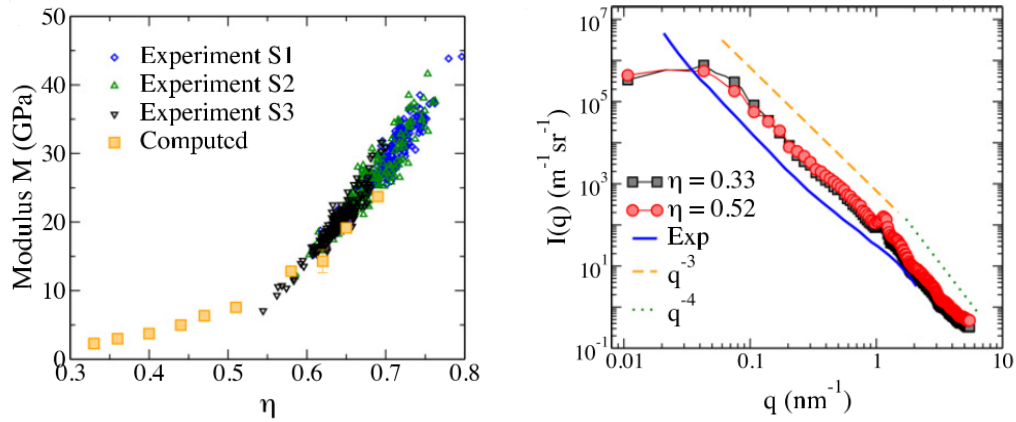


Figure 1.11: Comparison of mesoscale simulations and experiments. Comparison of experimental and computed values of the nano-indentation modulus (left) and scattering intensity (right) [65].

1.5 SUMMARY

Cement is the most used synthetic material in the world, responsible for 8% of global CO_2 emissions [7]. Its hydration leads to the formation of a cement hydrate (C-S-H) gel network, which is responsible for binding concrete and providing its mechanical strength. From the nanoscale electrostatic cohesion, to the mesoscale gel network formed out of equilibrium, to the microscopic underpinnings of the macroscopic material properties, I have provided an overview of the main theoretical and modeling questions to be addressed in order to develop a scientific understanding of this complex material.

In the next chapter, I will discuss my work on a new formulation of the Ioannidou approach [63, 64, 65] that includes spatial gradients. I will investigate the heterogeneous growth of C-S-H in the context of time-evolving effective interactions and show how the evolution of those interactions controls the development of spatial gradients and anisotropy in the C-S-H microstructure.

CHAPTER 2

CALCIUM-SILICATE-HYDRATE GELATION AND MICROSTRUCTURE

The combination of reaction kinetics driving the nucleation and growth of C-S-H particles [46, 141] with changing effective interactions [78, 107] drives the non-equilibrium formation of the C-S-H gel. This pathway has a clear effect on the microstructure, which shows strong spatial gradients and anisotropy, and it is in this context that we need to understand the development of C-S-H morphology during hydration. To do so, one important question to answer is how exactly the way C-S-H forms affects its final properties. Another is how the changing interactions couple to the non-uniform C-S-H precipitation.

We use a mesoscale model to answer these questions, expanding on work which has had success in understanding the role of the changing interactions [64] and their effects on the hardened paste [65]. Specifically, we implement a spatial gradient in the C-S-H precipitation, corresponding to the nucleation of C-S-H at cement grain surfaces. Using a wide range of computational analysis tools, we then characterize the C-S-H network, pore structure, internal stresses, and more. This analysis gives insight into the effect of heterogeneous C-S-H growth mechanisms on the overall microstructure, but it also demonstrates how this effect is enhanced or limited by the features of the interaction potential. In particular, non-contact repulsion, due to electrostatics and present in the early stages of hydration, can limit the density gradients and anisotropy of the C-S-H gel. The results obtained may help explain the surprising robustness of the C-S-H gel against phase separation induced by density gradients and against the formation of a dense C-S-H layer at the cement grain

surface that can block or slow down further reaction. Understanding the role of the interactions during the heterogeneous formation of the C-S-H gel is an important step towards designing new and better cementitious materials.

2.1 THE MODEL

In our model, C-S-H nanoparticles are coarse-grained and treated as spherical particles of fixed size. An effective interaction potential is prescribed to these particles that includes the net interactions mediated by the solvent. The physics behind these interactions is a complex problem in itself. It has been studied extensively via both experiment and simulation [14, 73, 74, 78, 89, 105, 107] and will be the subject of Ch. 3 and Ch. 4. The forces at play emerge from the fluctuations of the electrolyte solution confined between the highly charged C-S-H surfaces. While we do not include the solvent and counterions explicitly in the model here, it is the correlations between these species that give rise to strongly attractive non-contact forces between C-S-H nanoparticles. These correlations are highly dependent on ion concentrations and pH [107], so the overall interactions change over time as the continued dissolution of cement alters the solution chemistry.

For simplicity, we consider fixed forms for the effective interaction during precipitation but investigate two different forms. Following the example of previous studies [63, 64], we implement a potential that has a short-range attractive well coupled with a longer-range repulsive barrier—a shape that is consistent with both the experimental and simulation work done [105, 107]. In Ch. 3 and Ch. 4 I will discuss the emergence of these interactions from the nanoscale physics of C-S-H, as well as how such interactions might be relevant to a wide range of materials.

The quantitative form of the interaction potential is:

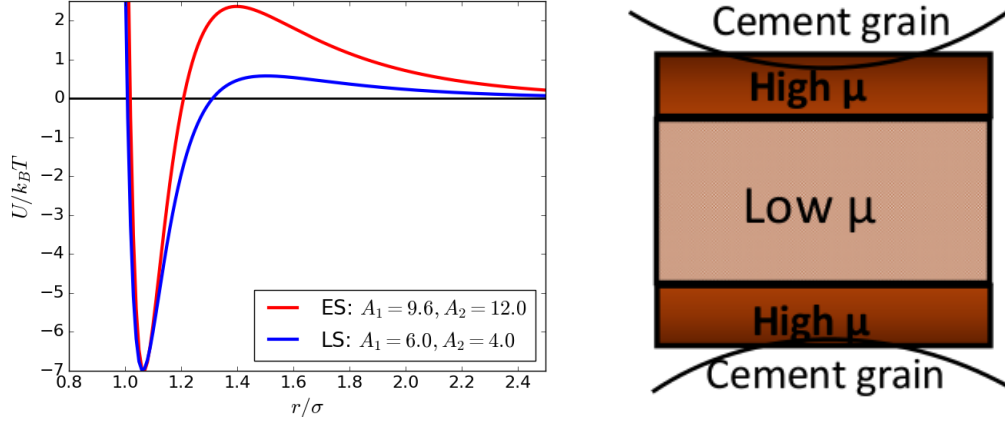


Figure 2.1: Interaction potential and chemical potential in simulations. Left: We use two sets of parameters A_1, A_2 to consider different repulsive strengths. These are labeled Early Stage (ES) and Late Stage (LS) corresponding to a high and low repulsive barrier present in early and late stages of cement setting. Right: A schematic of the variation of μ across our system. By considering a simulation volume between two cement grains, we introduce a spatial gradient in the hydration and the precipitation of C-S-H nanoparticles. The cement grain surface is not included explicitly, but rather through an effect on the local μ , turning it into a spatially varying quantity.

$$\frac{U(r)}{\varepsilon} = A_1 \left[\left(\frac{\sigma}{r} \right)^{24} - \left(\frac{\sigma}{r} \right)^{12} \right] + A_2 \frac{e^{-\kappa r}}{r} \quad (2.1)$$

where A_1 and A_2 are constants, σ and ε are the length and energy scales (discussed further in next section), and κ is the inverse Debye screening length. Due to the observation that the potential features depend on the chemistry of the cement solution [107]—which changes as cement dissolves—we consider two sets of parameters corresponding to Early and Later Stages (ES,LS) of cement hydration (Fig. 2.1, left). The ES potential exhibits a stronger repulsive barrier with $A_1 = 9.6$ and $A_2 = 12$, while the LS exhibits reduced repulsion but similar attraction with $A_1 = 6$ and $A_2 = 4$.

In the physical system, C-S-H does not exist in equilibrium conditions. In fact, as the reaction proceeds, more and more C-S-H is created from the combination of ions and water [138]. These species are not included explicitly in our model, but we mimic this precipitation via a Grand Canonical Monte Carlo (GCMC) process, where particles are inserted and deleted with a probability given by the Metropolis Monte Carlo scheme [45]:

$$P_{\text{ins/del}} \propto \min[1, e^{\pm\beta(\mu_{\text{exc}} - \Delta U)}] \quad (2.2)$$

where $\beta = \frac{1}{k_B T}$, k_B is the Boltzmann constant, T is the temperature, μ_{exc} is the excess chemical potential, and ΔU is the total change in the energy upon inserting/deleting a particle. In a closed system, μ_{exc} is associated with all the interactions between particles and depends on the density and phase equilibria.

During cement hydration, the dissolution of cement grains increases the overall concentration of ions in solution, and when saturated they combine to form a C-S-H molecule [138]. As we have coarse-grained out these degrees of freedom, the usual equilibrium chemical potential is not sufficient to describe this. Instead, we consider that the background chemistry has an effect of producing a net free energy gain with the creation of C-S-H.

With this assumption in mind, we take μ_{exc} to have two components:

$$\mu_{\text{exc}} = \mu_{\text{interaction}} + \mu_{\text{chemical}} \quad (2.3)$$

The interaction term is the usual μ_{exc} [45], while the chemical term represents the free energy gain of calcium, silicon, oxygen, and hydrogen coming together to form a C-S-H nanoparticle. While the equilibrium value of the first term can be computed (and indeed, it has, for example in [64, 150]), this chemical term is difficult to estimate. Considering that densification does not stop during cement hydration [46], previous studies have used a value of μ_{exc} that favors insertion [63].

Our scenario here is different because we want C-S-H precipitation to vary spatially. There is a tendency for C-S-H to grow at the surface of cement grains or other nucleation sites [46, 141]. If we consider our simulation box to be part of a pore between two cement grains (Fig. 2.1, right), the hydration of the cement occurs near the edges of the box, as, consequentially, does the precipitation of new C-S-H nanoparticles. To implement this, we consider $\mu_{\text{exc}}(z)$ to be a quantity that depends on position. Near the edges, a higher μ_{exc} will favor insertion, while far from the cement grains a lower μ_{exc} will discourage insertion unless it is close to existing particles.

This GCMC process is combined with Molecular dynamics (MD) of the C-S-H particles. Due to this coupling, the system exists in a non-equilibrium state where the kinetics of the reaction (mimiced by GCMC) affect the morphology of the system that evolve in time through MD. The rate R , which is the ratio of GCMC exchanges to MD steps, can be thought of as setting how fast a C-S-H particle creation occurs. When R is very high or very low, the behavior of the system would be essentially dictated by either the precipitation kinetics (GCMC) or by the dynamical aggregation (MD). However, when $R \sim \mathcal{O}(1)$, we are in a situation where the C-S-H precipitation and the particle dynamics interfere with each other to determine the gel morphology.

2.2 SIMULATION DETAILS

We use m as the unit mass, σ as the unit length, and ε as the unit energy, which defines a unit time $\tau = \sqrt{\frac{m\sigma^2}{\varepsilon}}$. The simulation volume is a periodic cubic box of side length $L = 49.2\sigma$, in which we perform molecular dynamics in an NVT ensemble with a Nosé-Hoover thermostat [45] at temperature $k_B T = 0.15\varepsilon$, which is comparable to room temperature when the interaction strength is calibrated to a modulus of 20 MPa for a C-S-H gel at early hydration times [64]. We solve the Newtonian equations of motion using the velocity Verlet

algorithm with a time step of $.0025\tau$. The GCMC and MD simulations here are done using LAMMPS [108].

For GCMC exchanges, the simulation box is split into three regions along the z -axis. The top and bottom slices are high μ regions of thickness 5σ . In the case of ES (see Fig. 2.1) we assign $\mu_{ES} = 6\varepsilon$, while for the LS case we set $\mu_{LS} = 1.5\varepsilon$. The middle region has thickness 40σ and lower values of $\mu_{ES} = -1\varepsilon$ and $\mu_{LS} = -1.5\varepsilon$ respectively. These values have been calibrated so that insertion is always preferred in the edge regions, while in the middle regions it can only happen near existing clusters.

In the simulations, the MD and GCMC parts are connected through the rate parameter R . This is the ratio of the number of GCMC exchanges to the number of MD time steps, and previous studies have found only qualitative differences when varying R over the range of $R = .5 - R = 4$ [63]. Here we present results for $R = 4$, with 400 GCMC exchanges attempted every 100 MD steps. The number of insertions/deletions varies, but there are approximately 200 of each for every GCMC cycle. As we run the MD and GCMC, particles are inserted into the initially empty simulation box, and simulations are run until $N \approx 57,000$: corresponding to a volume fraction of $\phi = 0.25$. Here ϕ is estimated considering spheres of diameter σ , and hence computed as $\phi = \frac{N\pi\sigma^3}{6L^3}$. The whole simulations requires approximately 10^6 MD steps, with variations that depend on the interaction potential. The MD time can be converted to real time (hydration time in the experiments) using the argument developed in [63], which indicates that $t_{exp} \propto \log t_{sim}$.

From the results of these simulations, we analyze the structural and morphological features. In the next section, the analysis of the clusters and of the connectivity percolation are presented in the reduced units just mentioned (m , σ , ε , τ , and unit pressure ε/σ^3), showing the gradients and anisotropies that arise due to heterogeneous growth of C-S-H. We also discuss the role of the interaction potential on these features.

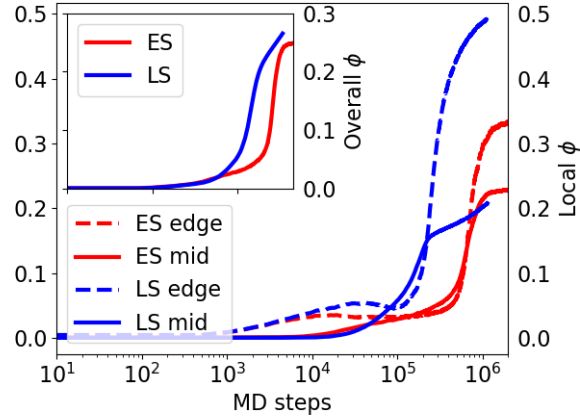


Figure 2.2: Volume fraction ϕ vs simulation time. The variation of total and local (edge,middle) ϕ as the simulations progress. With LS interactions, the non-uniform μ leads to a much larger local ϕ difference between the edge and middle regions. The formation of a locally dense, crystalline (see Fig. 2.7) layer near the cement grain surface is consistent with observations of the inner product or high-density C-S-H [32, 139].

2.3 CLUSTERS AND PERCOLATION

The choice of using a Grand Canonical ensemble allows the insertion of particles to occur at a non-uniform rate in a way that depends on the state of the system. As seen in Fig. 2.2, the total volume fraction ϕ starts to increase more rapidly as particles are inserted—until ϕ saturates due to increasing density and steric repulsion between particles.

Fig. 2.2 also shows local ϕ in the edge and middle regions, defined as the 5σ thick high μ regions and the 39.2σ thick low μ region respectively. Due to diffusion of particles from the edge, the middle region actually becomes denser than the edge for a period, starting around $t = 10^5$ MD steps. This reversal ends around $\phi = 15\%$ when the edge ϕ starts to rise rapidly. For LS, this also corresponds to a sudden decrease in $d\phi/dt$ in the middle, as the dense structure at the edge limits diffusion. For ES, the increased growth rate at the

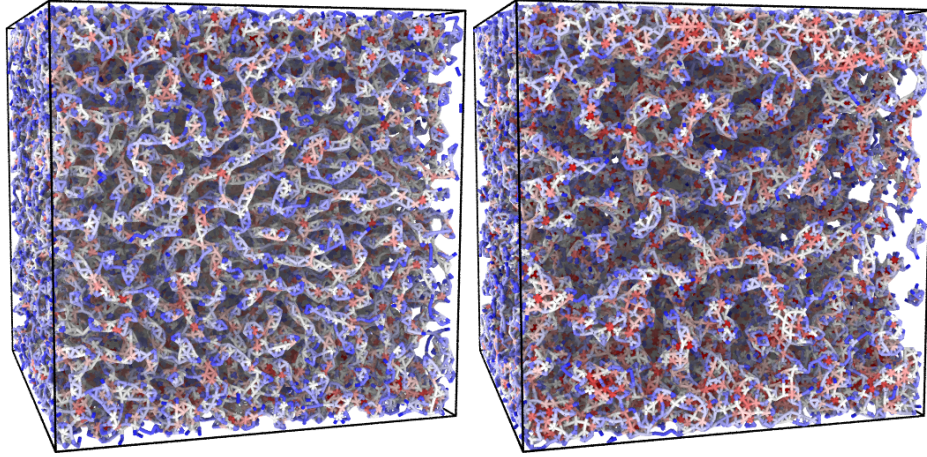


Figure 2.3: Simulation snapshots. At an overall volume fraction $\phi = 25\%$, snapshots show the microstructure for the ES potential (left) and LS potential (right). Color indicates number of neighbors (from blue=0 to red=12).

edge is correlated with an increased growth rate in the middle. This holds until $\phi \approx 22\%$, when the deletions in the low μ regions balance the diffusion from the edge region.

We see a morphological difference between the two regions which becomes increasingly pronounced as more particles are inserted. Fig. 2.3 shows that particles in at the edge tend to be more clustered and have higher coordination. In these snapshots, at $\phi = 25\%$, simulations with both potentials show the formation of a percolated, system-spanning cluster. During the simulation, as ϕ increases, clusters grow and aggregate into a connected structure, and these morphological changes also couple back to how quickly and uniformly—or not— ϕ increases. While the C-S-H clusters eventually percolate in both cases, the way that structure forms and its final morphology are quite different.

To begin examining this process quantitatively, we group particles into clusters by defining a bonding distance, r_b . We use $r_b = 1.1\sigma$ here, corresponding to a bond distance such that two particles are near the minimum of the interaction potential, after having con-

firmed that varying r_b around this value does not change our results. Note that these bonds and clusters are defined solely by instantaneous distance, but because of the interaction strength chosen ($k_B T = 0.15\epsilon$) they correspond to C-S-H particles that adhere to each other and do not continuously break and reform over time. Cluster percolation is defined as the formation of a cluster which spans the simulation box in x, y, and z directions. Fig. 2.4 shows the percolation probability, i.e. the fraction of independently generated systems that formed, in the same conditions of precipitation rate R , interaction strength ϵ , and volume fraction ϕ , a percolating connected structure. We gathered statistics from 10 independent samples for each potential. We see that, for ES, the percolation transition is more sharply defined, i.e. it happens over a narrow range of ϕ . On the other hand, with LS there is a 6% volume fraction difference between the first occurrence of a percolating cluster and 100% percolation. Interestingly, the percolation seems to correspond with the density cross-over seen in Fig. 2.2 at $\phi = 15\%$ (where the local ϕ at the edge starts to rapidly rise over that in the middle). This suggests that the percolating cluster limits particle diffusion from the edge to the middle—especially for the LS potential.

In order to understand the mechanical implications of this percolation, we looked at the build-up of internal stresses within the material. Using the virial formulation of the stress tensor, one can define a coarse-grained local stress tensor [146]. To focus our analysis on the stresses associated with particle interactions rather than thermal motion, we neglect the kinetic term and obtain:

$$\sigma_{\alpha\beta} = -\frac{1}{V_{\text{cg}}} \sum_{i \in V_{\text{cg}}} \sum_{j \neq i} \frac{1}{2} F_{\alpha}^{ij} r_{\beta}^{ij}, \quad (2.4)$$

where α and β indicate the vector components while i and j are summed over individual particles. Taking the trace of this gives us a local pressure which describes the forces a particle experiences and converges to the total pressure if we expand the coarse-graining

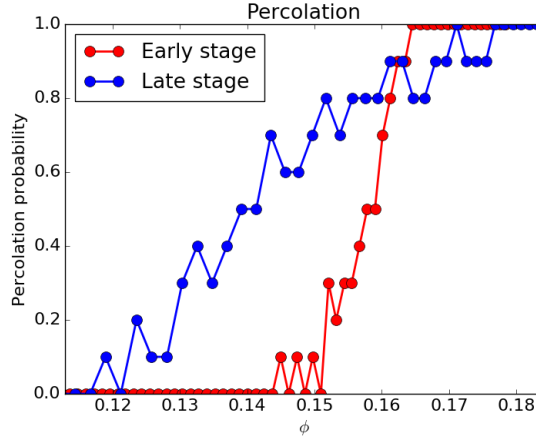


Figure 2.4: Percolation of C-S-H network. The geometric percolation probability as a function of ϕ . The particles are clustered according to a distance cutoff of 1.1σ . A cluster is considered percolating if it spans the system in x , y , and z directions. This says nothing about the persistence or rigidity of the percolating cluster, and is a geometric definition rather than a mechanical one.

volume, V_{cg} . For the results presented, we use $V_{cg} = \frac{4}{3}\pi r_c^3$, the cutoff of the potential. Small variations of V_{cg} do not produce any qualitative differences.

Fig. 2.5 shows the local pressure distributions for two values of ϕ in the edge and middle regions. They are plotted with Gaussian fit lines and show fairly normal distributions within each region. Around the percolation transition at $\phi = 15\%$ we see that ES and LS have similar distributions, but they are shifted due to the extra repulsion in ES. In both cases, there is a sharply defined value in the middle region, while the denser edges have a wider spread. Since the local ϕ in each region is roughly the same (see Fig. 2.2), it's interesting that there is such a difference in the stress distributions³, indicating that the two regions arrived at $\phi = 15\%$ through different paths, which in turn modified the local morphology and stresses.

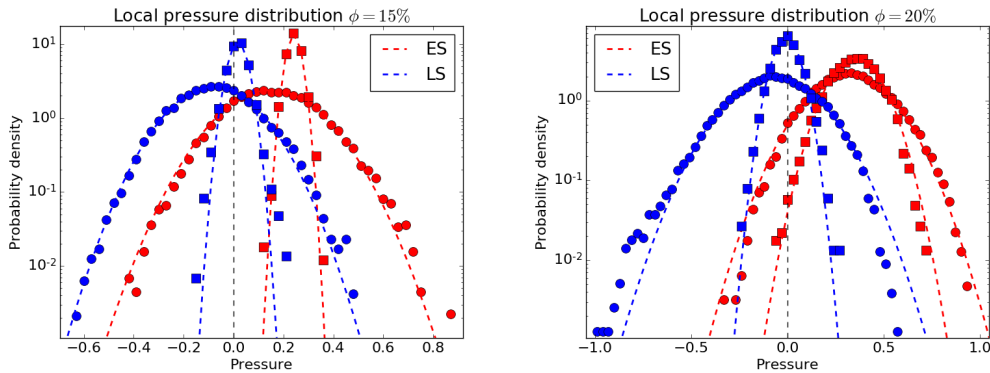


Figure 2.5: Internal stress distributions. Distributions of local pressure at the edge (circle symbols) and center (square symbols). Gaussian fits are also plotted as dashed lines.

As we add particles and go to $\phi = 20\%$, the stresses in the ES case become more uniform across the simulation box. The center distribution widens and the peak of the edge distribution shifts. Once the connected structure percolates, the stresses can be transmitted between regions, and this serves as a mechanism to reduce the initial heterogeneities introduced by the chemical potential gradient. In contrast, the LS samples maintain the extreme differences in edge vs center distributions, indicating that they are not effectively connected to allow for a stress redistribution. The geometric percolation of a cluster is enough to reduce the diffusion but not necessarily to transmit stresses, which suggests that the ES interactions are crucial to give the product an early mechanical response, as experiments have seen for cement mixtures [80].

In Fig. 2.6, we show snapshots from our simulations at $\phi = 20\%$, color coded according to local pressure. As one would expect from the stress distributions, the system snapshots show stresses that are more uniformly distributed for ES. In addition, there is no pronounced morphological difference between the edge and center regions. For LS, there is

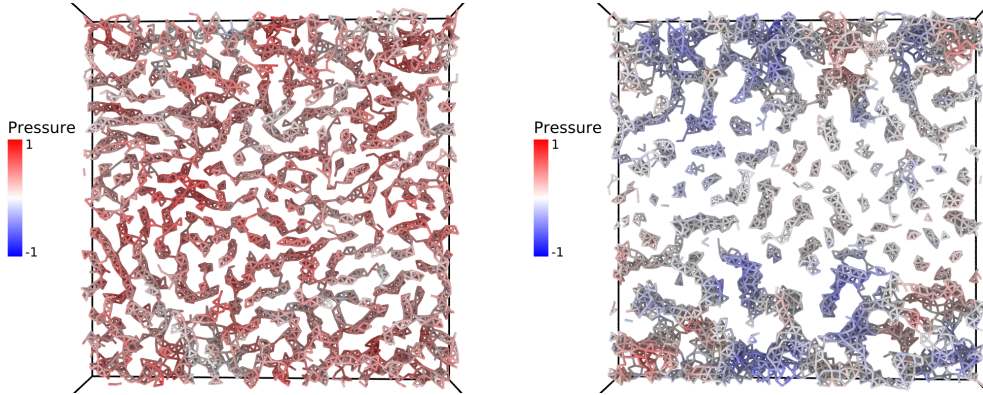


Figure 2.6: Stress snapshots. A thin (5σ) slice of our system at $\phi = 20\%$ for ES (top) and LS (bottom). The coloring corresponds to the local pressure, with red being positive pressure—i.e. parts under compression—and blue being negative pressure.

a clear distinction with most stressed areas lying on the edge of the system, which also corresponds to local structures that clearly differ from the edge to the middle.

To characterize the differences in the local structure, we computed the Steinhardt Bond Orientational Order Parameters (BOOPs) [133]. These are obtained from the angular orientation of the bonds defined by distance, the same criteria we use to define clusters. For a bond with some orientation \vec{r} , we consider the spherical harmonic function, $Y_{lm}(\theta(\vec{r})\phi(\vec{r}))$. The BOOPs, q_{lm} , are defined as an average over the bonds of a particle:

$$q_{lm}(i) = \frac{1}{N_{b_i}} \sum_{j=1}^{N_{b_i}} Y_{lm}(\theta(\vec{r}_{ij})\phi(\vec{r}_{ij})) \quad (2.5)$$

We are interested in the even l terms, which are independent of an arbitrary choice of bond direction. Since these terms are still dependent on the choice of reference frame though, we consider rotationally invariant combinations of q_{lm} . The second-order rotational invariants are

$$q_l(i) = \sqrt{\frac{4\pi}{2l+1} \sum_{m=-l}^l |q_{lm}(i)|^2} \quad (2.6)$$

and the third-order invariants are

$$\hat{w}_l(i) = w_l(i) / \left[\sum_{m=-l}^l |q_{lm}(i)|^2 \right]^{3/2} \quad (2.7)$$

where

$$w_l(i) = \sum_{m_1, m_2, m_3} \binom{l \quad l \quad l}{m_1 \quad m_2 \quad m_3} q_{lm_1}(i) q_{lm_2}(i) q_{lm_3}(i) \quad (2.8)$$

where the coefficients are the Wigner 3-j coefficients and the sum is over values such that $m_1 + m_2 + m_3 = 0$. Specifically, the set of $\{q_4, q_6, \hat{w}_4, \hat{w}_6\}$ are generally sufficient to characterize the order typical of the local packing relevant here [64]. In particular, we focus on \hat{w}_6 because it captures the difference between crystalline (fcc and hcp) and Bernal spiral ordering (the latter characterizes spirals of face sharing tetrahedra, which, as shown below, are very prevalent in certain conditions).

In Fig. 2.7 we see that both ES and LS at $\phi = 20\%$ have clear signals of Bernal spirals in the central region. At the edge, ES maintains that ordering while the denser LS shifts into a more crystalline morphology. This further demonstrates that LS is more sensitive to the spatial gradients introduced in our study. While the percolated ES system is quite uniform, with LS the percolation leads to increasing morphological heterogeneity.

The concept of two different morphological forms of C-S-H (inner vs outer, high-density vs low-density) with different elastic properties has been well established in the literature [32, 139]. The locally dense and crystalline region we observe close to the cement grain surfaces with the LS interaction could therefore mirror what is seen experimentally, as does the fibrillar form taken far from the surfaces—demonstrating how these features can arise and persist as the interactions change during cement hydration.

The heterogeneities in density, stresses, and local packing present with the LS potential arise due to the spatial gradient in chemical potential μ , and are coupled to the anisotropy that develops in the underlying network topology. In a quantitative sense, this can be probed

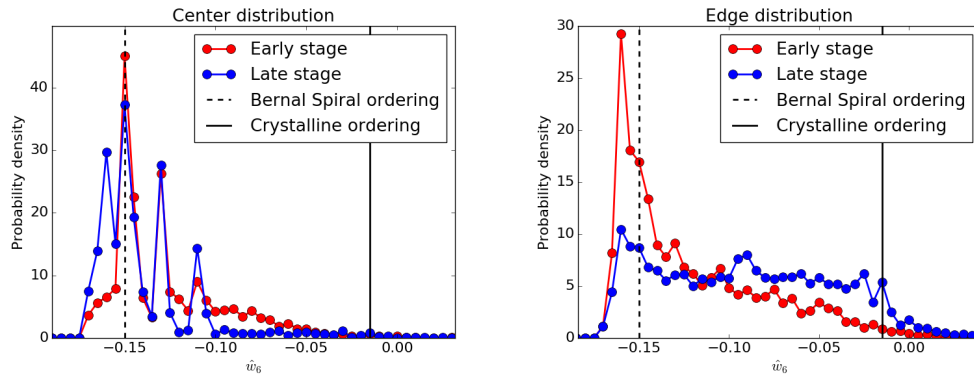


Figure 2.7: Local packing of C-S-H. The distributions of the local BOOP as first introduced by Steinhardt [133]. This provides a way to quantify the spatial differences in ordering. Here we show the rotational invariant \hat{w}_6 which is useful for differentiating between Bernal Spiral ordering and crystalline fcc/hcp ordering. The ordering observed in the center region is quite similar for both potentials, but near the edge, the LS potential forms a much denser layer (Fig. 2.2) with more crystalline ordering.

by considering a random walk on the network graph constructed from the bonds in structures analyzed so far. The corresponding mean squared displacement (MSD_g) is plotted in Fig. 2.8 as a function of the number of steps taken along the graph. The x and y directions are expected to be symmetric in a statistical sense, and unsurprisingly the MSD_g along those directions is equal. On the other hand, the z direction—the direction of the spatial μ gradient—is set up to be distinct from the others, and we’ve shown there are clear heterogeneities along this direction. These have a clear effect on the network graph as the z displacement differs from x and y for both ES and LS potentials. Notably, like the other measured properties, this difference is far more pronounced with the LS potential, demonstrating that the anisotropy in the particle insertion has been built into the network topology. Just as important is the observation that, although there is some shift, the z displacement

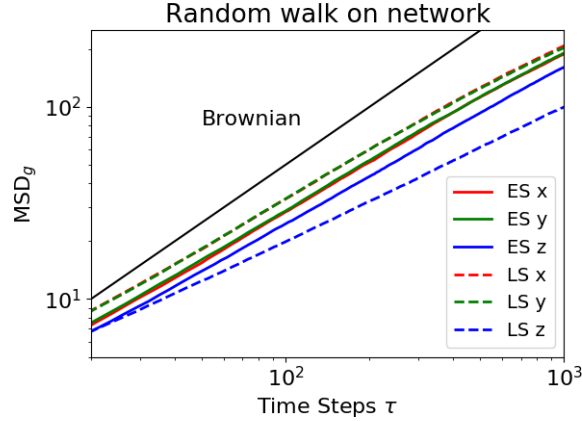


Figure 2.8: Network graph analysis. Mean square displacement (in reduced units, i.e. particle diameter squared) along x, y, and z directions from a random walk along the network graph corresponding to simulated structures from ES and LS potentials at $\phi = 25\%$. Black line indicates what purely Brownian motion would be, and MSD_g is found to be sub-diffusive. Due to the inherently anisotropic way in which the network is created, one expects and finds the displacement along z to differ from x and y. Notably, this difference, and thus the underlying anisotropy of the network, are enhanced for LS, where $MSD_g \propto \tau^{0.7}$ for the z direction instead of $\tau^{0.8}$ as in the other directions.

with ES still closely mirrors the x and y. The homogenization of stresses and ordering is coupled to an erasure of the underlying anisotropy.

2.4 POROSITY

Having characterized the solid network in terms of its percolation, internal stresses, and anisotropy, it is important to understand their implications on the associated pore network. The size, shape, and connectedness of pores not only directly affect the compressive strength, but also the long-term stability and resistance to fracture of cement. Additionally, the permeability of the pore network is crucial to the continued reaction of water and

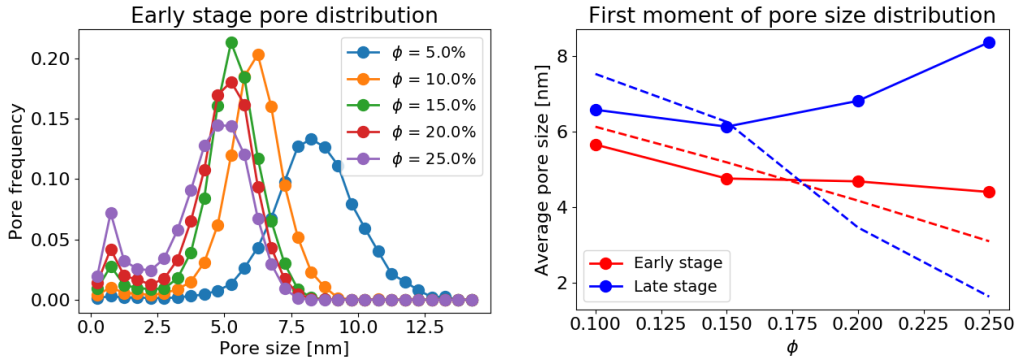


Figure 2.9: Pore size distribution (PSD) in C-S-H gel. Left: The PSD with ES potential for several volume fractions. The pore frequency describes what fraction of pore space is occupied by pores of a given radius. Right: The first moment of the PSD for both potentials as a function of ϕ . The solid line represents the low μ middle region, while the dashed line is for the high μ edge.

cement. Without this, the reaction area would be completely blocked off early in the hydration and stop the reaction.

To start, we compute the pore size distribution (PSD). This is generated using the method of Bhattacharya and Gubbins [12]. It consists of constructing a finite grid, taking points in the pore space, and determining the largest possible radius of a sphere that can fit there without overlapping any particles. This sphere is not necessarily centered at the grid point: Shor's r-algorithm is used to find a local maximum for the radius of a non-overlapping sphere, constrained to include the selected grid point. From this calculation we generate the pore frequency $p(s)$, which indicates the fraction p of the total pore space that corresponds to pores of size s . Note that this method does not provide the shape of the pores: what we obtain corresponds to the smallest linear size of the pore.

The left panel of Fig. 2.9 shows the full pore size distribution with the ES potential. We see that the peak pore size is fixed after percolation, maintaining the permeability of the

network. The increasing frequency at $s = 0.5\text{nm}$ corresponds to the packing of spherical particles in high density regions. There is no such clear trend for the LS PSD, and we must separate the edge and center regions to understand what is happening. In the right panel of Fig. 2.9, we plot the first moment of the PSD for both potentials, separated into edge and center regions, as a function of volume fraction.

Looking at the ES results through this new lens, we see that there is a difference in the porosity across the system. At $\phi = 25\%$, the $\approx 10\%$ local difference in volume fraction between edge and center leads to the pores at the edge being a bit smaller. However, relatively speaking, the density difference and consequently the pore size difference is not very large with the ES system. On the other hand, the LS system shows a remarkable transformation after percolation. The edge pores rapidly close up—just as the edge ϕ shoots up dramatically (see Fig. 2.2)—while almost paradoxically the central pore sizes start to increase with increasing particle number. This is consistent with the coarsening of the initial structure, which would lead to two separated dense C-S-H layers near the system edges. This heterogeneous pore formation has consequences for diffusion through the pores, which can be quantified by performing a random walk in the pore space.

This random walk can be thought of as the trajectory of a particle diffusing through the pores, and in Fig. 2.10, we plot the corresponding MSD. When split into x,y, and z components, the data shows that the pore network tortuosity is isotropic for ES but not LS. With LS, the x and y components are comparable to the porosity of ES, but the z direction displays a higher tortuosity—indicating reduced diffusivity through the pores. As the cement grain surfaces are modeled to be along this z direction, the diffusion is necessary for the continuation of the cement hydration. Premature closure of pores could prevent a sufficient degree of hydration being reached.

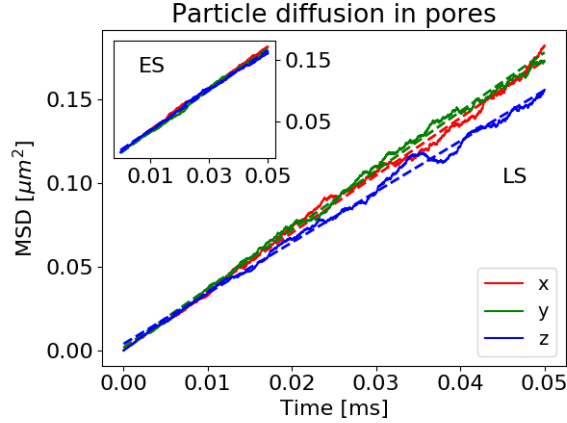


Figure 2.10: Diffusion in C-S-H pores. Diffusion through the pore space of the structures corresponding to the two potentials at $\phi = 25\%$. This is computed from a random walk in the pore space. Assuming that a particle following this random trajectory moves at some fixed speed, one can obtain the overall displacement with time. In an isotropic pore network, this displacement would be evenly split between x, y, and z directions—as in the ES case. For LS however, there is a decreased displacement along the z direction indicating an increased tortuosity of the pores along z.

2.5 SPECIFIC SURFACE AREA

Experimentally, the porosity of cement pastes can be characterized in terms of the specific surface area, S_{sp} , which is defined as the total surface area of all pores per unit mass. This is probed by scattering experiments or by measuring the ability of the material to uptake gasses such as Nitrogen or water vapor into pores. From our simulations, it is possible to calculate S_{sp} through the statistics of the pores. In particular, we first compute the pore chord length distribution, that is, the distribution of lengths l_p that randomly drawn chords can traverse in the pore space without intersecting a particle. Our results for $\phi = 25\%$ (Figure 2.11) show that the chord length distribution $p(l_p)$ for ES exhibits a local peak at $l_p = 10\text{nm}$, consistent with the data in the PSD (peaked at pore radius $s = 5\text{nm}$) of

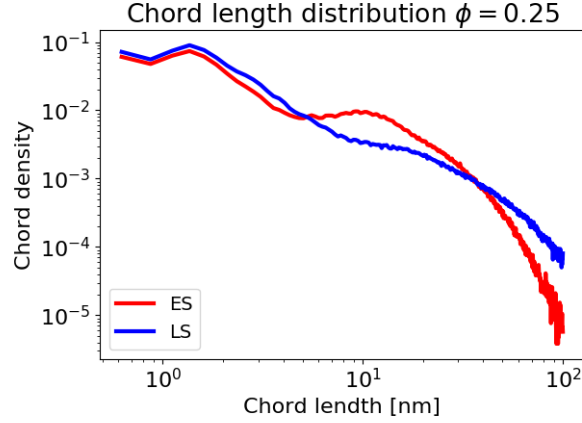


Figure 2.11: Chord length distribution in pores. The chord length distribution shows the length of chords drawn randomly in the pore space. The results with ES show a more pronounced peak at intermediate sizes due to the well-controlled pore size.

Fig. 2.9 and demonstrating that there is a characteristic size associated with the porosity for ES—a feature that is less pronounced for LS. The repulsive barrier in the two potentials introduces a length scale to our system which affects the porosity, and the strength of that barrier controls how important this length scale is.

From the mean of the chord length distribution $\langle l_p \rangle$, we calculate the specific surface area S_{sp} of our system using, according to Refs [79, 103]:

$$S_{sp} = \frac{4(1 - \phi)}{\rho \phi \langle l_p \rangle} \quad (2.9)$$

where ρ is the density of the C-S-H matrix, which is estimated to be 2.43g/cm^3 from atomistic simulations [2, 106]. Due to the discrete nature of numerical calculations, the chord length distribution is computed with a finite cutoff l_c , which affects the value of S_{sp} . To obtain the *true* surface area, one can calculate this by varying l_c and extrapolating to the $l_c = 0$ limit.

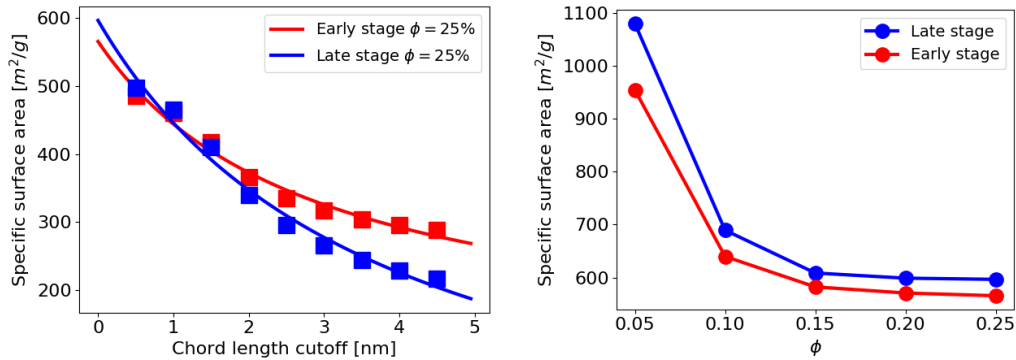


Figure 2.12: Specific surface area of C-S-H gel. Left: The specific surface area as a function of the chosen chord length cutoff. By fitting the calculated data points to $f(l_c) = \frac{A}{1+Bl_c} + C$, we extrapolate to the $l_c = 0$ limit and obtain the geometric surface area $S_{sp} = A + C$. Right: The value for specific surface area obtained by extrapolation for different volume fraction ϕ .

The specific surface area computed depends on l_c differently for the two potentials. This is something that needs to be considered when trying to compare with experimental data. Interestingly, despite the clearly different nature of the porosity for ES and LS, we actually end up with quite similar overall surface area. However, in comparison with experiments we must be careful of these different features and try to understand which parts of the porosity an experiment will be able to access. These limitations will apply differently to the two gel morphologies corresponding to ES and LS.

The values reported for S_{sp} of hardened cement paste by gas sorption experiments vary in the range of approximately $50m^2/g$ to $200m^2/g$ [10, 92, 138, 144, 145]. Meanwhile, mesoscale simulations [65] have reported values of $S_{sp} = 347m^2/g$ and $S_{sp} = 283m^2/g$ for $\phi = 33\%$ and $\phi = 52\%$ respectively. Our results are clearly significantly higher than these values, plateauing around $S_{sp} = 600m^2/g$ at $\phi = 25\%$. However, given that S_{sp} decreases with increasing ϕ , that is expected. At the very early stages of hydration, which our simu-

lations correspond to, experimental measurements are challenging due to how rapidly the material changes. Additionally, there is a significant quantity of unreacted cement at this stage, skewing possible experimental results in comparison to our simulations (which do not explicitly contain cement grains). A study by Suda et al suggests the specific surface area associated with C-S-H only is closer to $200 - 300 \text{m}^2/\text{g}$ [135]. Finally, one should keep in mind that no matter how sensitive, sorption techniques only access well-connected pores of sufficient size. If we take a larger l_c such that only pores of diameter greater than 3nm are considered, S_{sp} falls to about $300 \text{m}^2/\text{g}$. Alternatively, if we look at results from more sensitive SAXS (small angle X-ray scattering) experiments, values of $S_{sp} > 500 \text{m}^2/\text{g}$ have been reported [145, 152].

2.6 SCATTERING

In addition to measuring the specific surface area, neutron and x-ray scattering experiments have been used to characterize the microstructure of cement pastes—and are one of the most powerful tools to do so. The usual way to compute $I(\vec{q})$ is as the Fourier transform of the autocorrelation of fluctuations in local density, $\eta_2(\vec{r}) = \frac{1}{V} \int d^3 r' (\rho(\vec{r}') - \bar{\rho})(\rho(\vec{r}' + \vec{r}) - \bar{\rho})$, of our simulated microstructures (Fig. 2.13), where $\rho(\vec{r})$ is the local density and $\bar{\rho}$ the average density [19]. In case of an anisotropic medium, this computation is more involved due to the need to compute $\eta_2(\vec{r})$ for each orientation of \vec{r} prior to performing the 3D Fourier transform.

A second way, more numerical tractable, was proposed in [20, 44]. This a two-step process. First a projection image of the chosen 3D binary structure is performed either along the x or y or z direction. Second, a 2D Fourier transform of this projection is calculated. The associated spectral density gives directly $I(q_x, q_y, q_z)$ with either $q_x = 0$ or $q_y = 0$ or $q_z = 0$. For example, the projection along the optical axis x will allow one to get the 2D

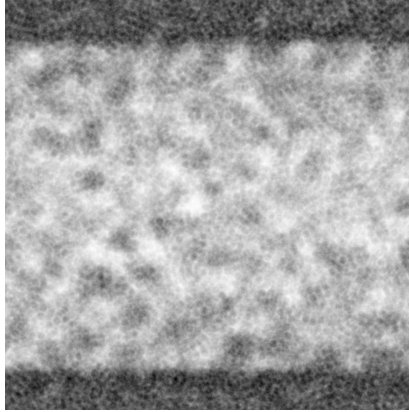


Figure 2.13: Scattering cross-section. A 2D projection of local densities in the LS structure at $\phi = 25\%$ when looking down the y -axis. The darker regions correspond to higher density. Scattering intensity $I(q)$ can be computed from the autocorrelation of fluctuations in the local density, $\eta^2(r)$.

pattern $I(q_x = 0, q_y, q_z)$. To estimate the level of anisotropy, an angular average along the principal directions of these 2D scattering patterns is performed using a averaging angle of 15 degrees. A comparison of the two methods is presented in [44], showing a very good agreement.

Due to the anisotropy in the structure, the choice of optical axis for the scattering naturally affects the results obtained. Due to the symmetries in our system, the x and y directions are equivalent—anisotropy is associated with the z , i.e. μ -gradient, direction. If one considers an optical direction along a non- z axis, the μ and density gradients produce clear differences in the low q scattering intensity along the z direction compared to the x or y (Fig. 2.14). For both ES and LS potentials, the scattering along z exhibits low q structure (instead of a plateau as along x or y), which is consistent with the system-spanning density gradient along z . The high q scattering is instead dominated by the oscillations typical of monodispersed spherical particles [54].

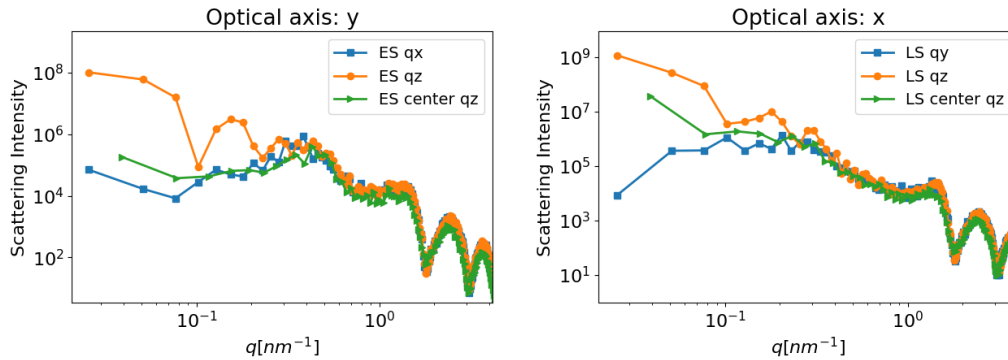


Figure 2.14: Scattering intensity. The scattering intensity is computed for both potentials for various different optical axes. The intensity is split into components along different directions to highlight anisotropy. The scattering component along z differs from the others at low q due to anisotropy in the structure. Surprisingly, for ES this effect is suppressed if we consider only the center region—meaning all of the measured anisotropy is due to the density variation across the whole box. Meanwhile, for LS, even the center region alone deviates from the x and y scattering. The structure is anisotropic even at scales smaller than the system-wide μ gradient. The high q oscillations are consistent with having monodispersed spherical particles

One can also consider just the scattering from the center region of the system (green triangles in Fig. 2.14). Limiting ourselves to this region reveals an interesting difference between the two potentials. With LS, the z scattering deviates from y scattering in the low μ center region as well—highlighting that the anisotropy in the structure goes beyond the large difference in density, stresses, porosity, etc. between the edge and center regions. On the other hand, for ES, this split leads to a suppression of scattering anisotropy and produces a curve which matches the scattering along x. This suggests that the anisotropy is due entirely to the differences between the high and low μ regions.

The anisotropy induced by the cement grain surfaces manifests itself in our calculated scattering intensity. For a macroscopic sample, these grains would be distributed randomly and give an overall isotropic response due to the statistical averaging of the results. The

isotropic $I(q)$ has been computed using similar mesoscale models for high volume fractions [65], and it was found to match experimental measurements of scattering intensity. It is difficult to make such a connection using our simulations due to limitations of system size at low q and the effects of particle size monodispersity at high q . Nonetheless, this calculation has revealed interesting differences in the anisotropy of ES and LS systems. Future studies can expand on this to make a direct connection to scattering experiments.

2.7 CONCLUSIONS

We used MD and GCMC simulations to investigate the effect of C-S-H growth in the presence of spatial gradients of C-S-H precipitation and of the changing effective interactions between C-S-H nanoparticles on the overall morphology of the C-S-H gel. By using the GCMC to mimic precipitation of nanoparticles, we observed how the precipitation at cement grain surfaces leads to spatial gradients in density that develop over time but depend on the features of the C-S-H interactions. With the ES interaction, we discovered a percolating cluster that forms around $\phi = 15\%$ with reduced density and stress gradients, as well as network anisotropy, relative to the LS interaction. Calculations of pore size and diffusion in the pores demonstrated that these differences in the gel morphology translated into coarsening pores and an increase in pore tortuosity along the gradient direction for the LS system. Finally, we computed specific surface area and scattering intensity to make a connection to experimental methods of characterizing cement microstructure.

The heterogeneous growth of C-S-H nanoparticles clearly has an effect on the morphology of the gel that is formed, and this effect of spatial gradients in the C-S-H precipitation is controlled by the features of the interaction potential between the C-S-H nanoparticles. The non-contact repulsion that is present in early stages of hydration due to electrostatics plays a crucial role in the formation of a percolated and stress-bearing network with

limited anisotropy. It also helps to prevent the formation of large pores due to coarsening, while maintaining diffusivity in the pores. These features are necessary to the continuing hydration of cement grains and the formation of a connected solid structure. As the interactions evolve over time, the presence of the cement grain surfaces can drive the formation of spatial gradients in C-S-H density as well as differences in local packing and density—consistent with the two distinct morphological phases of C-S-H observed in the literature [32, 139].

Our study provides further support to the idea proposed by Ioannidou et al: the natural time-evolution of the interaction between C-S-H nanoparticles is crucial to attaining the final mechanical strength through a complex tuning of the gel morphology [64]. Not only are the differences in the interactions maintained under spatial gradients of C-S-H precipitation, they are enhanced. And in the context of heterogeneous C-S-H nucleation, the features of the early stage interactions are required to explain how cement setting can be such a complex but robust process. These discoveries give insight into how the growth of nanoscale components builds up the overall microstructure of cement hydrates and how it depends on the interactions between the nanoparticles. Such insight is an important step towards understanding how an alternative cementitious material could behave through the changes in chemistry and thus the effective interactions.

One consequence of this work is that the effective interactions between C-S-H nanoparticles are seen to strongly affect the growth and gelation of C-S-H. However, as I discussed in the Sec. 1.3, those interactions clearly depend on the cement chemistry, yet it has remained unclear what specific ingredients control the interactions and lead to the evolving cohesion during hydration. While it is understood that the electrostatics of Calcium ions progressively confined between developing C-S-H surfaces is at the core of the problem, existing theories do not apply in conditions relevant to cement, i.e. high surface charges and multivalent ions. In my thesis work, I have developed a quantitative approach, again based

on numerical simulations, to understand the emergence of the cohesion between C-S-H nanoparticles during cement hydration. The next two chapters are dedicated to this work, in particular by setting a comparison to the PM approach described in Ch. 1. I will start by discussing the need for a more detailed description of the solvent, water, and the model I decided to work with.

CHAPTER 3

A SEMI-ATOMISTIC MODEL FOR ELECTROSTATICS IN CONFINED WATER

In the previous chapter, I described the mesoscale C-S-H gel and pore networks. These networks show gradients and anisotropies due to the heterogeneous growth of C-S-H from cement grain surfaces, but these features are highly dependent on the effective interactions between the C-S-H nanoparticles. These interactions were observed to depend on the cement chemistry (Fig. 1.3), yet it has remained unclear how specific ingredients (ion specificity/confinement, surface charge) control the interactions and lead to the strong cohesion at the end of hydration. PM simulations, going beyond mean field theories, demonstrate that attraction can arise between C-S-H-like charged surfaces due to ion-ion correlations. However, the predicted cohesive strength for C-S-H in the hardened cement paste is multiple orders of magnitude too low to compare to atomistic simulations [89] or experiments [93, 148] in the hardened paste. This discrepancy is too large to be explained by small details: important physical effects are missed by the PM description. In this chapter, I will explain the model I decided to work with, starting from the need to capture water restructuring and its effect on ions in confinement.

3.1 PROBLEMATIC TREATMENT OF CONFINED WATER

Water is, in fact, a highly complex fluid, that is notoriously challenging to model [98]. Water molecules have a high dipole moment (1.855 Debye) in isolation, and are polarizable so that the condensed phase is observed to have moments in the range of 2.4 to 2.6 D [53].

Due to the partial charges on H and O atoms, liquid water readily forms hydrogen bond networks, and the connectivity of these networks lies well above the percolation threshold [124]. However, despite the bonding energy being greater than the thermal energy, the diffusivity of water is comparable to that of unconnected simple liquids [124]. In addition to short-ranged ordering from hydrogen bonds, there is a long-ranged contribution to the forces between water molecules from their dipole moments. Dipolar fluids have been demonstrated to exhibit structure at all length scales [75].

The situation is further complicated by the confinement, as water behavior is strongly affected by confinement, including modification of density and dielectric properties [9, 123, 125]. Due to geometric constraints, water structure is greatly altered, leading to water layering being observed in simulations for a wide range of systems, including atomistic simulations of C-S-H [38, 48, 89, 90]. This means that water density differs from the bulk and depends on the level of confinement. The modification of density also affects dynamics and phase behavior.

Of particular relevance is the demonstration of a drastically reduced (and locally varying) dielectric constant in simulations of water confined by charged surfaces [114]. There is also experimental evidence that the water restructuring near an AFM tip reduces the dielectric constant of water [140]. Interestingly, the topological constraint induced by the mere presence of a surface, regardless of surface properties, is found to slow water dynamics in experiments [100]—suggesting the key here is the water behavior rather than the surface properties. Could this change in water properties be the source of the large discrepancy between the PM, with water treated implicitly with a bulk dielectric constant, and atomistic simulations or experimental measurements?

3.2 EXPLICIT SOLVENT WITH CLAYS

Seeking to answer this question, we have drawn inspiration from the PhD thesis of Benoit Carrier, in which he tackles the same question in the context of clays [24]. Like C-S-H, wet clays are made up of charged particles in solution with counter-ions. Clay particles are much coarser, up to microns in size, the types of ions are different, and the cohesive strength does not compare to hardened C-S-H. Nonetheless, the underlying physical question about the microscopic mechanisms for electrostatic cohesion is the same.

In the thesis, Carrier does both PM and atomistic simulations of clays, and he goes on to introduce an explicit solvent primitive model (ESPM) in which water molecules are included as soft spheres with a point dipole [24]. By explicitly including the solvent, the dielectric properties can arise from the fluctuations of these dipoles rather than being an imposed constant as in the PM. This allows for the dielectric “constant” to actually be a function of the confinement and ion concentration, as it is in atomistic simulations. It also captures some of the water structuring due to confinement—though notably, the lack of a quadrupole moment means there is no hydrogen bonding or tetrahedral structure.

This model is investigated as an intermediate between the PM and fully atomistic simulations, ideally capturing important physics the PM misses without increasing the computational cost too much. The inclusion of water was found to dramatically alter the computed forces, qualitatively as well as quantitatively. Carrier was able to see cases of attraction between clay surfaces where the usual PM predicted repulsion (Fig. 3.1), indicating that the solvent plays a role in creating the cohesion [24].

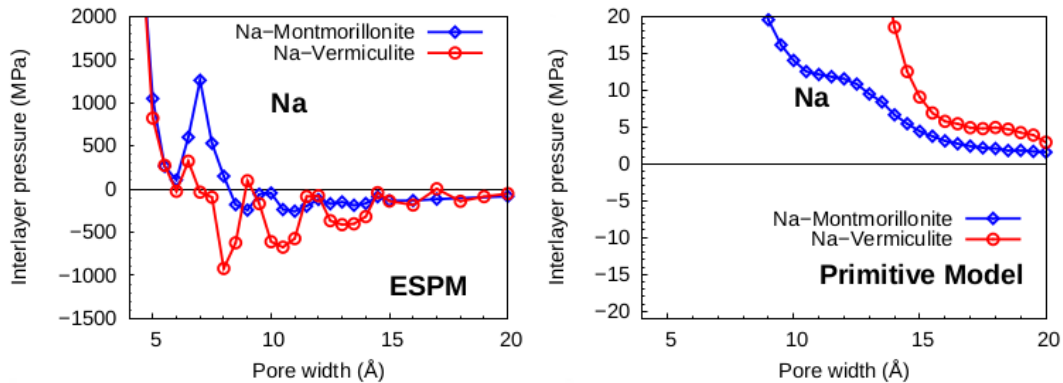


Figure 3.1: Explicit solvent model in clays. ESPM simulations (left) show attraction between clay surfaces in cases where the PM (right) predicts only repulsion [24]. Two types of clay are considered, in solution with Sodium counter-ions, and ESPM simulations show electrostatic attraction at certain distances for both clays.

This demonstration of the effect that explicitly including the solvent has for clays is a strong indication that it is also important for modeling the net interaction between C-S-H surfaces. But what about the explicit solvent is so important in correctly predicting the forces? If we can understand this mechanism, it will make it much clearer how the changing conditions during cement hydration play into the development of C-S-H cohesion.

3.3 SEMI-ATOMISTIC APPROACH FOR CALCIUM-SILICATE-HYDRATES

We need a realistic model that can capture the complexities of the water behavior but still allow one to explore different conditions (surface charge density, ion type and concentration, etc.). In the next chapter, I will discuss my results, including the overall interaction between C-S-H particles, the microscopic mechanism that I find is responsible for that, and how that can arise during cement setting. I will also talk about the comparison with analytic theory developed by our collaborators. But before all that, I will explain the model we developed and its parameters in detail.

3.3.1 THE INGREDIENTS

Building on the framework of the PM, and Carrier's extension with an explicit solvent, I start with a system that is 2D periodic and confined by charged surfaces in the z direction. Ions are included explicitly as point charges in a soft sphere. Water is also treated as an explicit solvent.

Since the first computer simulation of liquid water, by Barker and Watts in 1969, there have been over a hundred different proposed water models [98]. The strategies employed have ranged from empirical models using effective point charges to a focus on polarization and many-body effects. The extensive hydrogen bonding network of water is dependent on rather subtle details of its quadrupole moment (and the balance with short-range, steric repulsion), but it also has a high dielectric constant and long-ranged order associated with its strong dipole moment [132]. As the behavior depends both on the magnitude and relative values of the moments, improving the model in regards to one property can make it worse for others [39].

While it may not be possible to capture all features of water behavior, Carrier's work [24] suggests that even a simple water model could be enough to capture several important effects that implicit solvent models like the PM missed. The SPC/E model [11] is widely used due to its ability to capture several features of water structure [87] with computational efficiency. In order to make direct quantitative comparisons with the analytical predictions, a simpler dipolar model (similar to what is used by Carrier [24]) was also used in some cases. This model consisted of a soft sphere with an embedded point dipole.

To account for the finite size and dispersion interactions of ions, water, and the walls (C-S-H surfaces), I used a Lennard-Jones potential (LJ):

$$U_{\text{LJ}}(r) = 4\epsilon \left[\left(\frac{\sigma}{r} \right)^{12} - \left(\frac{\sigma}{r} \right)^6 \right]. \quad (3.1)$$

In the SPC/E model, there is one LJ site per water molecule situated at the Oxygen atom, and I use the same scheme for the dipolar water model. The LJ parameters for the ions are taken from Cygan et al [34] (more on this in the next section). The specific values used for the LJ d and ϵ are: $d = 2.87\text{\AA}$ and $\epsilon = 0.1\text{kcal/mol}$ for Ca-Ca, $d = 3.166\text{\AA}$ and $\epsilon = 0.155\text{kcal/mol}$ for water-water, and $d = 3.018\text{\AA}$ and $\epsilon = 0.127\text{kcal/mol}$ for Ca-water.

In addition, the walls (C-S-H surfaces) have a similar potential that just varies with the z distance perpendicular to the surface:

$$U_{\text{wall}}(z) = 4\epsilon \left[\left(\frac{\sigma}{z} \right)^{12} - \left(\frac{\sigma}{z} \right)^6 \right]. \quad (3.2)$$

The wall LJ parameters are the same as those of water (corresponding to Oxygen atoms).

The final ingredient is the Coulomb forces. Calcium ions have a charge of $+2e$. Water is overall neutral, but it has a very strong dipole and quadrupole moment: features that strongly affect its properties as a solvent. The SPC/E model implements this via partial charges associated with the O and H atoms in fixed (relative to each other) positions. The dipolar model I implement is simpler and includes only a point dipole with a moment of 1.8 Debye. This clearly will not reproduce the more complex tetrahedral structure of water, which the SPC/E model manages to do, and the main relevance is to enable comparisons with the analytical predictions. Finally, the walls are considered to have equal surface charge densities, and since they are infinite planes, this produces no net electric field.

3.3.2 DISPERSION INTERACTIONS

It is important to correctly account for the dispersion forces between ions, water, and C-S-H surfaces. To do this, I use a LJ potential. ClayFF is a force field that parameterizes LJ terms for the various species of atoms that are of interest when studying clays [34], and there is a lot of overlap for C-S-H.

As a check, I computed the expected interaction term between Oxygen atoms (such as those in water) via the Pn-Traz method of Pellenq and Nicholson [104]. Two spherically symmetric atoms, separated by a distance R , will exhibit long-range dispersion interactions due to correlations in charge fluctuations, and generally this interaction will have the following form:

$$u_{disp}(R) = -\left\{\frac{C_6}{R^6} + \frac{C_8}{R^8} + \frac{C_{10}}{R^{10}} + \dots\right\} \quad (3.3)$$

As a first estimate, I will be focusing on the R^6 term (which has the largest contribution). This term represents interactions between two instantaneous dipoles. The coefficient is given by [104]

$$C_6 = \frac{3}{\pi} \int_0^\infty \alpha^A(i\omega) \alpha^B(i\omega) d\omega \quad (3.4)$$

where α is the dipole polarizability for each of the atoms A and B. These polarizabilities can be expressed in terms of the energies and dipole moments associated with ground state to excited state transitions as

$$\alpha(i\omega) = \sum_{n=1}^{\infty} \frac{f_n}{\epsilon_n^2 + (i\omega)^2} \quad (3.5)$$

where ϵ_n is the energy of the n th state transition and f_n is a quantity associated with the energy, dipole moment, and probability of such a transition. It is defined as [137]

$$f_n = \frac{8\pi}{3} \epsilon_n |\langle \psi_0 | \sum_j r_j Y_1^0(\cos\theta_j) | \psi_n \rangle|^2 \quad (3.6)$$

where the sum is over the electrons and Y is the spherical harmonic function. Note that this is defined in atomic units, and there is an implicit factor of e^2 . The squared term can be understood as the square of the dipole moment of the n th state weighted by the probability of that transition.

In this method of computing dispersion interactions, the main simplification is the use of Padé approximation, a mathematical technique used to estimate a function of a single variable (analogous to a truncated Taylor series). This gives the following single term approximant for the dynamic polarizability:

$$\alpha(i\omega) = \frac{\alpha(0)\eta^2}{\eta^2 + \omega^2} \quad (3.7)$$

where η is an energy parameter that will be discussed in greater detail later. Combining the above approximation with the identity

$$\frac{2}{\pi} \int_0^\infty \frac{ab}{(a^2 + x^2)(b^2 + x^2)} dx = \frac{1}{a+b} \quad (3.8)$$

allows us to simplify equation 6 to:

$$C_6 = \frac{3}{2} \frac{\eta^A \eta^B}{\eta^A + \eta^B} \alpha^A(0) \alpha^B(0) \quad (3.9)$$

This formulation only depends on the static polarizability of the two atoms and a suitable choice for the energy parameter η .

η can be chosen to find upper or lower bounds for $\alpha(i\omega)$ [137]. Here we choose $\eta = \sqrt{\frac{S(0)}{\alpha(0)}}$, where $S(k) = \sum_n f_n \epsilon_n$, which gives us an upper bound. The main advantage here is that this sum can be related to the number of electrons in an atom, allowing us to estimate this for a general species. Specifically, this sum is equal to the effective number of electrons, N_{eff} , which is related to the number of outer shell electrons, N .

$$N_{eff} = aN^2 + bN + c \quad (3.10)$$

The values of a, b, c depend on the number of electron shells in the atom, and specific values are tabulated in the paper of Pellenq and Nicholson [104]. This choice is found to give results that are about 10% too high for C_6 .

Having made the above approximations and chosen the parameters, the expression for C_6 becomes very simple. For two atoms of the same type, equation 11 reduces to:

$$C_6 = \frac{3}{4} \sqrt{N_{eff} \alpha(0)^3} \quad (3.11)$$

Our interest is in the interaction between C-S-H and water. For water, we will focus on the dispersion interactions of the Oxygen atom as is commonly done in water models. C-S-H is a more complex molecule, but the outermost atoms are Oxygen. As a first approximation, we will compute the Oxygen-Oxygen interaction.

The polarizability and effective number of electrons for Oxygen depend on the molecular structure within which it exists. For parameters corresponding to SiO₂ and MgO, C_6 is found to be 38.8248 and 74.2078 respectively.

LJ parameters for the particles are taken from ClayFF [34]. For Ca-Ca: $d = 2.87\text{\AA}$ and $\epsilon = 0.1$ kcal/mol, for water-water: $d = 3.166\text{\AA}$ and $\epsilon = 0.1554$ kcal/mol, and for Ca-water: $d = 3.018\text{\AA}$ and $\epsilon = 0.127$ kcal/mol [34]. In comparison to the calculated coefficients, the LJ parameters we have from ClayFF give $C_6 = 45.4306$. As this falls between the two computed values, it seems like this force field does a good job representing the dispersion interactions.

3.3.3 COULOMB FORCES AND EWALD SUMMATION

Since Coulomb forces are long-ranged, simply having a force cutoff would lead to large errors in the calculation, and the sum of Coulomb forces from all periodic images of the system is actually only conditionally convergent (i.e. it will only converge for certain summation geometries). A more efficient and reliable method is the use of Ewald summation [5, 41]. This is a method for summing the electrostatic forces in Fourier space that converges absolutely. The key feature that enables this is splitting the Coulomb interaction into two terms:

$$\frac{q^2}{r} \rightarrow q^2 \left(\frac{f(r)}{r} + \frac{1-f(r)}{r} \right), \quad (3.12)$$

where $f(r)$ is chosen so that $\frac{f(r)}{r}$ is short-ranged and can be computed directly up to a cutoff distance, while $\frac{1-f(r)}{r}$ has a negligible Fourier transform for large values of k . The common choice is to use the complimentary error function:

$$f(r) = \text{erfc}(r) = \frac{2}{\sqrt{\pi}} \int_r^\infty e^{-t^2} dt. \quad (3.13)$$

By splitting the potential in this way, it is possible to truncate the sums in r and k . This introduces an error in the energy that scales as $\frac{M^2}{V(\epsilon_S)}$, where M is the net dipole moment in one periodic image, V is the volume of that image, and ϵ_S is the dielectric constant of the surrounding medium [131]. By taking our "infinite" system to be surrounded by a conductor, this term vanishes and we recover the correct energy. In other words, the Ewald sum gives the result for summing the Coulomb forces from a large sphere of periodic images in spherical coordinates then taking the material outside this sphere to be a conductor.

Although this method has been derived for a 3D periodic system, it can be applied to a 2D periodic slab geometry (where one dimension, which we'll refer to as z , is finite). This is done by adding a large vacuum space in the z direction and then making the system periodic. Effectively, we produce infinite slabs that are separated by large vacuum spaces.

Recall that the true Coulomb sum depends on the order of summation, so the usual Ewald sum is exact only for one summation geometry and requires a correction for other geometries. Yeh and Berkowitz showed that treating the slab system as 3D periodic, with some vacuum space inserted between slabs, is accurate given the addition of a geometry-related correction term to the energy [154]. For the slab geometry, this term is:

$$E(M, \text{slab}) = \frac{2\pi}{V} M_z^2 \quad (3.14)$$

where M_z is the z component of the total dipole moment of the simulation cell [131]. Adding this correction term to the standard 3D Ewald summation allows accurate computation of the sums—while without it, the convergence to 2D results remained unsatisfactory even

when the vacuum space is significantly larger than the simulation cell [154]. This term has a contribution to the z component of the force equal to

$$F_{z,i} = -\frac{\delta}{\delta z_i} E(M, slab) = -\frac{4\pi q_i}{V} M_z \quad (3.15)$$

3.3.4 WATER DENSITY

As mentioned already, water in confined geometries (especially in the presence of charges) can have a density that is different from bulk water. To select the number of water molecules for the simulations, I first performed Grand Canonical Monte Carlo based on the chemical potential of bulk water (room temperature, density). Simulations in bulk conditions showed that chemical potentials of $\mu = -2$ kcal/mol and $\mu = -8.8$ kcal/mol gave the correct water density for the dipolar and SPC/E models respectively. GCMC simulations with these values can be used to produce the water density profile under confinement.

In general, the chemical potential represents the free energy change due to adding a particle. It can be broken down as:

$$\mu = \mu_{ideal} + \mu_{excess} \quad (3.16)$$

The ideal gas contribution is due to the entropy associated with confining the particles in a certain volume: $k_B T \ln \rho \Lambda^3$, where ρ is the number density and Λ is the thermal De Broglie wavelength. The excess term is the result of water interactions with other water molecules, ions, and the walls.

In the Grand Canonical ensemble, the probability of states with $N + 1$ particles relative to N particles must be given by:

$$\frac{p_{N+1}}{p_N} = \frac{V}{\Lambda^3(N+1)} e^{-\beta(\mu - \Delta U)} \quad (3.17)$$

where $\beta = k_B T$ and ΔU is the total change of interaction energy due to the inclusion of an additional particle. This can be maintained using the Metropolis method by attempting

insertions/deletions with equal probability, and accepting them with the following probabilities [5]:

$$p_{ins} = \min\left[1, \frac{V}{\Lambda^3(N+1)} e^{\beta(\mu-\Delta U)}\right] \quad (3.18)$$

$$p_{del} = \min\left[1, \frac{\Lambda^3 N}{V} e^{-\beta(\mu-\Delta U)}\right] \quad (3.19)$$

3.3.5 DIELECTRIC PROPERTIES

The dielectric response of a material can be quite complex at the atomic level. While the dielectric constant ϵ_w is a macroscopic quantity, it arises from this complex microscopic behavior. Even ignoring how the confinement in our system would change the macroscopic ϵ_w , trying to use this ϵ_w for interactions at the nanoscale (as in the PM) has a host of problems. With numerous charges enclosed in a small volume, the polarization of the solvent would depend non-trivially on the arrangement of all the ions and solvent molecules, so taking it to behave the same as in the macroscopic material exposed to an external field is a very strong assumption.

Explicit inclusion of the solvent allows one to directly incorporate this as a microscopic phenomenon. Unfortunately, this is a feature that is actually quite difficult to capture correctly, and many water models that give otherwise similar results produce drastically different values for the dielectric constant. Sprik et al compared several different models and found that the value of the dipole moment played a large role in the dielectric constant, even for models that were otherwise very similar [132]. Other studies have found that the higher order terms in the electrostatic interactions mainly play a role in the local structuring of a fluid, while the dipole moment is longer-ranged and strongly impacts the dielectric properties [1]. Achieving a perfect balance has proven to be difficult as the adjustment of parameters to improve accuracy of one can inadvertently reduce the accuracy of the other [39].

In MD simulations, the standard way to compute ϵ_w is from the total dipole moment, M [52]. ϵ_w can be related to M through the fluctuation-dissipation theorem. Specifically, $\epsilon_w = 1 + \chi$, where χ is the electric susceptibility, and the fluctuations in M are related to its dissipation through χ . For an isotropic system $\langle M \rangle = 0$ and the variance of M is simply $\langle M^2 \rangle$, so we get:

$$\chi = \frac{1}{\epsilon_0 V k_B T} \frac{\langle M_x^2 + M_y^2 + M_z^2 \rangle}{3} \quad (3.20)$$

In real water, an external electric field would both align dipole moments and induce polarizations, but our model has no mechanism for that kind of polarization. Similarly, induced polarization causes the dipole moment of real water (measurements range from 2.4 – 2.6 Debye) to differ from the value associated with an isolated molecule (1.855 Debye) [53]. We selected the dipole moment in our dipolar water model by matching the dielectric constant of real water: which worked out to 1.8 Debye. With the SPC/E model, the dipole moment is 2.35 Debye, which is closer to experimentally reported values in liquid water ranging from 2.4 – 2.6 Debye [53]. However, the SPC/E model gives a slightly lower bulk dielectric constant of $\epsilon_w \approx 71$ instead of 80 [136].

3.4 SIMULATIONS

Having developed a detailed and realistic semi-atomistic model for water and ions confined by charged surfaces, it can now be applied to investigate the physical phenomena underlying like-charge attraction. In the next chapter I will delve into how this arises in C-S-H during cement hydration. First, I will describe how I perform simulations using this model and, in Sec. 3.5, how this alters water properties compared to the bulk liquid and other studies of water in confinement.

Simulations are done using LAMMPS [108]. I consider a slab geometry which is finite in the z direction and periodic in x and y (the charged surfaces being at $z = 0$ and $z =$

D). 64 Calcium ions are confined in this system. For a surface charge density of $\sigma = 3e^-/\text{nm}^2$, the *xy* size is fixed by the electroneutrality condition at $L_x = L_y = 46.2\text{\AA}$. This value of σ corresponds to C-S-H in the hardened cement paste, but early during hydration the hydrates have a less defined form and can have lower surface charges. While there is not a quantitative timeline of the surface charge, I will consider the qualitative effects it has by varying σ . For each value of σ and the surface separation *D*, independent simulations are performed.

The procedure consists of two steps: 1) insert water to reach equilibrium density and 2) sample the equilibrium states. The first step involves GCMC (Grand Canonical Monte Carlo) done in conjunction with some MD (Molecular Dynamics) steps so that the system can quickly explore various configurations. Specifically, 1000 GCMC exchanges are attempted every 1000 MD time steps (each time step is 1 fs). This is continued until water density reaches a plateau, and this is taken as the equilibrium water density for that system. I found $3 * 10^6$ MD steps, or 3 ns to be a sufficient amount of simulation time to reasonably ascertain the densities. The second stage consists of pure MD in an NVT ensemble. During this process, macroscopic and microscopic data is outputted, and a variety of statistical tools are used to examine both the overall interaction pressure and the microscopic mechanisms that give rise to it.

3.5 WATER PROPERTIES IN CONFINEMENT

One motivation for using explicit water is the large modification of water properties under confinement, and it is reassuring to find that the water properties I observe are consistent with studies on confined water in other contexts [9, 48, 114, 123, 125, 155]. In this section, I present results for the water properties in confinement by surfaces with charge density $\sigma = 3e^-/\text{nm}^2$, which is on the order of C-S-H in the hardened paste, using both the SPC/E and

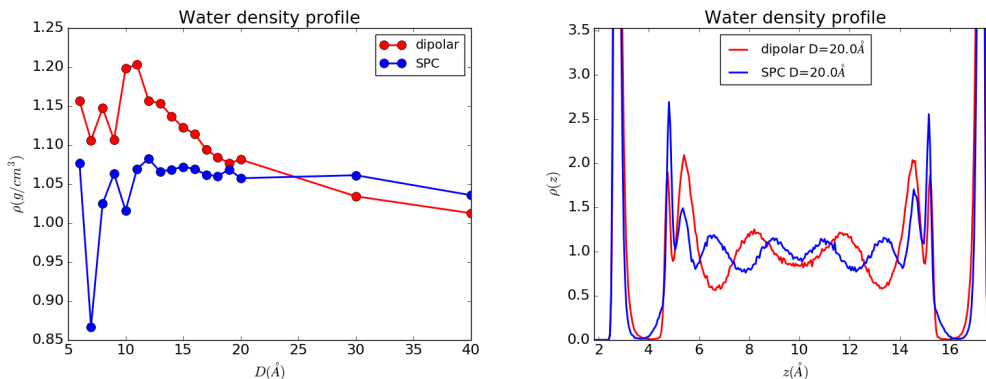


Figure 3.2: Water density in confinement. Left: Water density from GCMC simulations as a function of confinement. Both models give density oscillations due to water layering. Right: An example of the local density profiles shows the clear layering effect of the water near either surface. The effect becomes less pronounced in the middle, far from either wall. In this regime, the different bulk behaviors of the two water models begin to appear, and we see different structures for dipoles and SPC.

dipolar model, to demonstrate that these semi-atomistic models capture important physical effects that implicit water models cannot. The most clear effect is layering of the water in confinement, for both dipolar and SPC/E water models, and this leads to large oscillations of the water density as a function of surface separation (Fig. 3.2). This sort of layering has been seen in simulations for a wide range of systems, including atomistic simulations of C-S-H [38, 48, 89, 90]. The layering has also been associated with an oscillatory solvation force measured between surfaces at very small separations [67].

In addition to layering, we see a clear restructuring of the water into hydration shells around the Calcium ions. The ions themselves stay close to the charged surfaces, and the water forms hedgehog like structures around the ions. All this limits the orientational mobility of the water, resulting in a decreased effective dielectric constant in confinement (Fig. 3.3). A similar effect was seen in simulations of cylindrical pores when surface

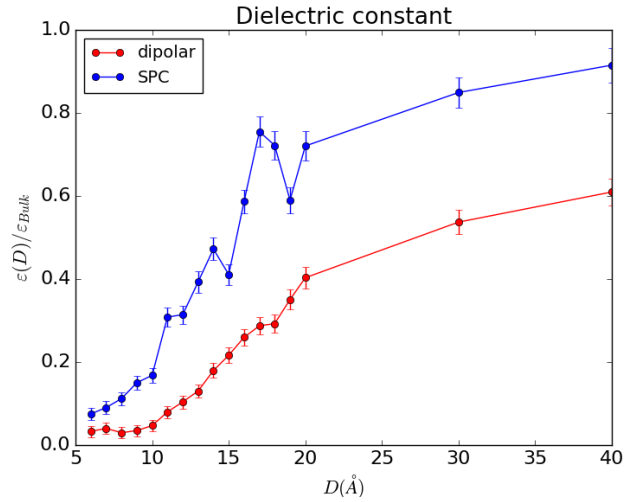


Figure 3.3: The effective dielectric constant of the confined water. There is a clear reduction in dielectric properties due to water restructuring under confinement and around ions.

charged density was increased [114]. There is also experimental evidence that the water restructuring near an AFM tip (tested by modifying tip material) reduces the dielectric constant of water [140].

These results demonstrate that there are important physical effects that implicit water models miss which my simulations with semi-atomistic models are able to capture. We know from Carrier’s PhD thesis work [24] that the change in solvent properties can strongly affect the net forces in clays. The next questions are what effect they have for C-S-H and by which microscopic mechanisms the solvent affects the cohesion in the developing material during cement hydration.

3.6 SUMMARY

In this chapter I have discussed the model and simulation approach I have developed to analyze how nanoscale forces between C-S-H particles emerge during hydration. I have

built on previous work carried out for clays and formulated a semi-atomistic approach that allows for an explicit description of confined water in the presence of divalent ions. In the next chapter, I will discuss the novel insight obtained, through this approach, into how nanoscale cohesion develops during cement hydration

CHAPTER 4

THE NANOSCALE ORIGIN OF CEMENT COHESION

Cohesive forces between charged C-S-H nanoparticles are the foundation of cement-based construction. Net attractive interactions between equally charged surfaces in ionic solutions are a widespread phenomenon in colloidal materials or biological systems [24, 66, 67, 70, 95, 116, 134]. As discussed in Ch. 1, primitive model (PM) simulations have shown that net attractive interactions can emerge from correlations of the ions positions in a dielectric continuum that has the properties of bulk water [36, 73, 101, 102, 105]. The corresponding cohesive strength is nevertheless always orders of magnitude too low when compared with experimental measurements of the modulus of the hardened paste [93, 148] and atomistic simulations of hardened C-S-H [89].

In the previous chapter, I discussed how the PM and analytical treatments of this electrostatics problem do not adequately account for the effects of the solvent. Water properties in confinement are drastically different compared to the pure bulk liquid, and the semi-atomistic model we developed can capture those differences. In this chapter, I use that model to investigate the origin of the cohesion of cement hydrates and how such cohesion could arise during hydration. I then analyze the spatial and dynamic correlations to unravel the microscopic mechanisms behind that cohesion. Finally, I discuss the comparison with an analytical theory for strongly coupled systems.

4.1 SIMULATION METHODS AND PARAMETERS

In order to investigate the origin of electrostatic cohesion between C-S-H nanoparticles, I will be using the semi-atomistic model described in detail in Ch. 3. In this model, SPC/E water [11] and Calcium ions (LJ spheres with point charge) are confined by uniformly charged planar surfaces. Fixing the surface separation D and the ion number $N_{Ca} = 64$, the number of water molecules is determined by a Grand Canonical Monte Carlo (GCMC) process to equilibrate the confined simulation volume with a reservoir of water at room temperature and pressure. The GCMC is run until the water density stops changing and its equilibrium value is reached. The GCMC process alone is very slow to converge to the final density as it only considers single molecule moves. To speed up the convergence, we combine this with Molecular Dynamics (MD), with 1000 GCMC exchanges attempted every 1000 MD steps with a time step of 1 fs. With this process, the equilibrium density in confinement is found within $3 * 10^6$ MD steps. In certain larger simulations, the convergence was slow due to the larger number of water molecules. In this situation, an initial configuration with water molecules at bulk density ($\rho = 1\text{g/cm}^3$) significantly reduced the GCMC simulation time required to converge to the equilibrium density.

After this process, MD in an NVT ensemble, with N fixed by the GCMC equilibration and $T = 298\text{K}$, is performed to sample the equilibrium states and measure microscopic variables. Surface separation is varied to measure the pressure and microscopic quantities as a function of D . For each value of D , an independent simulation is performed, including both the GCMC equilibration and MD sampling. As seen in Fig. 3.2, the water density is highly dependent on D , so the entire process must be repeated for each simulation.

From the particle trajectories, the pressure and microscopic correlations can be computed. The pressure is calculated as the time average of the total force exerted on one of the C-S-H surfaces, which fluctuates around a mean value in equilibrium. To investigate

the microscopic origins of this force, we also study the spatial and dynamical correlations that arise in the ions and water. As discussed in Ch. 1, there are theoretical predictions that ions have strongly correlated positions and may even form 2D crystals [119]. To quantify the extent to which this holds, we calculate the pair correlation function $g(r)$ of ions in the xy plane, i.e. parallel to the C-S-H surfaces, defined as:

$$g(r) = \frac{L_x L_y}{2\pi r \Delta r N_{\text{ion}}^2} \left\langle \sum_i \sum_{j \neq i} \mathcal{H}(\Delta r - |r - r_{ij}|) \right\rangle \quad (4.1)$$

where $L_x = L_y$ are the simulation dimensions, r_{ij} is the distance between the two ions in the xy plane, Δr is a binning distance, and \mathcal{H} is the Heavyside function. Later, this function is also calculated for specific groups of ions, determined by their z position, which simply involves modifying N_{ion} and the \sum bounds appropriately.

In addition to static spatial correlations, significant *dynamical* correlations also arise. They have been studied by computing the self-intermediate scattering function [57], which quantifies the time correlations of ion (or water molecule) displacements. In particular, we analyzed the dynamics in the direction normal to the surface, z :

$$F_s(q_z, t) = \frac{1}{N} \left\langle \sum_{j=1}^N e^{iq_z(z_j(t) - z_j(0))} \right\rangle \quad (4.2)$$

where the q_z values are chosen according to the system dimension D . The q_z value sets the length scale of displacements that contribute most to $F_s(q_z, t)$, and due to boundary conditions the lowest allowable value is $q_z = 2\pi/D$. We consider values up to $q_z = 10 \text{ \AA}^{-1}$, corresponding to sub-angstrom length scales. Once again, it can be helpful (and straightforward in simulation) to separate this into contributions from different groups of ions or water molecules, and this requires modifying the N and the bounds of the \sum .

All these simulations and calculations are performed to investigate the microscopic mechanisms responsible for cohesion. One of main goals is to explain the discrepancy between the PM [105] and atomistic simulations [89] or experimental measurements [93,

148] for the cohesion of hardened C-S-H. However, we are also interested in the time evolution of that cohesion. Experimental measurements [107] show that the changing cement chemistry affects the forces between C-S-H surfaces, and my mesoscale simulations in Ch. 2 have demonstrated how that change affects the development of the C-S-H gel. Simulations show that the pH of the cement solution, which rises during hydration, strongly affects the C-S-H surface charge density [77]. In order to explain the emergence of the cohesion starting from the early stages of hydration, we investigated the pressure and the microscopic correlations for a range of surface charge densities, from $\sigma = 1 e/\text{nm}^2$ to $\sigma = 3 e/\text{nm}^2$. $\sigma = 1 e/\text{nm}^2$ is comparable to surface charge densities typical of clays, and in general, low surface charges could be due to the partial development of the structure typical of the hardened paste. For each set of simulations, $N_{\text{ion}} = 64$ was fixed and the simulation bounds L_x and L_y were adjusted accordingly.

4.2 DEVIATION FROM PRIMITIVE MODEL

At lower σ , which corresponds to early cement hydration times, the electrostatic coupling is relatively weak, and one might expect the PM or DLVO pictures to work reasonably well. However, earlier work with clays has already indicated this is not necessarily true, as explicit solvent models can predict attraction where the implicit water PM fails to [24]. Indeed, I find that at $\sigma = 1 e^-/\text{nm}^2$, a surface charge comparable to clays, the inclusion of explicit water leads to a net attraction (Fig. 4.1a) that is not reproducible in the PM. This effect arises from strong and long-ranged correlations in ion positions that are not present in the PM. Like in the PM, the ions are strongly localized in the z direction due to the confinement, but the spatial arrangement in the xy plane is significantly altered. Fig. 4.1b is a plot of the ion pair correlation $g(r)$ (Eq. 4.1). The $g(r)$ shows clear peaks that persist to large distances with SPC/E water. On the other hand, the bare ion PM has no clear peaks,

indicating that their spatial arrangement is close to uncorrelated. A simplistic attempt to account for the hydration shells of ions by considering a larger effective ion size does change the microscopic behavior a bit, reproducing the first $g(r)$ peak, but is insufficient to fully capture the long-range effects of water.

Under confinement, the ion hydration shells differ significantly from those of free ions. At relatively larger separations of $D > 20\text{\AA}$, hydration shells are limited to at most 8 water molecules (Fig. 4.1c), consistent with the average 7.9 calculated for Calcium ions in bulk SPC/E water [76]. As D is decreased, these shells do not immediately change, indicating that a larger fraction of the total water is bound in the hydration shells, with presumably limited mobility and ability to function as a dielectric. Further confinement affects the hydration shells—by $D = 8\text{\AA}$ the surfaces are squeezing the ions into a single layer and pressing against their hydration shells (see simulation snapshots in Fig. 4.1d). Hence reducing D from 9\AA to 7\AA requires overcoming a repulsive barrier that results in a non-monotonic dependence of the pressure on surface separation D . This feature of a repulsive shoulder in the interactions at early times is indeed consistent with the AFM experiments [107] discussed in Ch. 1. In addition, the simulations discussed in Ch. 2 predict that it plays an important role in the early stage of hydration. There have been many hypotheses as to what may produce this repulsion, and my results suggest a novel mechanism as the source. Note that here I considered only one type of ion, but with the addition of salts these hydrated structures could change and this mechanism would lead to repulsion at different D .

4.3 INCREASING SURFACE CHARGE

As σ is increased in the simulations, the ions become increasingly localized in the z direction. At $\sigma = 3e^-/\text{nm}^2$, ions become strongly confined to layers near the walls and progressively squeezed with their hydration shells against the walls (as seen from ion density

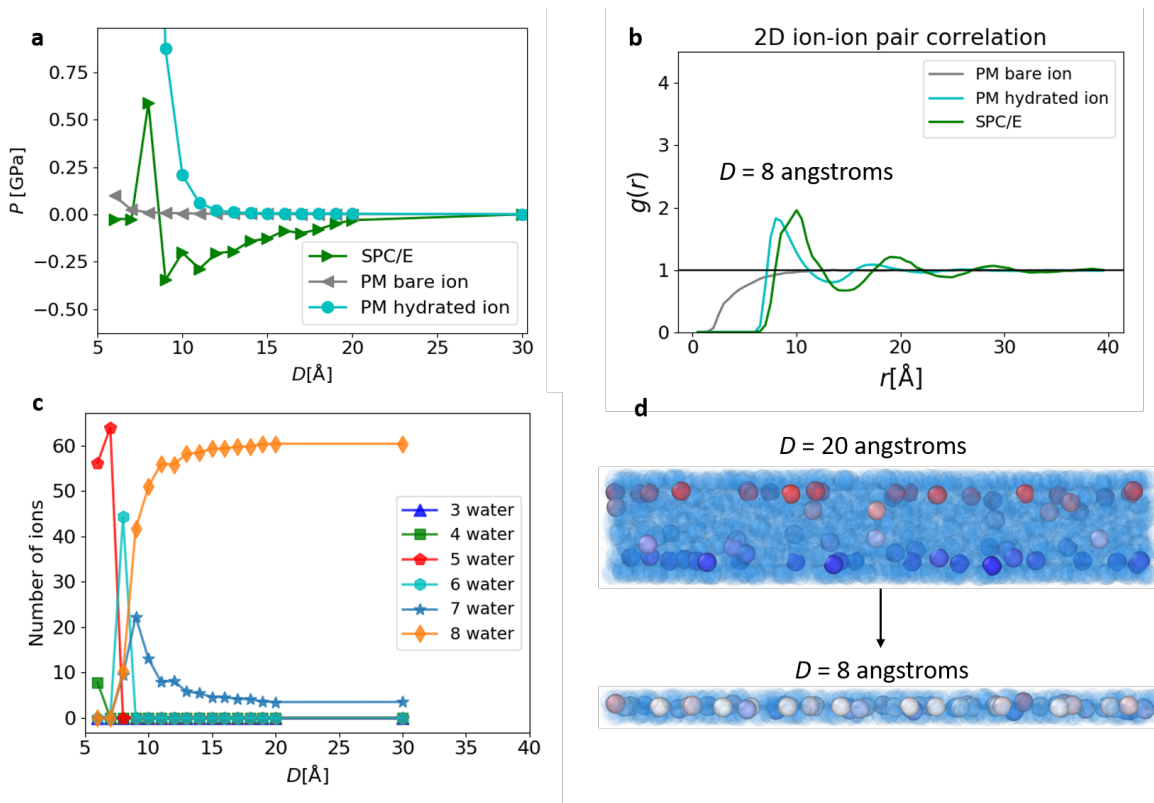


Figure 4.1: Semi-atomistic approach deviates from PM even at low σ . In (a) we show the net pressure between the C-S-H surfaces. With explicit water, we obtain negative pressures—i.e. net attraction—that cannot be found with the PM approach, even considering an increased effective ion size due to hydration. This stems from much strong ion-ion correlations seen in (b), where we plot the pair correlation in the xy plane at $D = 8$ Å. Using the hydrated ion size in the PM creates a first peak that is similar to what we get with explicit water, but it cannot replicate the long-ranged correlations. The water behavior is more complex than that and strongly depends on confinement. Looking at the hydration shell size (c) we see that, at large separations, we observe nearly full hydration shells of 7-8 water molecules. As D is decreased, these shells make up a larger portion of the system water, which affects its ability to screen electrostatic interactions. When confined to $D = 8$ Å, the ions coalesce into a single layer (d) and these shells get pressed by walls resulting in the overall repulsion seen at this separation.

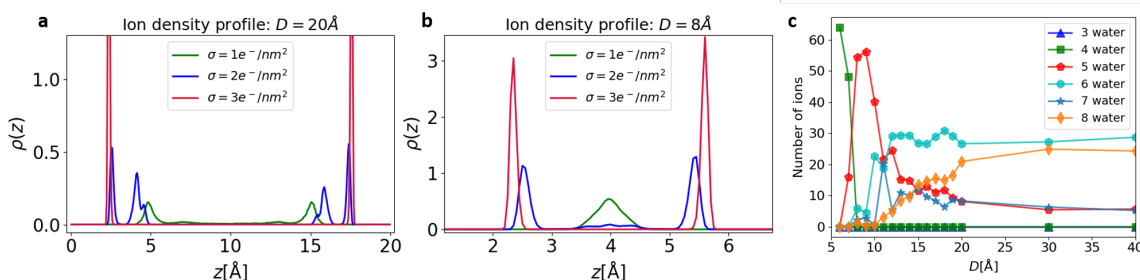


Figure 4.2: Ion density profiles and hydration shells. Plots of ion density profiles at (a) $D = 20 \text{ \AA}$ and (b) $D = 8 \text{ \AA}$. By increasing surface charge density, we see an increasing localization of ions in the z direction. For $\sigma = 2e^-/\text{nm}^2$ at large D (c), there is a split between wall ions with a hemispherical hydration shell of 5-6 water molecules and shifted ions with a nearly full hydration shell of 7-8 water molecules. At lower D or higher σ , the shifted ions are suppressed and all ions are close to the wall, in stark contrast to the situation at $\sigma = 1e^-/\text{nm}^2$ and $D = 8 \text{ \AA}$ where all the ions coalesce into a single layer.

profiles in Fig. 4.2a,b). Because of that, they are unable to form full hydration shells. At $\sigma = 2e^-/\text{nm}^2$ and $D = 20 \text{ \AA}$, the ion profiles show that there are two peaks, split between these wall ions with a hemispherical hydration shell of 5-6 water molecules and shifted ions with a nearly full hydration shell of 7-8 water molecules (Fig. 4.2c shows the hydration shell populations in simulations with $\sigma = 2e^-/\text{nm}^2$). If D is decreased at $\sigma = 2e^-/\text{nm}^2$, the shifted ions are eliminated and there is no splitting of the ion density peaks at $D = 8 \text{ \AA}$, indicating that this localization is a function of both separation D and surface charge σ . Finally, for the highest surface charge $\sigma = 3e^-/\text{nm}^2$, the ions stay pressed against the walls even at large separations.

To better understand the implications of these different types of ion layers/hydration shells, we go back to the pair correlation, plotted in Fig. 4.3. This shows the $g(r)$ separated into intra- and inter-layer correlations at high confinement ($D = 8 \text{ \AA}$). The layers are defined by the ion position z_i , and the calculation considers either ions in the same layer (intra-layer)

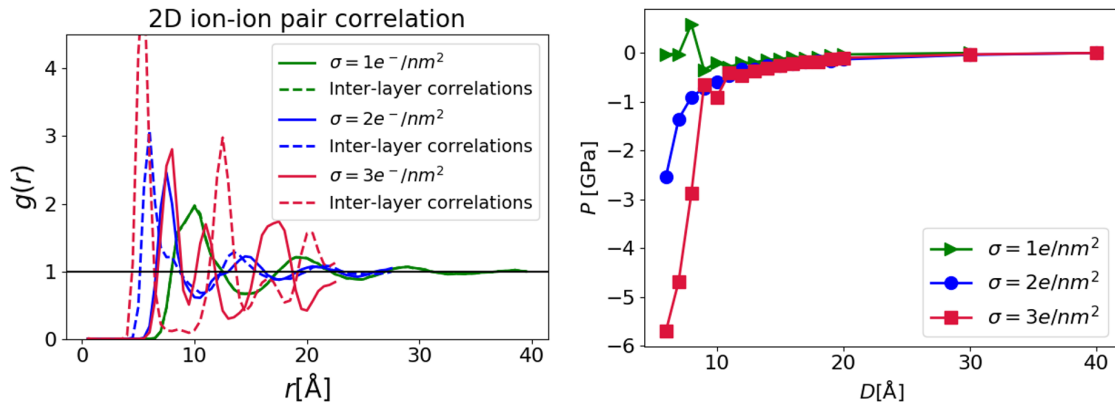


Figure 4.3: Rising correlations and cohesion with increasing σ . The xy pair correlation $g(r)$ between ions shows that, as σ increases at fixed separation $D = 8\text{\AA}$, ions become closer together and their positions more correlated. The increasing correlations drive the overall pressure between the confining walls to become increasingly attractive, reaching $P_{\min} \approx 6\text{GPa}$ at $\sigma = 3e^-/\text{nm}^2$.

or opposite layers (inter-layer). At $\sigma = 1e^-/\text{nm}^2$ where the ions are in a single layer, this separation is meaningless. However, as σ increases, we see a clear signal that the layers have distinct but strongly coupled ordering. Despite the separation in z , the xy positions remain correlated and we observe a staggered square lattice—which is in fact the ground state configuration for confined charges in the strong coupling regime [119], as discussed in Ch. 1. Another key observation is that the correlation strength rises significantly with σ , and this is coupled to a large increase in the net attractive pressure between the two C-S-H surfaces. In fact, at $\sigma = 3e^-/\text{nm}^2$ we get a pressure minimum of $P_{\min} \approx 6\text{GPa}$, which is consistent with atomistic simulations and nano-indentation experiments for fully hydrated cement [89, 93, 148].

4.4 DYNAMIC CORRELATIONS

In addition to the strong static spatial correlations measured by the $g(r)$ (Fig. 4.3), the ion-water correlations have significant implications for the dynamics of the system. This has been quantitatively measured by computing the self intermediate scattering functions (Eq. 4.2), which give insight into the time dependence of spatial correlations. By varying q , we determine how the correlations depend on the length scale $2\pi/q$.

At lower surface charges, the ions become highly localized in the z direction, leading to a plateau in $F_s(q_z, t)$ (see Fig. 4.4a). The plateau value depends on q_z , indicating that the ion positions fluctuate a small amount, and are thus uncorrelated at high q_z , but do not change significantly during the simulation time. Due to the formation of hydration shells, this localization extends to the water as well, and we observe long t plateaus in $F_s(q_z, t)$ (Fig. 4.4b). There are, however, specific values of q_z which allow enhanced decay in $F_s(q_z, t)$, such as the violet curve corresponding to $q_z = 2\pi/5\text{\AA}^{-1}$. The enhanced mobility at specific length scales corresponds to the ability of water in hydration shells to exchange with free water or attach to a different ion. As only these specific types of motion are allowed, certain characteristic length scales, associated with these moves, emerge in $F_s(q_z, t)$. As separation increases, and water and ions become progressively less confined, we investigate the water dynamics for both free and bound water and observe a relatively slower decay in $F_s(q_z, t)$ for water that is bound in hydration shells at time $t = 0$ (plotted in Fig. 4.4 c and d). However, while energetically favorable, Calcium hydration shells are highly dynamic with residence times $t_{res} \simeq 7 * 10^5 \text{fs}$ [76], and we observe significant decay in $F_s(q_z, t)$, even for bound water, indicating that the water does not stay closely attached to the ions, which are instead highly localized (while Fig. 4.4a is for ions at $D = 10\text{\AA}$, it is qualitatively similar to $D = 40\text{\AA}$).

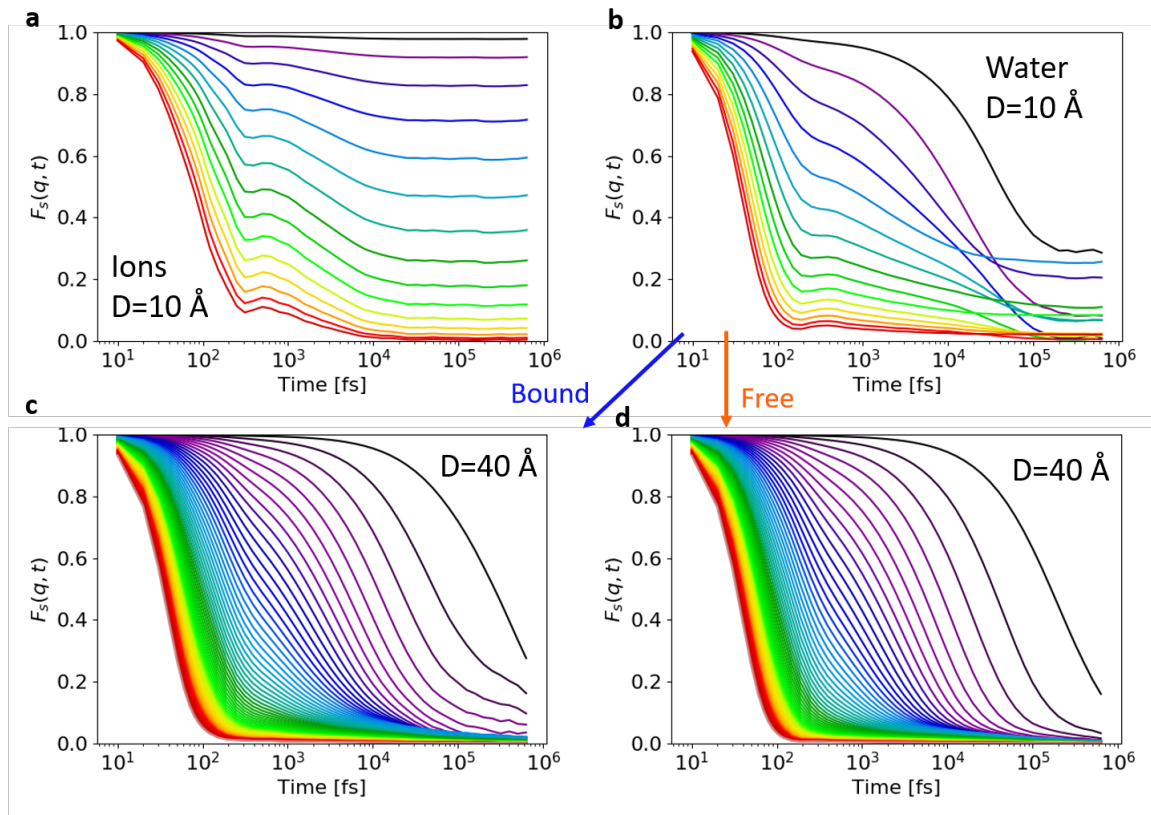


Figure 4.4: Ion and water dynamics at low σ . Self intermediate scattering function at $\sigma = 1e^-/\text{nm}^2$ in the z direction (normal to surface plane) for ions (a) and water (b) at $D = 10 \text{ \AA}$ and bound (c) and free (d) water at $D = 40 \text{ \AA}$. Color indicates q from $q = 2\pi/D$ for black to $q = 10 \text{ \AA}^{-1}$ for red. Ions are highly localized, and at low separations this strongly influences the water dynamics. At large separations, bound water, defined as the water in ion hydration shells at time $t = 0$, is dynamic and free to move on simulation time scales, as indicated by $F_s(q_z, t)$ approaching 0. Nonetheless, compared to free water, the mobility is reduced and the decay in $F_s(q_z, t)$ is slower, demonstrating that the ion-water interactions still reduce water mobility.

Previously, we saw that increasing the surface charge density enhanced the spatial ordering of the ions (seen in Fig. 4.3). Similarly, enhanced electrostatic forces affect the dynamics of the hydration shells of the ions. To better understand this, we calculate the bond correlation, defined as the fraction of ion-water bonds that persist at time t :

$$B_{\text{corr}} \equiv \frac{1}{N_{\text{bond}}} \sum_i^{N_{\text{bond}}} \frac{f_i^{\text{bond}}(t)}{f_i^{\text{bond}}(0)} \quad (4.3)$$

where $f_i^{\text{bond}}(t)$ is either 1 or 0 depending on whether an ion-water pair is bonded or not at time t . B_{corr} decays from 1 at $t = 0$ over time, but does not reach 0 in the simulation time considered. Nonetheless, there is a drastic difference in the decay as a function of surface charge (plotted for $D = 20\text{\AA}$ in Fig. 4.5). As surface charge density increases, we observe that water resides in the ion hydration shells for increasing times. Notably, as the ion charge is unchanged, this difference arises from the collective dynamics of ions and water due to the decreased average distance between ions. The increased persistence times of the hydration shells in turn affect the dynamics of both ions and water.

In the most extreme case of $\sigma = 3e^-/\text{nm}^2$, which would correspond to the end of hydration, $F_s(q_z, t)$ for the ions (plotted in Fig. 4.6a) shows that there is a first decay in the correlation function at short times. This corresponds to a ballistic regime for very short times and distances, with approximately free motion of ions. After this short transient, $F_s(q_z, t)$ shows some oscillations and a flat profile until the end of the simulations, indicating a strong localization. As this effect persists at $q = 10\text{\AA}^{-1}$, this localization holds for length scales smaller than an angstrom, and we infer that this signal corresponds to the localization of the ions near the surfaces, consistent with the density profiles averaged over time shown in Fig. 4.2. Compared to lower σ , the density peaks are sharper and the plateau values of $F_s(q_z, t)$ higher at $\sigma = 3e^-/\text{nm}^2$, demonstrating the increased localization. The plot shown is for a separation of $D = 10\text{\AA}$, but $F_s(q_z, t)$ for the ions is very similar up to $D = 40\text{\AA}$ —the highest separation simulated.

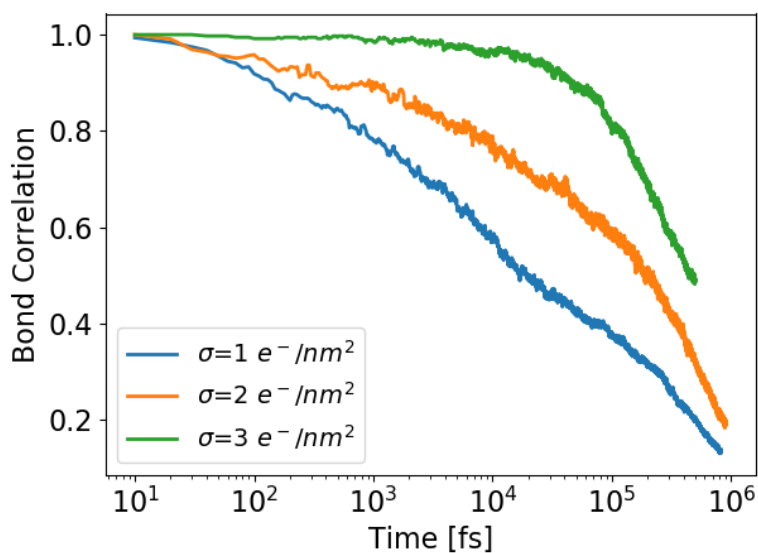


Figure 4.5: Ion-water bond correlation. The bond correlation (defined in Eq. 4.3) for different values of σ at $D = 20\text{\AA}$. The increasing surface charge density makes ion hydration shells more persistent and long-lived. Notably, this change is due to the collective dynamics of ion and water as the individual pairwise interactions between ion and water molecule do not change.

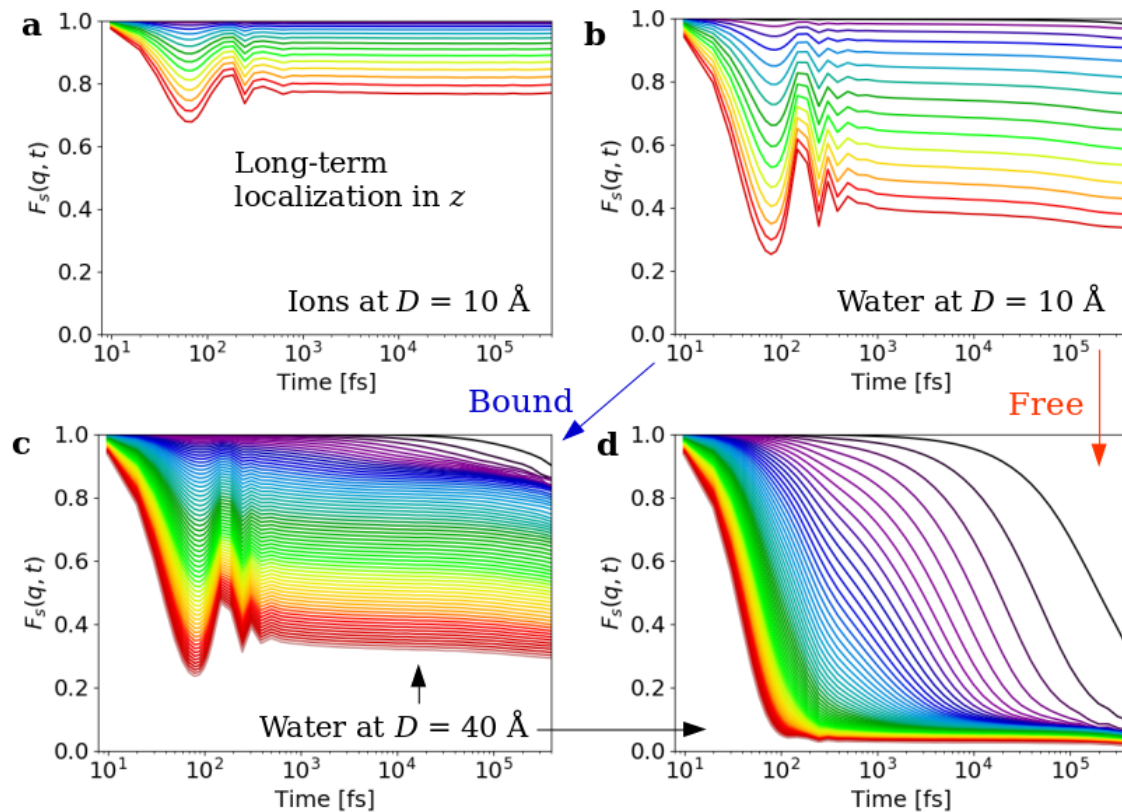


Figure 4.6: Ion and water dynamics at high σ . Self intermediate scattering function in the z direction (normal to surface plane), for ions or water. Color indicates q from $q = 2\pi/D$ for black to $q = 10\text{\AA}^{-1}$ for red. (a) Ions in confinement exhibit strong localization near the surfaces. Notably, this does not change when considering larger separations. (b) Same quantity for water. Its dynamics are highly coupled to ion dynamics in confinement. At larger separations, water is split into two populations. The bound water (c) which starts close to ions follows the ion dynamics, while free water (d) is much more mobile. The dynamical signature of the ions appearing in this bound water demonstrates the stability of ion-water structure and its persistence at larger separations.

Starting at low separation (Fig. 4.6b), we see that the water behavior closely follows the ion dynamics. The correlations drops off to a lower valued plateau, meaning the localization is not quite as strong as for the ions, but it is clearly there for the water as well. The oscillations in Fig. 4.6b also mirror those exhibited by the ions, showing how strongly the water dynamics are coupled to those of the ions. These strong and long-lasting dynamical correlations are evidence of the formation of strongly correlated ion-water assemblies. While similar structures are observed at lower surface charges, the residence time of water molecules the hydration shells is much lower, and thus the water correlations are not as long-lived. Instead, at high σ , the ion-water assemblies persist through the simulation time and the bound water remains highly localized even for $t > 10^5$ fs.

The same picture persists even at larger separations (Fig. 4.6c). However, while at lower separations most of the water is bound to ions, at $D = 40 \text{ \AA}$ we observe drastically different behavior for bound and free water. The bound water, i.e. the water in the ion hydration shells, behaves exactly the same at $D = 40 \text{ \AA}$ as at $D = 10 \text{ \AA}$. This water is strongly coupled to the ions and they move (or rather do not move) in unison. Instead, the dynamics of free water (Fig. 4.6d) is substantially uncorrelated from the ions. There is an initial decay of $F_s(q_z, t)$ for high q_z (short distances), while for a given diffusion speed, it takes longer for the displacement of water molecules to become uncorrelated over large distances (low q_z). The fact that there is no localization in the free water, indicates that the behavior of the bound water is truly determined by electrostatic interactions with ions even at large separations, when the effects of the confinement are reduced.

4.5 HYDRATED IONS VS n -MERS

At higher surface charges, unlike in a bulk ionic solution, ions are localized very close to the walls and hydration shells are limited by the confining surfaces. We label these hemispher-

ical ion-water objects n -mers (n being the number of water molecules surrounding an ion). The simulation snapshots in Fig. 4.7a show the presence of these n -mers and how the water arrangement in these structures depends on the level of confinement. For $\sigma = 3e^-/\text{nm}^2$ beyond $D \simeq 15 \text{ \AA}$, we reach a balance of 5-mers and 6-mers, whereas at even smaller D , the surface limits both the number of water molecules and the space available around the ions, leading to a prevalence of 3-mers or 4-mers as at the smallest separations $D = 6 \text{ \AA}$ (Fig. 4.7b), consistent with fully atomistic simulations of the hardened paste [106]. While the specific size of the n -mers depend on the level of confinement, the presence of these structures is a consistent feature for all separations considered, and their lifetime is longer than the simulation time (demonstrated by dynamic correlations in Fig. 4.6), implying that there should be a strong free energy gain driving their formation.

To ground this microscopic understanding in a theoretical background, our collaborators Ivan Palaia and his advisor Emmanuel Trizac computed the free energy of the n -mers [51, 99]. For these calculations they used a dipolar approximation for the water, where water “molecules” consist of a spherical particle endowed with a dipole moment. This removes one degree of freedom per water molecule relative to the SPC/E water, and this simpler model proves sufficient to provide significant insight. Fig. 4.7 summarizes the results obtained.

The calculations of the ground state energy u_n with varying n show that the tendency to form n -mers can be explained by the significant energetic gain when a dipole adsorbs to an ion. With non-interacting dipoles, this gain is $\sim 64 k_B T$ per water molecule (turquoise line in Fig. 4.7c). By including dipole-dipole interactions (blue diamonds) and then interactions with neighboring n -mers (green squares), we observe that the energetic gain decreases with increasing n , but is still more than an order of magnitude higher than $k_B T$ when going to $n = 6$. The minimum energy configurations used in the calculations are sketched in Fig. 4.7c and correspond to the shapes observed in simulations. In the hydration of ions,

the confinement of water molecules and of their dipoles plays an important role, because it decreases entropy. Taking into account these entropic effects, and therefore including finite-temperature in our (so-far) ground-state calculations, one obtains that 5-mers and 6-mers have the same free energy of formation, within a tolerance $\sim k_B T$: this explains the right part of Fig. 4.7b, where these two structures appear in commensurate proportions. Instead, the free energy gained when a water molecule is adsorbed on a 3-mer to form a 4-mer, or on a 4-mer to form a 5-mer, is energy-dominated and amounts to negative several tens of $k_B T$: it is always extremely favorable to adsorb water molecules on ions from the bulk to increase n , at least up to $n = 5$. As a consequence, upon increasing the confinement, i.e. when progressively fewer water molecules are available in the nano-slit, all of them are adsorbed on ions. This observation allows us to predict the expected fraction of adsorbed water (Fig. 4.7d) and the peaks of the n -mers distribution (Fig. 4.7b) for $n = 3, 4$ and 5 by assuming all available water is bound in n -mers of size up to 5 or 6 .

4.6 THE MICROSCOPIC MECHANISM BEHIND COHESION

Putting together all the analysis I have described so far, a coherent picture emerges. At low σ , hydrated ions exhibit strong spatial correlations (Fig. 4.1b) beyond what is predicted by the PM. This leads to a net attraction between the charged surfaces. The stability of the hydrated structures also serve as a barrier against the surfaces approaching each other too closely, which creates a repulsive shoulder in the net pressure at intermediate distances. As σ increases during hydration, the fully, or nearly fully, hydrated ions become less favorable, especially in strong confinement (Fig. 4.2), and ions separate into layers with strongly crystalline ordering (Fig. 4.3) that matches theoretical prediction for the ground state configuration of confined charges [119]. These ions are strongly coupled to the water due to free energy considerations (Fig. 4.7c), leading to a strong modification of ion and water

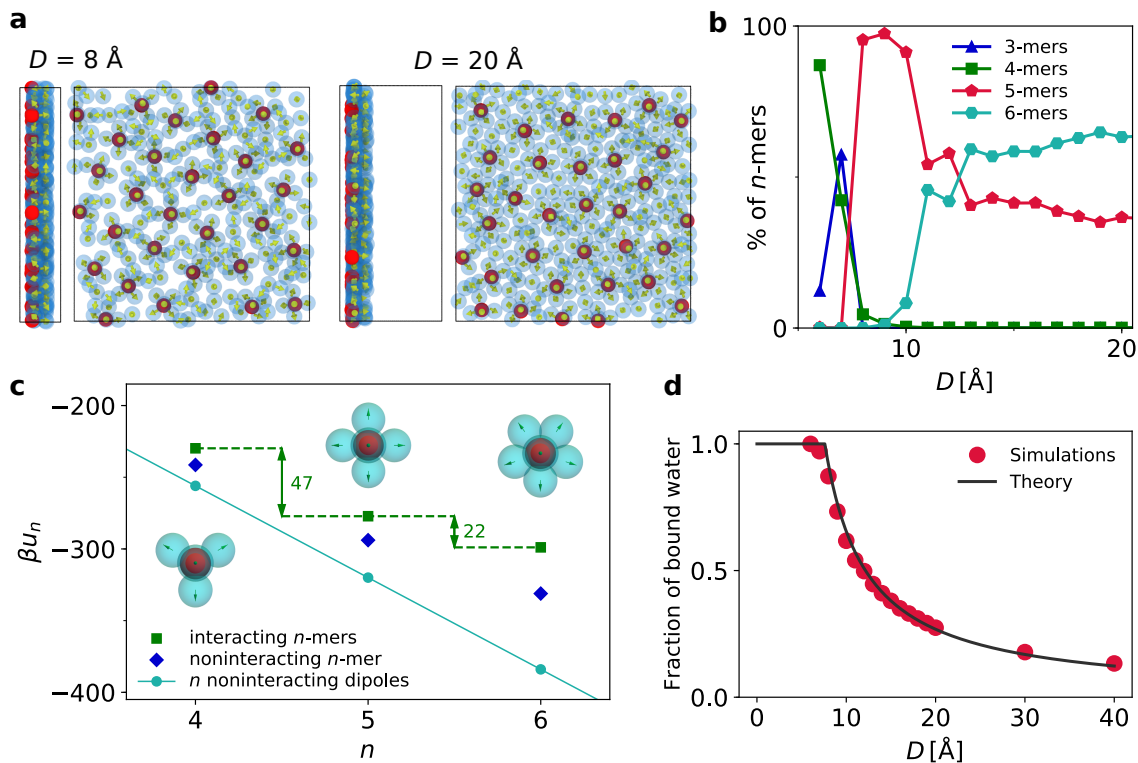


Figure 4.7: Formation of n -mers. (a) Simulation snapshots and ion-water coordination as a function of surface separation. The snapshots show the formation of n -mers with an ion and its n water hydration shell. (b) A transition from 3-mers at low separation to a balance of 5- and 6-mers at larger separations is observed. (c) Ground state energy calculations reveal that there is a large gain for a dipole to adsorb on an ion, explaining the formation of these effective objects. As n grows larger (to 5 or 6), the additional entropic cost becomes sufficient to limit this—with a 6-mer being the largest possible semi-hemispherical object. (d) The fraction of water in n -mers as a function of separation. At small D , almost all water is bound up in these n -mers, with n limited by water availability. At larger separations, the balance of energetic gain and entropic cost limits n -mer size. These theoretical arguments enable quantitative predictions about the water structure which agree with simulations.

dynamics (Fig. 4.6), especially in confinement. As, at small separations, all water becomes bound to ions (Fig. 4.7d), there is a drastic decrease in the ability of water to screen electrostatic forces (Fig. 3.3). This means that, instead of fluctuating ions in a dielectric background (the basis for the PM), we have a highly correlated crystal of n -mers in vacuum. Considering the large dielectric constant of water ($\epsilon \approx 80$), these effects explain the nearly 100-fold increase in cohesive strength that we measure in simulations ($P_{\min} \approx 6\text{GPa}$ with explicit SPC/E water instead of $P_{\min} \approx 60\text{MPa}$ in the PM).

To demonstrate that this mechanism is indeed the origin of the large increase in the force, Palaia and Trizac estimated the pressure through their analytical theory that is based on the idea of “correlation holes” around each ion [120] to account for ion-ion correlations, i.e. by defining a region around each ion in which other ions are prohibited from entering. This idea is supported by the profile of the pair correlation functions $g(r)$ in Fig. 4.3, which exhibits strongly depleted short-scale domains, with $g \simeq 0$. With this concept in mind, Palaia and Trizac computed [51, 99] the local effective field κ felt by an n -mer, due to the presence of all other n -mers, in a staggered arrangement, as the one we obtain for large σ and low D in Fig. 4.3. They obtained ion density profiles that match the profiles obtained in simulations, as shown in Fig. 4.8a, b (here we have used only dipolar interactions for the water to simplify the comparison to the theory, but qualitatively the same behavior is shown in Fig. 4.2a, b with the SPC/E water model). While the theory slightly overestimates the peak heights, the agreement with simulations is excellent.

The interactions between n -mers and walls yield the pressure between the two surfaces. The Coulombic contribution has been estimated as

$$P(D) = 2\pi l_B \sigma^2 k_B T \left[-1 + \kappa(D_{\text{eff}}) \left(\frac{1 + e^{\kappa(D_{\text{eff}}) \frac{D_{\text{eff}}}{\mu_{\text{GC}}}}}{1 - e^{\kappa(D_{\text{eff}}) \frac{D_{\text{eff}}}{\mu_{\text{GC}}}}} \right) \right]. \quad (4.4)$$

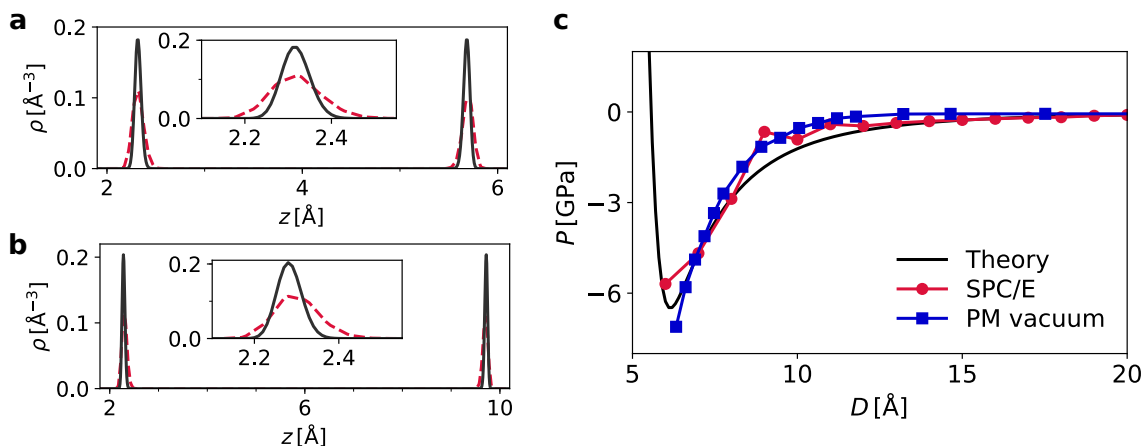


Figure 4.8: A new analytic theory for strongly coupled electrostatics. Ion densities can be computed through the theory of strong coupling and correlation holes, considering an n -mer as an effective ion and treating appropriately the Lennard-Jones interactions between wall and n -mers. These computed density profiles (solid line) are compared to the simulated profiles (dashed line) for (a) $D = 8$ Å and (b) $D = 12$ Å. While the theory predicts a somewhat sharper density peak, there is good agreement between the two. (c) From density profiles, one can compute the equation of state, through a generalized version of the contact theorem. This gives a calculated interaction pressure much stronger than earlier theories for implicit water models and close to what is seen in simulations. Due to adsorption of water into n -mers at small distances, the effective pressure in the explicit water simulations approaches what one would get for ions in vacuum (squares, for which the rise of pressure at distances below 6 Å is not visible, since the Lennard Jones contribution has been discarded for the sake of the argument).

Supplemented with the Lennard Jones contribution (that becomes relevant only for $D < 6 \text{ \AA}$), this prediction yields a total pressure in remarkable agreement with the simulations (Fig. 4.8c). While in our approach water molecules are explicitly accounted for, they are all “captured” by ions. With this major restructuring, their effect on ions is much less important than in bulk conditions, to such an extent that water contribution to dielectric screening can be ignored altogether. This is illustrated in Fig. 4.8c, showing that the results of simulations with SPC/E water and from the theory are close to those of PM simulations with a *vacuum* dielectric constant. For the extreme confinement and highest surface charge considered here, the electrostatic screening ability of water is effectively eliminated. The resultant pressure profile is remarkably consistent with fully atomistic simulations of hardened cement paste [89]. These results reconcile the description of the fundamental physics involved in the electrostatics of C-S-H during cement hydration with the characteristics of the atomistic model proposed by Pellenq et al [106] and with the scenario hypothesized in [49]. We now have the unified picture for the emergence of nanoscale cohesion during cement hydration that was missing.

4.7 THE ROLE OF CEMENT CHEMISTRY

For designing new cementitious materials, understanding the consequences of changing cement chemistry is a necessary step. In addition, there is significant variability in the chemical composition of cement beyond the simple case considered here and in the additives introduced during mixing. Some of this is designed for specific applications or constrained by local resources, and in many cases the implications for the material properties are not understood. The connection between different cement chemistry and its final mechanical properties is unclear but of great practical importance.

The changing of surface charge density in my investigation was motivated by the change in chemical composition of the cement solution as hydration progresses, as changes to pH or the Ca/Si ratio in the mixture can change the C-S-H surface charge. Those results give us an idea of how the chemical changes can affect cohesion and propagate up to larger scale structure and mechanics. However, all of this was done with Calcium ions. Introduction of different ionic species is common and is an important avenue to explore for novel materials. The nanoscale structuring of ions and water into n -mers was found to underlie the cohesion of C-S-H, and thus cement. Modifying the types of ions available would affect that structuring and cohesion. Until now, there has not been an efficient way to make quantitative predictions about how this would change, but the research just discussed provides the framework to do just that. One major consequence of the importance of n -mers is that the ion-water interactions are a large factor in the overall cohesion. In particular, the ion valency controls the strength of the Coulomb attraction between water (with its dipole moment) and the ions. Real cement mixtures contain various components which introduce different ions, and novel materials might not be based on Calcium ions at all.

Over the past year, I have worked with Francis Dragulet, an undergraduate student at Georgetown, on testing the effect of varying ion composition in the scenarios just discussed in the previous sections. Focusing on valency effects, we have studied the cases of Sodium (monovalent) and Aluminum (trivalent) ions in comparison to the Calcium (divalent) case already considered. Following the protocol described in Ch. 3, we have performed simulations for fixed surface charge density $\sigma = 3e^-/nm^2$ while varying the ion type and number (to maintain electroneutrality). Preliminary data already shows that there is a large change in pressure, dynamics, and ion-water structuring upon changing the ion type for high confinement.

Calculations of pressure (Fig. 4.9) indicate that a higher valency results in a stronger attraction at $D = 6\text{\AA}$. As a higher charge produces stronger electrostatic coupling between

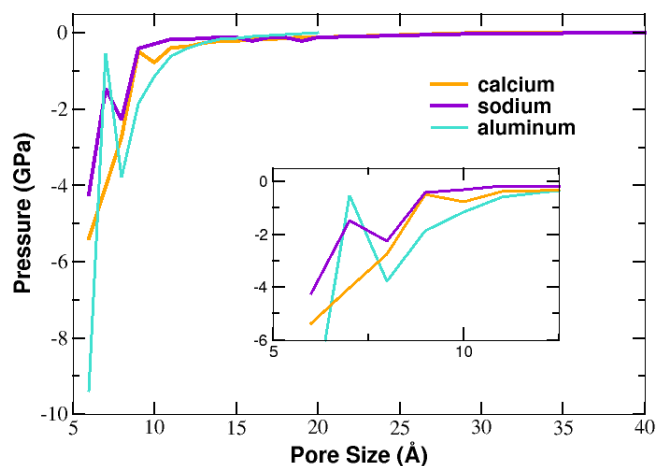


Figure 4.9: C-S-H cohesion strength with different ions. Calculated pressure between surfaces with charge density $\sigma = 3e^-/nm^2$ as a function of the counter-ion type and surface separation. Increasing ion valency leads to stronger attraction at $D = 6\text{\AA}$, but it also changes the entire interaction profile in a non-linear way.

ions and water, this is again consistent with the mechanism based on ion-water restructuring in confinement. Of course, the pressure curves do not tell the full story. Despite the relative similarity of the curves for Sodium and Calcium, the microscopic dynamics are surprisingly different. By computing the Mean Squared Displacement (MSD), we showed that unlike Calcium and Aluminum (which form a solid crystal in strong confinement, $D = 8\text{\AA}$), Sodium ions remain highly mobile (Fig. 4.10). However, they are still strongly localized in planes near the charged surfaces and the MSD normal to the surfaces is flat. Despite the in-plane mobility, correlations in that motion might explain how cohesion may still arise for high surface charges—though further investigation is needed.

Beyond the pressure minimum and MSD, interesting features arise that are not simply explained by the valency. A striking example is the large spike in pressure, to $P \approx -0.5\text{GPa}$,

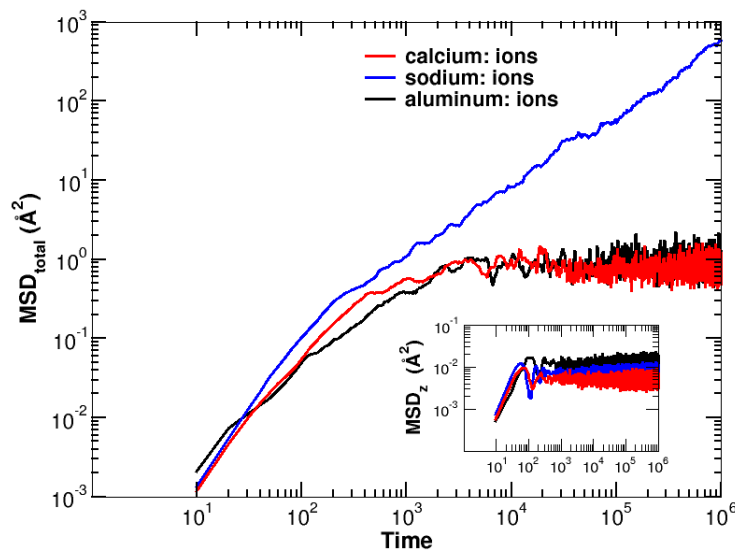


Figure 4.10: Ion dynamics. The Mean Squared Displacement (MSD) of ions in strong confinement, $D = 8\text{\AA}$. While the higher valency ions, Calcium and Aluminum, form a solid crystal, Sodium ions remain diffusive. Inset shows MSD in z direction, normal to surface, in which all ions are strongly confined.

in the Aluminum system at $D = 7\text{\AA}$. Both the curves for Sodium and Calcium show oscillations as well, to a smaller degree, that can partially be explained by water layering and the resulting oscillations in water density, but the local peak at $D = 7\text{\AA}$ for Aluminium is more pronounced than similar oscillations in the curves for Calcium and Sodium. Further investigation revealed that this is associated with a strong energetic preference for certain types of n -mer: much like the spike at $\sigma = 1e^-/\text{nm}^2$, $D = 8\text{\AA}$ with Calcium (Fig. 4.1). Analyzing the Aluminum ion hydration shells shows that 5-mers are the most preferred configuration at almost any D (Fig. 4.11). However, at $D = 7\text{\AA}$, the surfaces impinge on the 5-mers, and at $D = 6\text{\AA}$ there is only enough space for 4-mers to exist. This impingement is exactly the same as what happened for low surface charge Calcium simulations, and the associated energetic cost drives up the pressure.

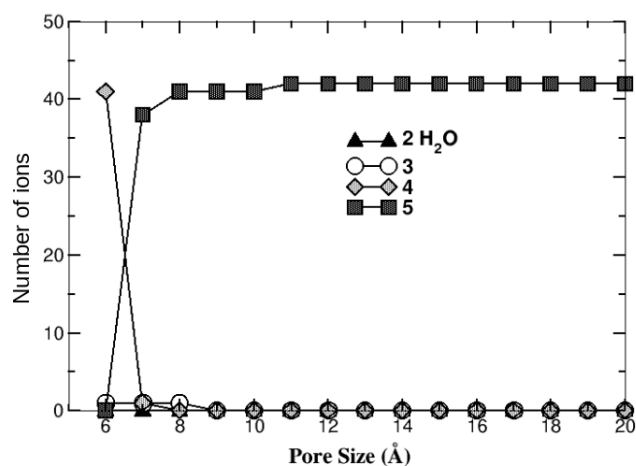


Figure 4.11: Aluminum hydration shells. The size of Aluminum ion hydration shells in simulations as a function of pore size (surface separation D). Due to the high ion charge and small ion size, 5-mers are the most stable configuration at almost all separations. At $D = 7\text{\AA}$, the surfaces impinge on the 5-mers, and at $D = 6\text{\AA}$ there is not enough space for the 5th water molecule in the hydration shell.

These simulations with varying ion composition have demonstrated two main results. First, the role of the ion-water structuring remains central to understanding the emerging pointing to ion specificity, and the cohesion seems to scale with ion valency. Sodium and Aluminum ions specifically are very commonly included in cement mixtures, using materials such as alkali-activated fly ash or slag. These are actively researched avenues for new cements, and it is important to understand these scenarios.

The second result is that varying ions opens up a much richer space of microscopic behavior and macroscopic consequences. Given the large differences in water structure around each type of ion, new types of correlated structures could arise in any real situation with a mixture of ion types. This model provides, for the first time, a computationally

viable procedure to directly investigate the effects of changing cement chemistry on C-S-H cohesion.

4.8 CONCLUSIONS

The semi-atomistic model and the investigations I have discussed in this chapter have elucidated how the cohesive forces that emerge during cement hydration between nanoparticles of cement hydrates are the result of the complex interplay between electrostatics, ion confinement, and water restructuring. The physics discovered here is not restricted to cement: it is applicable to materials ranging from clays to colloids to biological membranes or DNA. I have already discussed that similar models were applied to clay [24], and a theory based on correlations between ions has been proposed as an explanation for DNA condensation [116]. My simulations show the importance of water restructuring in all these effects for cement, but the insight gained here has wide relevance and could be applied directly to the other systems.

The tools I developed allow one to efficiently explore the effects of changing cement chemistry, through its composition or the inclusion of additives. The path to stronger, longer-lasting, and more sustainable cements requires us to explore new formulations, and we now have the ability to make quantitative predictions on the cohesive strength of such alternative materials depending on their physical chemistry.

In the last part of my thesis, I have attempted to bring together all results discussed so far and integrate them quantitatively with new experiments on cement rheology and scattering. To do this, I have been collaborating with Scott Jones and Nicos Martys at NIST. While this effort is still in its initial phase, in the next chapter I will outline the main ideas and preliminary results.

CHAPTER 5

FROM COHESION AND TEXTURE TO RHEOLOGY

In the previous chapter, I have discussed the nanoscale electrostatics responsible for the cohesion of C-S-H particles. Having developed a new physical picture for how nanoscale cohesive forces emerge during cement hydration, the next step is to link the physical chemistry during cement hydration to the microstructural development discussed in Ch. 2. In this chapter, I will discuss ongoing work to connect the microstructure to the rheological properties of the hydrating cement. I describe my collaboration with Scott Jones and Nicos Martys at NIST, who are working to connect the evolution of microstructure and flow properties during hydration with rheology and neutron scattering measurements. Next, I discuss preliminary work on integrating my mesoscale simulations with these efforts, including scattering intensity calculations and simulated shear tests. Finally, I comment on these results in the context of my meso- and nano-scale work, and conclude with the possible implications of this in cement design and use.

5.1 EXPERIMENTAL CHARACTERIZATION OF MICROSTRUCTURE AND RHEOLOGY

The progressive precipitation of C-S-H causes the microstructure and rheology of the cement paste to evolve over time. At NIST, Scott Jones is linking the rheology of setting cement to the microstructure build up by performing simultaneous rheological and Small Angle Neutron Scattering (SANS) measurements. These measurements can provide unique insight into properties of the hydrating paste at early times—a period for which comparatively less data is available, but is crucial, as discussed throughout this thesis, to the final

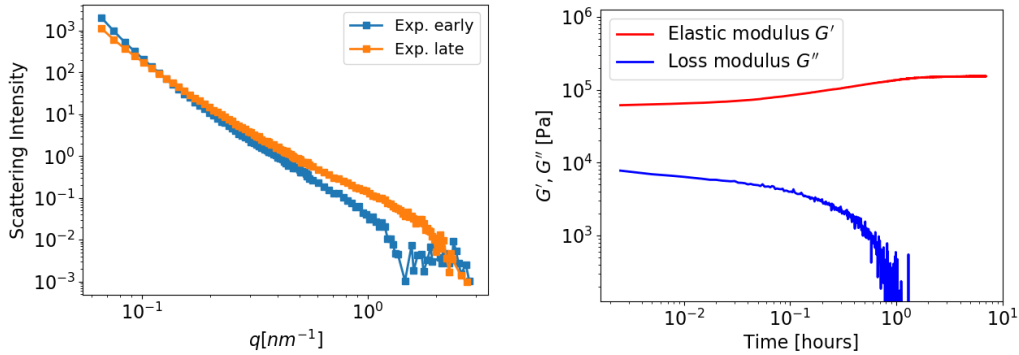


Figure 5.1: Scattering and rheology measurements of hydrating cement paste. SANS and rheology measurements from Scott Jones [71]. Left: Scattering data show that there are microstructural changes in the cement paste during hydration as cement grains dissolve and C-S-H progressively precipitates. $I(q)$ changes from a steeper slope minutes after hydration starts to a less steep one 7 hours later, indicating a greater amount of structure at large q . This is consistent with the newly formed C-S-H nanoparticles creating structure at small length scales. Right: The storage and loss modulus of the hydrating cement paste, calculated from oscillatory shear at $\omega = 6.28\text{rad/s}$, as a function of hydration time. The elastic modulus rapidly increases during hydration as the material becomes stronger, while the loss modulus progressively disappears as the material solidifies.

performance of cement and concrete. Most importantly, these experiments measure the evolution of the properties of hydrating cement.

The history of the material plays an important role in the final properties, but while those final properties have been studied extensively, there is little quantitative information about the early stages of hydration. Nonetheless, the SANS measurements (Fig. 5.1, left) show that there are, in fact, changes in the microstructure in the first hours of hydration, in agreement with previously measured changes in the shear moduli during this time [80] and with previous scattering experiments [3]. Further, these changes are mainly at high q , corresponding to small ($\approx 5 - 10\text{nm}$) length scales, as cement dissolution drives the precipitation of C-S-H nanoparticles. Starting from $I(q) \propto q^{-3.6}$, the scattering intensity

evolves towards $I(q) \propto q^{-3}$ with hydration time, which is the scaling observed in mesoscale simulations and experiments for the hardened paste [65]. This change of slope is consistent with an increasing multiscale heterogeneity of the cement paste as the Porod regime ($I(q) \propto q^{-4}$) corresponding to particle surfaces eventually appears at higher q , or smaller length scales.

The precipitation of C-S-H also drives an increase in the elastic modulus of the paste (Fig. 5.1, right). During the 7 hour interval between the early and late scattering curves, G' —measured via oscillatory shear tests at angular frequency $\omega = 6.28\text{rad/s}$ —triples. Although there are many hours left before the cement hydrates reach their final strength, these measurements indicate that, consistent with the literature [80], there are clearly significant microstructural and mechanical changes happening very early during setting. By integrating my work on modeling the microstructure and nanoscale forces with this approach, I hope to better understand these changes and enable quantitative predictions of the mechanical properties that start from the nanoscale cohesion.

5.2 INTEGRATING NUMERICAL SIMULATIONS

The mesoscale simulations at low volume fractions discussed in Ch. 2 can be used to probe the microstructure development at early stages of hydration. The increase in small length scale structure with time measured by experiments is consistent with the decreasing pore size as calculated in my simulations with increasing C-S-H volume fraction (Fig. 2.9). The precipitation of C-S-H creates a porous network at small scales, filling the larger pores between cement grains and increasing the high q scattering intensity. Depending on the effective interaction between C-S-H nanoparticles, this network (once percolated) could also transmit stresses (Fig. 2.5), which would increase the elastic modulus with hydration time as measured in the shear experiments.

5.2.1 SCATTERING CALCULATIONS

To further this comparison between simulations and experiments, we turn to scattering intensity calculations on my simulated microstructures. I discussed the results of such calculations, based on a method of projecting the microstructure into a 2D plane [20, 44], in Sec. 2.6. In comparing to the above experiments, we are less interested in the anisotropy—which would be averaged out due to the random orientations of scattering surfaces in a macroscopic sample. Thus, we can simply calculate the scattering from the structure factor [57]:

$$S(q) = P(q) \frac{1}{N} \sum_{j,k} e^{-i\vec{q} \cdot (\vec{r}_j - \vec{r}_k)} \quad (5.1)$$

where r is the position of a particle, $P(q) = \left[\frac{3}{qa} \left(\frac{\sin(qa)}{q^2 a^2} - \frac{\cos(qa)}{qa} \right) \right]^2$ is the form factor for spherical particles of radius a , and the sum is over all N particles. The wave vector q has values $n \frac{2\pi}{L}$ where n is an integer and L is the linear size of the simulation box, setting a lower bound for the q values. Fig. 5.2 shows the results for a fixed volume fraction of 25% and using two different interaction potentials corresponding to Early and Late Stages of hydration (ES and LS).

At low q , the finite size of the simulations becomes apparent and we seen an upturn due to the system-spanning density gradient. At $q > 10^{-1} \text{nm}^{-1}$, the two systems exhibit local peaks in the scattering intensity. These peaks correspond to typical cluster sizes, which are larger for the LS potential. The snapshot for the ES system (Fig. 5.2, center) shows the presence of this length scale in the well-defined cluster/branch size, while the LS snapshot (Fig. 5.2, right) reveals a broader distribution and larger pores, consistent with the shifted and broader scattering intensity peak. Unlike the experimental system, there is no contribution to the scattering from the cement grains and other hydration products, so these nanoscale features of the C-S-H structure emerge very clearly in the scattering from the simulation. To the right of the peak, there is a high q decay that is flatter for the LS

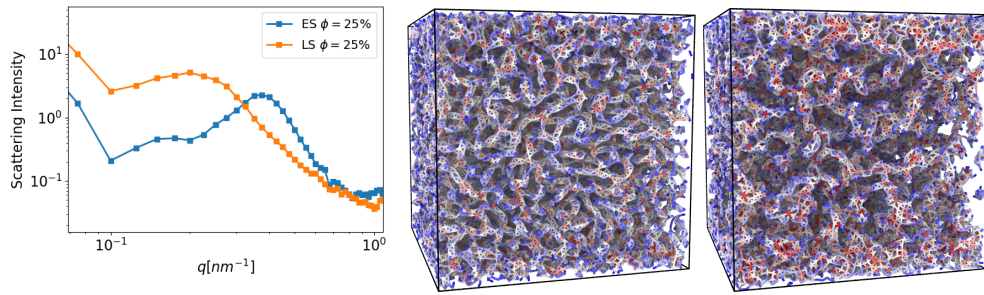


Figure 5.2: Scattering and snapshots from simulations. Left: Scattering intensity computed from my mesoscale simulations for the two different interaction potentials at an overall C-S-H volume fraction of 25%. At small q , the finite size of the simulation box is apparent. At $q > 10^{-1} \text{nm}^{-1}$, there is a local peak associated with the typical clustering of the C-S-H in simulations. To the right of the peak, the high q behavior shows a decay that depends on the potential: with LS exhibiting a flatter slope. Right: Simulation snapshots showing the microstructure for the ES potential (middle) and LS potential (far right), with the color indicating number of neighbors (from blue=0 to red=12). The system-spanning density gradients are responsible for the low q upturn in scattering while the typical cluster/branch size gives the peak—which is more sharply defined for the ES potential.

potential—consistent with the flatter slope at later times in the SANS data. Further work is currently in progress with larger samples and different volume fractions. We also plan to introduce particle size polydispersity which is certainly more appropriate for comparisons with experiments.

5.2.2 SHEAR TESTS

The next step is to investigate the rheological properties of my simulated microstructures. To do this, I run the simulations for hydration as described in Ch. 2. Using the fixed precipitation rate $R = 4$, temperature $T = .15\epsilon$, and a μ gradient along the z direction as described there, I run the simulations to reach a C-S-H volume fraction of $\phi = 25\%$. Stopping the simulations there, I use the microstructure to do shear tests as follows. Keeping the same

interaction potential, I use Langevin dynamics with fixed temperature, $T = .15\varepsilon$, so the equations of motion are:

$$m \frac{d^2 \vec{r}_i}{dt^2} = -\vec{\nabla}_{\vec{r}_i} U - \zeta \frac{d\vec{r}_i}{dt} + \vec{F}_r \quad (5.2)$$

where m is the particle mass, ζ is the damping factor, and $\vec{F}_r \propto \sqrt{\frac{k_B T m}{\zeta dt}}$ is a random force corresponding to the thermal fluctuations of the solvent. The shear is applied via stepwise affine deformations with strain increments $\delta\gamma$, followed by relaxation of the deformed configuration over a period δt , using the method of Colombo and Del Gado [29]. The affine deformation $\Gamma_{\delta\gamma}$ corresponds to simple shear in the xz plane, such that particle positions are transformed according to

$$\vec{r}_i^j = \Gamma_{\delta\gamma} \vec{r}_i = \begin{pmatrix} 1 & 0 & \delta\gamma \\ 0 & 1 & 0 \\ 0 & 0 & 1 \end{pmatrix} \vec{r}_i \quad (5.3)$$

As the simulation box is sheared, the Lees-Edwards boundary conditions [5] are updated to adjust the periodic images according to the applied strain. Next, the system is relaxed for a time δt in the affinely deformed volume according to the equations of motion (Eq. 5.2). The ratio of $\frac{\delta\gamma}{\delta t}$ sets the strain rate $\dot{\gamma}$, and this process is repeated to obtain the desired strain γ .

Applying this protocol to a configuration with the Early Stage (ES) potential at $\phi = 25\%$, I can calculate the shear stress σ_{xz} , using the virial formulation discussed in Ch. 2, as a function of γ and $\dot{\gamma}$ (Fig. 5.3, left). Like in Ch. 2, the unit energy is ε , unit mass m , and unit length (which is equal to the particle diameter) σ . The stress in reduced units is thus ε/σ^3 , while $\dot{\gamma}$ is in units of τ^{-1} . The stress is found to be rate-dependent, even when reducing $\dot{\gamma}$ by two orders of magnitude, suggesting that the microstructure used might not be solid, since its response is not purely elastic even at small strains. In the mesoscale simulations, in

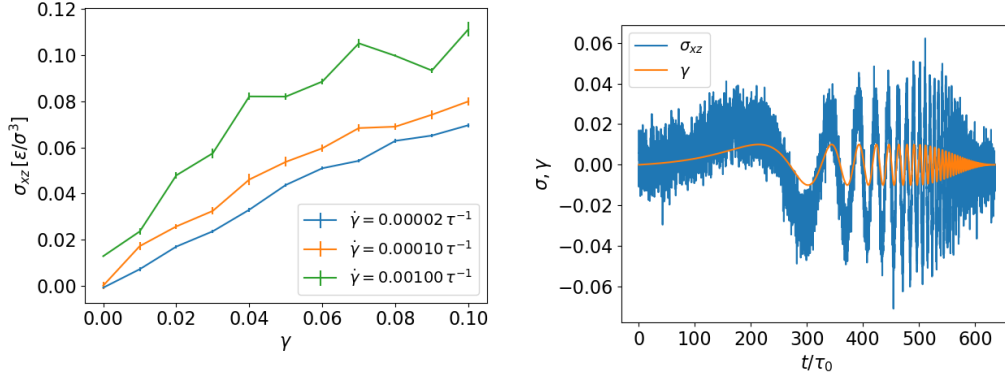


Figure 5.3: Implementing shear in simulations. Left: Start-up shear of simulated microstructure with ES potential at $\phi = 25\%$. The measured stress is found to be rate-dependent, indicating that relaxation of internal stresses occurs during the shear test. Due to the non-equilibrium formation of this microstructure, there are stresses in the system before shear is applied, and thermal fluctuations allow these to relax during shear. Right: Oscillatory shear with the chirp protocol [17] to measure the in and out of phase stress response. At low frequencies, the stress is mostly in phase with the strain, indicating an overall elastic response.

fact, the microstructure is out of equilibrium by design, due to the continuous precipitation of C-S-H, and this leads to the build-up of unrelaxed stresses that do not allow it to reach mechanical equilibrium. In order to mitigate this effect, damped dynamics as applied in [16] can be used to recover a mechanically stable state. This work is still in progress.

5.2.3 SMALL AMPLITUDE OSCILLATORY SHEAR

Small amplitude oscillatory shear allows one to measure the storage (G') and loss (G'') modulus of a sample, by applying a sinusoidally varying strain $\gamma = \gamma_0 \sin(\omega t)$, where γ_0 is the strain amplitude and ω the frequency. The stress exerted by the material as a response to the deformation is used to calculate the moduli. The storage modulus is associated with the in-phase response, while the loss modulus is the out of phase response:

$$G'(\omega) = \text{Re} \left\{ \frac{\tilde{\sigma}(\omega)}{\tilde{\gamma}(\omega)} \right\}; \quad G''(\omega) = \text{Im} \left\{ \frac{\tilde{\sigma}(\omega)}{\tilde{\gamma}(\omega)} \right\} \quad (5.4)$$

where $\tilde{\sigma}$ and $\tilde{\gamma}$ are the Fourier transforms of stress and strain respectively. In my simulations, this is done by solving the equations of motion (Eq. 5.2) with strain applied according to Eq. 5.3 and Lees-Edwards boundary conditions [5] updated accordingly. From the particle positions and forces, one obtains the resulting shear stress as a function of the imposed strain frequency. Traditionally, the procedure is repeated for each frequency ω of interest. A more efficient method has been proposed [17] in which a range of frequencies are sampled simultaneously using a chirp signal. The chirp strain profile has a frequency that varies continuously in a specified range, as shown in the right panel of Fig. 5.3, where I have plotted the applied shear and measured stress from my simulations. As the stress is mainly in phase with the strain, the overall behavior is elastic, and the moduli (as a function of frequency) are plotted in Fig. 5.4.

5.3 INVESTIGATING TIME EVOLUTION

In considering the time evolution of the microstructural and rheological properties during the simulations, as done in Ch. 2, there are two main parameters to account for: the interaction potential and the volume fraction ϕ . In principle, both of these should change with hydration time. In Ch. 2, I discussed simulations with different interaction potentials corresponding to earlier and later hydration times. Using that as a starting point, I have run oscillatory shear tests and measured the moduli from simulations for these two different scenarios (Fig. 5.4). G' and G'' are measured in units of ε/σ^3 , like the stress.

That data show that G' is, for the ES potential, greater than G'' (Fig. 5.4), implying that the material is solid-like. Comparatively, the LS system has weaker elastic response, with G' closer to G'' . These differences between the two potentials are very consistent with the

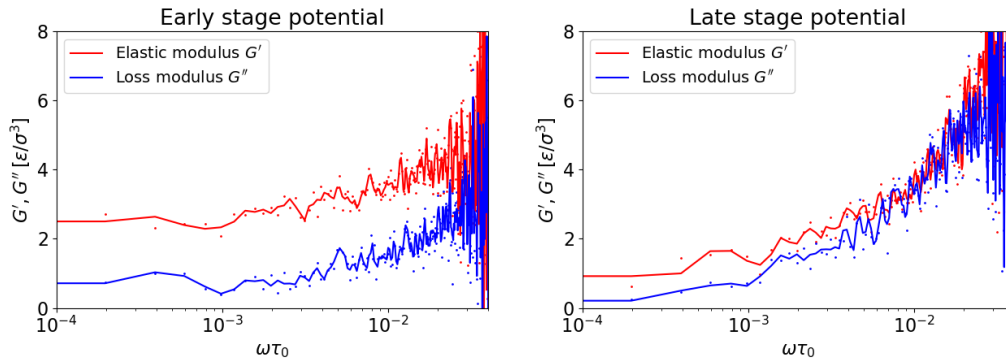


Figure 5.4: The elastic and loss modulus of the C-S-H gels. Dots are calculated data points while the solid line is a smoothed fit to guide the eye. At large frequencies, noise dominates and it is impossible to make meaningful measurements. The calculated G' is much higher for the ES potential, which is consistent with the formation of a percolating network that can transfer stresses as was observed in Ch. 2. The LS configuration instead exhibited larger density gradients, network anisotropy, and pore size: which explains its reduced ability to deform elastically.

observations about their respective microstructures in Ch. 2. For example, I demonstrated that the formation of a percolation structure led to a redistribution of stresses in the ES system. This indicates that the geometric percolation corresponds, in this case, to the formation of a mechanically percolating network—which would behave elastically. On the other hand, the LS system did not exhibit such a change upon geometric percolation. In addition, it showed large density gradients and coarsening pores, which are indeed likely to less solid-like material.

These oscillatory shear tests are consistent with the microstructural analysis of Ch. 2. However, the modulus obtained with the interactions corresponding to later stages (LS) of hydration is not consistent with our understanding of setting cement—which should get harder over time. The problem arises from the fact that, to obtain the microstructure used in these tests, we have used the LS potential from the very start of the simulations. Without

the initial stage where ES interactions drive the mechanical percolation and create a well-connected C-S-H network, the progressive densification brought on by the LS interactions happens in a far too heterogeneous way, leading to a mechanically weaker structure. The material history, *how* the microstructure develops over time, indeed plays an important role in the final properties it exhibits.

A more realistic scenario would therefore involve starting with the ES potential and gradually shifting towards the LS potential as the simulation progresses. Now that we have understood the nanoscale mechanisms controlling these interaction potentials during hydration (Ch. 4), it will be possible to use data on cement pore solution composition [81] to produce a quantitative time line for the evolution of the interactions. By connecting this to the experimental measurements of microstructure and rheology over time (Fig. 5.1), it will then be possible to develop a mesoscale model that incorporates a time-evolving interaction potential.

5.4 SUMMARY AND IMPLICATIONS

In the ongoing collaboration with Scott Jones and Nicos Martys at NIST, we are attempting to integrate simulations and experiments in order to connect the mesoscale texture of the cement paste to its macroscopic rheology during hydration. Simultaneous SANS and shear experiments during hydration (Fig. 5.1) show that the precipitation of C-S-H creates a heterogeneous network that strengthens the paste over time.

These observations are consistent with the microstructural changes observed in my simulations with increasing volume fraction of C-S-H. The progressive precipitation of nanoparticles creates small-scale porosity (Fig. 2.9) and leads to the formation of a percolating network that transmits stresses (Fig. 2.5). To further these comparisons, I calculated

the scattering intensity of my microstructures (Fig. 5.2) and performed shear tests to measure the moduli (Fig. 5.4). These results strengthen the discussion in Ch. 2: the history of the material plays an important role in the final properties.

Now, with the results of Ch. 4, we are in a position to explore the effects of that history more realistically. These results can then be used to motivate the interaction potentials in the mesoscale model to create a realistic time-evolution of the microstructure, and by integrating this approach with experiments we will be able to make quantitative predictions of the mechanical properties. When designing new formulations of cements, the central question is how the changes in cement chemistry will affect the mechanical properties: both during setting (to inform the transportation and construction protocols) and in the hardened material. The current answer is to make the new cement mixture and test it. The nanoscale model and the approach described in Ch. 3 and 4 open the path to explore the effects of changing cement chemistry on the cohesion. This framework would allow us to predict those properties from first principles using the information about cement composition.

The ideas just sketched are particularly interesting for the application of 3D printing with cement. Additive manufacturing (or 3D printing) based construction methods have the potential to revolutionize the industry, open up new possibilities for architectural designs, and increase sustainability. However, current methods of 3D printing cement struggle to produce consistent end products and require deeper knowledge of the evolution of material properties [23]. To progress, a precise control of material properties during pumping and setting must be achieved. During setting, the flowability and buildability of cement change rapidly, leaving a vary narrow window of time in which the material properties are such that 3D printing can be successful [23]. With a framework to model the rheology of the hydrating paste over time from the nanoscale cohesion and mesoscale texture, the work I have laid out in this thesis opens new opportunities for advancing these technologies.

CONCLUSIONS AND OUTLOOK

To design new cementitious materials with reduced carbon footprint or to improve the durability and strength of current cement, a clear understanding of the mechanisms that control cohesion and setting is needed. Additionally, novel applications such as additive manufacturing (3D printing) with cement are not possible without a framework to understand how the mechanical properties of cement develop during setting and what controls that development. The current state of the art with regards to cement design mostly relies on empirical models and experiments, with an incomplete understanding of the underlying physics, which makes researching advancements a slow and arduous process. The central challenge is the multiscale complexity of cement coupled to a non-equilibrium setting process. This is the fundamental problem that this dissertation attempts to address.

The difficulties start at the nanoscale: where charged C-S-H nanoparticles produced through the hydration of cement grains are immersed in a solution containing counterions. Due to the high surface charge density and ion valency, mean field theories fail to predict the cohesion between the nanoparticles. Computational models which allow for ion correlations predict attraction but still leave a multiple order of magnitude gap in attractive strength with experiments and atomistic simulations. Those C-S-H interactions then influence the developing microstructure during hydration. The progressive dissolution of cement grains and precipitation of C-S-H drives the non-equilibrium development of the C-S-H gel. During this process, the effective interactions between the C-S-H nanoparticles

change with the changing chemistry of the solution. Eventually the C-S-H, which precipitates at cement grain surfaces, grows into the pore solution forming a dense, percolating, solid glue that binds together any aggregates and forms concrete.

Building on existing models, I investigated the effects of heterogeneous C-S-H growth and time-evolving interactions on the C-S-H gel morphology. The interactions present early during hydration drive the formation of a percolating cluster that limits stress and density gradients while maintaining porosity to enable continued hydration. As hydration progresses, the heterogeneous growth and altered interactions lead to high densities with strong local variations as seen in hardened cement pastes. In particular, the specific evolution of the interactions during hydration is found to play an important role in determining the final properties.

To address this, I investigated the evolution of those interactions via a semi-atomistic model that incorporates explicit ions, immersed in SPC/E water, and confined by charged planar surfaces. Through simulations over a range of surface charge densities and ion types, I demonstrated the strong spatial and dynamic correlations that arise between ions and water. The formation of coordinated ion-water structures is responsible for reducing the screening capabilities of water and enhancing the attractive strength compared to implicit water models. Additionally, features such as repulsive peaks in the net force between the confining surfaces can arise when the ion-water structures are impinged upon by those surfaces.

These results explain the nanoscale mechanisms which are responsible for the cohesion of C-S-H gels. They also explain how such cohesion can develop over time during hydration as the surface charge density rises and how modifying cement composition would affect the cohesion by introducing different types of ions. Moving forward, this provides a framework to quantitatively predict the nanoparticle interactions for specific cement mixtures. This framework is not limited to cement: construction materials such as clays or geopolymers

and even biological membranes or DNA share many features at the electrostatic level, and the framework developed for cement could be applied to all these scenarios.

The mechanical strength and flow properties of cement depend on the C-S-H microstructure which in turn depends on the nanoscale interactions. Building the models to understand the nano- and meso-scale physics enables us to make quantitative predictions about the effects of time, cement composition, setting conditions, and more on the macroscopic material properties. As part of the endeavor to develop this further, I have begun to study the rheological response of my simulated microstructures. Preliminary tests demonstrate the strong connection between the structural features and the flow properties. By varying the interaction, volume fraction, and other simulation parameters, this can be extended to model the rheology corresponding to different physical conditions.

Longer term, my nanoscale model can be used in conjunction with experimental input on cement solution chemistry to develop a quantitative timeline for the evolution of the C-S-H nanoparticle interactions. This can also be connected to modifications of cement chemistry, through the novel compositions or additives, so we can guide the design of new and improved cementitious materials. Using the computed effective interactions as input, the microstructure and material properties can be investigated via the mesoscale model—enabling quantitative predictions based on first principles. This framework facilitates more efficient and intelligent material design for practical applications, and I hope that this research will help us to make some *concrete* changes in the world.

APPENDIX

DISCONTINUOUS SHEAR THICKENING IN FORCE SPACE

Discontinuous shear thickening (DST), or the abrupt viscosity increase of a suspension at some applied stress, is explained in terms of jamming of the particles through frictional contacts that develop under flow. It is typically associated to strong microscopic fluctuations whose origin is unclear and not easily explained by spatial correlations. During the program on The Physics of Dense Suspensions at the Kavli Institute of Theoretical Physics in Spring 2018, I developed a collaboration with Bulbul Chakraborty and her group at Brandeis University (including Jetin Thomas and Deshpreet Bedi) who have been studying this transition through the force networks emerging under shear. They have created a theory based on this “force space” representation that is built on simulations of dense granular systems by Abhinendra Singh at University of Chicago. By treating the force space vertices as particles with some effective interaction potential, one can develop a statistical physics framework to characterize the force network configurations accessible in flow. I have worked on a new way of generating these effective potentials, sampling the accessible force space configurations with MD simulations, and using a Fourier transform analysis to study the differences between the potentials generated for the systems in and out of DST regimes. Outside of DST, potentials exhibited a secondary minimum: a feature that can lead to more elongated and anisotropic structures. This points to a change in long-range correlations in force space associated with the DST transition [143]. This work is summarized here.

A.1 INTRODUCTION

Dense suspensions of grains in a fluid display an increase in viscosity $\eta = \sigma_{xy}/\dot{\gamma}$ (thickening) as the confining shear stress (σ_{xy}) or strain rate ($\dot{\gamma}$) are increased. At a critical, density dependent shear-rate $\dot{\gamma}$, the viscosity increases abruptly: a phenomenon termed Discontinuous Shear Thickening (DST). In stress-controlled protocols, $\eta \sim \sigma_{xy}$ marks the DST boundary [21, 91]. Experiments have also observed changes in other components of the stress tensor such as the first normal stress difference, $N_1 = \sigma_{xx} - \sigma_{yy}$ close to the DST regime [117]. A mean-field theory [25, 153], based on an increase in the fraction of close interactions becoming frictional (rather than lubricated) with increasing shear stress, has been extremely successful at predicting the flow curves and the DST flow-state diagram in the space of packing fraction, ϕ and shear stress or strain rate [83, 130]. The presence of frictional forces and the nature of the contacts between the grains has been intensively scrutinized and investigated [31, 43, 94]. The physical picture of lubricated layers between grains giving way to frictional contacts when the imposed σ_{xy} exceeds a critical value set by a repulsive force [153] provides a consistent theory of DST [130], shear jamming fronts [56] and instabilities of the shear-thickened state [26, 60].

The link between the constraints that such forces generate at the grain level and the emerging flow properties at the level of the whole suspension, such as normal stress differences [61, 68, 117], points to the existence of long ranged microscopic correlations that have been, so far, elusive to any structural analysis [83]. Conventional measures such as the microscopic pair correlation function of the grain positions, in fact, do not exhibit pronounced changes accompanying DST. As a consequence, although several features relating to the flow of dense suspensions can be well explained within the mean-field theory [25, 153], the nature of the microscopic correlations underlying this transition remains far from clear [83]. A recent theory [142] has proposed that a representation of the shear thick-

ening grains through their force networks, which emerges naturally from the collective force balance constraints under flow, can help better elucidate those correlations. In this “force space”, one can identify a correlation function that exhibits significant changes in its anisotropy across the DST transition. These correlations reflect the collective behavior triggered by changes in the nature of the *contact forces*, which often arise due to small changes in grain positions difficult to detect in any positional correlations. An interesting, distinctive feature of DST is that the shear stress increases less rapidly than the mean normal stress, and hence their ratio, the macroscopic friction coefficient, *decreases* as the fraction of frictional contacts *increases*. This, and direct visualizations [83], indicate that there are important changes in the network of frictional contacts that are not captured by scalar variables such as the fraction of frictional contacts. Remarkably, a statistical theory based on the observed correlations in force space, provides a semiquantitative description of the macroscopic friction coefficient and of the rheological changes accompanying DST [142].

The force-space based statistical theory, however, has only been explored through a mean field approach, while several experiments have indicated that long-range spatial correlations close to DST must be accompanied by large, intermittent stress fluctuations [112, 113, 118]. A theory in force space able to include fluctuations and predict their qualitative change close to DST, beyond mean field approximations, could therefore provide significant new insight into the origin and the nature of the transition. The existing theory [142] is difficult to generalize beyond mean field because the effective potential obtained directly from the correlations in force space is anisotropic and has a very strong clustering tendency, which makes it difficult to use it to sample the corresponding microstates in force space. In this paper, we outline a different procedure to (a) systematically construct a coarse-grained effective potential, which describes the behavior at large scales in force-space, and (b) go beyond the mean field theory using numerical simulations of this effective potential. The idea is that the representation of the shear thickening suspension in force space can be

mapped into a many-body, statistical mechanics description of points (akin to particles) interacting through the coarse-grained effective potential. As a consequence, numerical simulations that solve the corresponding many body equations of motion for the interacting points may naturally provide a beyond-mean-field description in force space. The coarse-grained potential we obtain here is *central* but, remarkably, its changes with the imposed stress and the density of the suspension in real space capture the observed changes in the anisotropy of the correlation functions in force space. As in the earlier work [142], we start from the distributions of macroscopic quantities that are measured in particle based simulations in real space of model DST suspensions [83, 130]. The simulation results illustrate the changing nature of fluctuations as DST is approached and provide evidence of non-trivial, highly correlated fluctuations. We use the microscopic information contained in the simulations, i.e. the local forces exchanged by the grains, to construct, through the constraints of local force balance, the representation of the shear thickening suspensions in terms of the underlying force network. To quantify the collective behavior of the changes detected in the force space representation, we apply a cluster analysis tool and show that two distinct clustering scales emerge as DST is approached, reflecting a scale separation of contact forces. From the representations of different flow-states, we construct an effective interaction potential in force space through a coarse-graining procedure, which is justified by the scale separation observed in the cluster analysis. We find that changes occur in this potential as a function of packing fraction and stress close to DST. Following a possible analogy with equilibrium statistical mechanics, molecular dynamics simulations based on this effective potential suggest that the different regions of the shear-thickening flow-state diagram stem from qualitatively different underlying force-space state diagrams across the transition, whose differences can be traced back to the changes in the effective potential. We discuss the implications that the observed changes in the coarse-grained potential may have

for the force space representation of the suspension and outline the emerging questions for future work on an effective field theory of the DST transition.

This paper is organized as follows. In Section A.2, we present a brief summary of the shear-stress controlled microscopic simulations. Section A.2.2 presents distributions of the strain rate obtained from time series of the simulations data. In Section A.3, we present a short description of the force-space representation. This is followed by the clustering analysis of particle patterns and force-space patterns in Section A.4. Finally, in Section A.5, we present our results for the effective interaction potential, and discuss the implications of our statistical analysis.

A.2 SIMULATION METHODS

We simulate a two-dimensional monolayer of non-Brownian spherical frictional particles that are immersed in a Newtonian fluid under an imposed shear stress σ_{xy} . This gives rise to a time-dependent shear rate $\dot{\gamma}$ [86, 127] and velocity field $\vec{v} = \dot{\gamma}(t)\hat{v}(\mathbf{x}) = \dot{\gamma}(t)(y, 0)$. Lees-Edwards periodic boundary conditions are used with $N = 2000$ particles in a unit cell. Bidisperse particles of radii a and $1.4a$ mixed at equal volume fractions are used to avoid ordering during flow [84]. In the simulation scheme presented here, the particles interact through near-field hydrodynamic interactions (lubrication), a short-ranged repulsive force, and frictional contact forces. The simulation model used here has been shown to accurately reproduce the experimentally measured rheology for dense shear-thickening suspensions [84, 126].

The motion is considered to be inertialess, so that the equation of motion reduces to force/torque balance between hydrodynamic (\vec{F}_H), repulsive (\vec{F}_R), and contact (\vec{F}_C) interactions,

$$\vec{0} = \vec{F}_H(\vec{X}, \vec{U}) + \vec{F}_C(\vec{X}) + \vec{F}_R(\vec{X}), \quad (\text{A.1})$$

where \vec{X} and \vec{U} denote the positions and velocities/angular velocities of all particles, respectively. The repulsive force \vec{F}_R is conservative in nature and can be determined based on the positions \vec{X} of the particles. On the other hand, calculation of the tangential component of the contact force \vec{F}_C is more involved as it also depends on the contact deformation history.

The translational velocities are non-dimensionalized by $\dot{\gamma}a$ and the shear rate and rotation rates by $\dot{\gamma}$. The hydrodynamic force is the sum of forces arising from the drag due to the motion of the particle relative to the surrounding fluid and the resistance to deformation imposed by the flow:

$$\vec{F}_H(\vec{X}, \vec{U}) = -\mathbf{R}_{FU}(\vec{X}) \cdot (\vec{U} - \dot{\gamma}\hat{U}^\infty) + \dot{\gamma}\mathbf{R}_{FE}(\vec{X}) : \hat{E}^\infty, \quad (\text{A.2})$$

where $\hat{U}^\infty = (\hat{v}(y_1), \dots, \hat{v}(y_N), \hat{\omega}(y_1), \dots, \hat{\omega}(y_N))$, and $\hat{E}^\infty = (\hat{e}(y_1), \dots, \hat{e}(y_N))$ is the normalized strain rate tensor. \mathbf{R}_{FU} and \mathbf{R}_{FE} are position-dependent resistance tensors and include the ‘‘squeeze’’, ‘‘shear’’ and ‘‘pump’’ modes of pairwise lubrication [8], as well as one-body Stokes drag. Regularization of the resistance matrix is achieved by introducing a small cutoff length scale $\delta = 10^{-3}$, typical for non-Brownian suspensions [84]. This regularization emulates the occurrence of contacts between particles due, for example, to surface roughness. The lubrication force is upper-bounded, and negative interparticle gaps l (i.e., particle overlaps) are allowed in our simulations.

We use a stabilizing repulsive force decaying exponentially with the interparticle gap $l \geq 0$ as $|\vec{F}_R| = F_0 \exp(-l/\lambda)$, with a characteristic Debye length λ . This force represents an electrostatic double layer interaction between particles. In the simulations presented in this study, we use $\lambda = 0.02a$.

To model contacts between particles – which occur only when the shear force is large enough to overcome the repulsive force F_0 – we use linear springs with both normal and tangential components, as is commonly done in soft-sphere Discrete Element Method

(DEM) simulations for dry grains [33, 82]. Note, however, that there is no dashpot in this model, since hydrodynamic resistance provides the source of energy dissipation. The corresponding normal (k_n) and tangential (k_t) spring constants used here satisfy $k_t = 0.5k_n$. The tangential and normal components of the contact force $F_C^{(ij)}$ between two particles satisfy Coulomb's friction law, i.e., $|F_{C,t}^{(ij)}| \leq \mu |F_{C,n}^{(ij)}|$ with μ being the interparticle friction coefficient. In this study, we use $\mu = 1$. This value of friction coefficient μ is comparable to experimentally measured values [42], where μ is reported to be in the range 0.6–1.1 for polymer brush-coated quartz particles of diameter $2a \sim 10 \mu\text{m}$, while it is higher than the value of 0.5 reported by Comtet *et al.* [30]. Some softness is allowed at the contact; we tune the spring stiffness for each (ϕ, σ_{xy}) such that the maximum overlaps between particles do not exceed 3% of the particle radius during the simulation, thereby staying close to the rigid limit [84, 128, 129].

The equation of motion (A.1) is solved under the constant shear stress σ_{xy} constraint. At any time during the simulation, the shear stress in the suspension is given by

$$\sigma_{xy} = \Sigma_{12} = \dot{\gamma}\eta_0 \left(1 + \frac{5}{2}\phi\right) + \dot{\gamma}\eta_H + \sigma_R + \sigma_C \quad (\text{A.3})$$

where η_0 is the viscosity of the suspending fluid, $\eta_H \dot{\gamma} = \dot{\gamma} V^{-1} \{(\mathbf{R}_{SE} - \mathbf{R}_{SU} \cdot \mathbf{R}_{FU}^{-1} \cdot \mathbf{R}_{FE}) : \hat{\mathbf{E}}^\infty\}_{12}$ is the contribution of hydrodynamic interactions to the stress, and $\sigma_{R,C} = V^{-1} \{\mathbf{X} \mathbf{F}_{R,C} - \mathbf{R}_{SU} \cdot \mathbf{R}_{FU}^{-1} \cdot \mathbf{F}_{R,C}\}_{12}$, where \mathbf{R}_{SU} and \mathbf{R}_{SE} are position-dependent resistance matrices giving the lubrication stresses from the particle velocities and resistance to deformation, respectively [69, 84], and V is the volume of the simulation box. At a fixed shear stress σ_{xy} the shear rate $\dot{\gamma}$ is the dependent variable which is calculated at each time step using [86]

$$\dot{\gamma} = \frac{\sigma_{xy} - \sigma_R - \sigma_C}{\eta_0 \left(1 + 2.5\phi\right) + \eta_H}. \quad (\text{A.4})$$

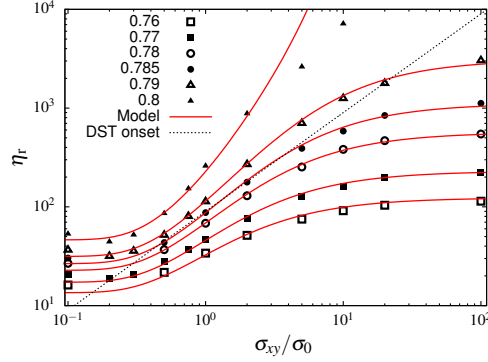


Figure A.1: Flow curves. Relative viscosity η_r plotted as a function of dimensionless applied stress σ_{xy}/σ_0 . The symbols are simulation data for various packing fractions. The solid lines are predictions from Eq. (A.6) for $\sigma^* = 0.78\sigma_0$. The dashed line represents $\eta_r \propto \sigma_{xy}/\sigma_0$, representing DST.

The full solution of the equation of motion (A.1) under the constraint of constant fixed stress (A.3) thus reduces to calculating the velocity [86]

$$\mathbf{U} = \dot{\gamma} \hat{\mathbf{U}}^\infty + \mathbf{R}_{\text{FU}}^{-1} \cdot (\dot{\gamma} \mathbf{R}_{\text{FE}} : \hat{\mathbf{E}}^\infty + \mathbf{F}_R + \mathbf{F}_C). \quad (\text{A.5})$$

From these velocities, we update the positions at each time step.

Lastly, the unit scales for strain rate is $\dot{\gamma}_0 \equiv F_0/6\pi\eta_0 a^2$ and $\sigma_0 \equiv \eta_0 \dot{\gamma}_0 = F_0/6\pi a^2$ for the stress.

A.2.1 FLOW CURVES AND FLOW STATE DIAGRAM

Fig. A.1 shows relative viscosity η_r plotted as a function of scaled shear stress σ_{xy}/σ_0 for simulations at several packing fractions. The relative viscosity data shows features typical of dense non-Brownian suspensions: shear thinning at low stress (arising due to the specific simulation model used here), thickening at intermediate stresses, and plateauing at high stresses $\sigma_{xy}/\sigma_0 > 10$. It has been previously shown that the physics behind shear thickening

and thinning are distinct [84, 130]; hence, in the following we only focus on the thickening behavior.

We observe that the extent of thickening increases with ϕ . To characterize the steepness of the viscosity in the $\eta(\sigma_{xy}/\sigma_0)$ flow curve, the shear thickening portion is fitted to $\eta \propto (\sigma_{xy}/\sigma_0)^\beta$, where $\beta < 1$ signifies Continuous Shear Thickening (CST), $\beta = 1$ implies that the viscosity increases for unchanging shear rate $\dot{\gamma}/\dot{\gamma}_0 = \eta/(\sigma_{xy}/\sigma_0)$ and hence indicates the onset of DST, and $\beta > 1$ designates DST. In this way, we identify $\phi = 0.785$ as the packing fraction at the onset of DST between two flowing states, as is evident from $\eta_r \propto (\sigma_{xy}/\sigma_0)^\beta$ (i.e., $\beta = 1$) in Fig. A.1.

The simulation data is described well by an analytical mean-field theory, which is a slight extension of that initially proposed by Wyart and Cates [153]. This theory, used to describe the rheology and flow-state diagram of dense suspensions, centers on the fraction of frictional contacts in the system, $f(\sigma_{xy})$, as a singular measure of the crossover between two distinct stress-independent rheologies at low and high stresses – namely, a lubricated, frictionless branch, and a frictional branch with a non-zero value of the microscopic friction coefficient, μ .

Using f , we can introduce stress-dependent rheological quantities that interpolate between their lubricated and fully-frictional values. In particular, the stress-dependent viscosity can be written as

$$\eta_r(\phi, \sigma_{xy}) = \alpha_m(\sigma_{xy}) [\phi_m(\sigma_{xy}) - \phi]^{-2}, \quad (\text{A.6})$$

where the stress-dependent jamming volume fraction is

$$\phi_m(\sigma_{xy}) = \phi_j^\mu f(\sigma_{xy}) + \phi_j^0 [1 - f(\sigma_{xy})], \quad (\text{A.7})$$

and the stress-dependent coefficient is

$$\alpha_m(\sigma_{xy}) = \alpha^\mu f(\sigma_{xy}) + \alpha^0 (1 - f(\sigma_{xy})), \quad (\text{A.8})$$

in which $\alpha^{0,\mu} = 0.102, 0.173$ are stress-independent constants determined via fits to the viscosities of systems of frictionless and frictional particles, respectively. Finally, the fraction of frictional contacts is modeled as $f(\sigma_{xy}) = \exp[-\sigma^*/\sigma_{xy}]$, based on previously published results [55, 59, 84, 96, 117, 130], with $\sigma^* = 0.78\sigma_0$, as determined by fit to the $\phi = 0.76$ data.

The viscosity curves modeled by Eq. (A.6) are compared to simulation data in Fig. A.1 and show good agreement, overall.

The fit of this mean-field model to the simulation data is presented as a flow state diagram in $\phi - \sigma_{xy}/\sigma_0$ space in Fig. A.2, in which three important packing fractions, ϕ_C , $\phi_J(\mu)$, and ϕ_J^0 , are indicated by vertical lines. Above ϕ_J^0 there is no flow at any stress (without deformation of particles, which we have not explored here), while above $\phi_J(\mu)$ the frictional state is jammed. ϕ_C is the minimum packing fraction at which DST is observed.

In the low-stress portion of the state diagram, i.e., $\sigma_{xy}/\sigma_0 \ll 1$, the shear forces are smaller than the repulsive force, and, thus, particles do not come into contact. In this case, frictional forces are not activated, and so the rheology diverges at ϕ_J^0 . On the other hand, in the large-stress portion ($\sigma_{xy}/\sigma_0 \gg 1$), most of the close interactions (or “contacts”) are frictional, which leads to a divergence of the viscosity at $\phi_J^\mu < \phi_J^0$. In these stress extremes, the viscosity is stress-independent.

For intermediate stresses ($0.3 < \sigma_{xy}/\sigma_0 < 10$), continuous shear thickening is observed in the range of $\phi < \phi_C$. For $\phi_C \leq \phi < \phi_J^\mu$, DST is observed between two flowing states and is termed as DST₁. The dashed line is the envelope of the DST states, with ϕ_C being the point with the minimum ϕ value along this line. This line is determined as the locus of points for which $d\dot{\gamma}/d\sigma_{xy} = 0$ in a flow curve $\dot{\gamma}(\sigma_{xy})$. For $\phi > \phi_J^\mu$, the upper boundary of the DST region is actually jammed as shown by the stress-dependent jamming line $\phi_m(\sigma_{xy})$, thus DST occurs between flowing (low stress) and jammed (high stress) states, and is termed as DST₂. The stress required to observe shear thickening (CST) is indepen-

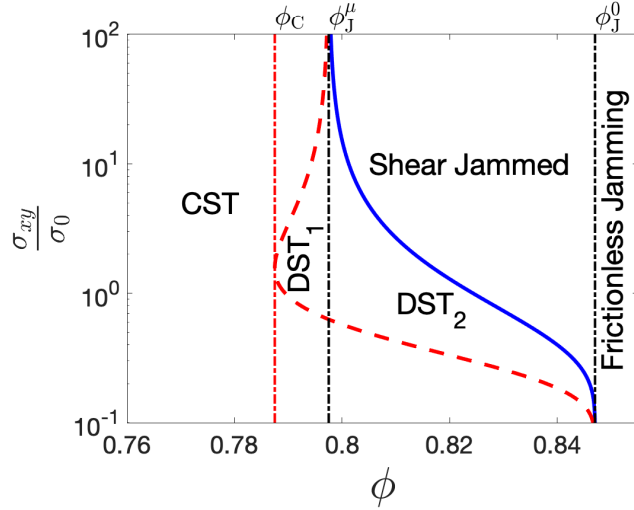


Figure A.2: Phase diagram in the shear stress–packing fraction (σ_{xy}, ϕ) plane. The left dashed curve (red) indicates the points where $\frac{d\dot{\gamma}}{d\sigma_{xy}} = 0$. The right solid curve (blue) illustrates the packing-fraction-dependent maximal stress above which the suspension is shear-jammed, i.e., above which no flowing states exist. The dashed and dotted-dashed vertical black lines represent the frictional and frictionless jamming points, respectively. Finally, the dashed vertical red line shows the minimum packing fraction ϕ_C at which DST is observed.

dent of the packing fraction, while the minimum stress required for DST and shear-jammed (SJ) states decreases with increase in packing fraction ϕ . Eventually these curves converge and the minimum stress for jamming tends to zero as the frictionless jamming point ϕ_J^0 is approached.

The data just discussed provides one indication that the mean-field model does not capture the complete physics of the DST transition, since it does not provide a quantitative description of η_r for $\phi = 0.80$ and high stresses ($\sigma_{xy}/\sigma_0 \geq 2$), as seen in Fig. A.1. In the next section, we show that this is the regime in which the strain-rate fluctuations exhibit significant non-Gaussian behavior.

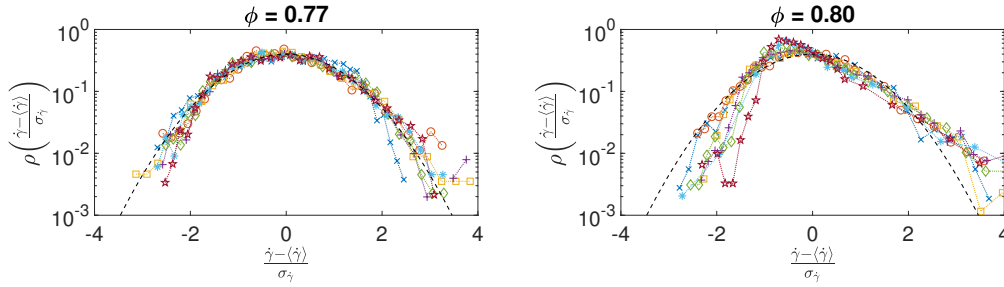


Figure A.3: Strain rate distributions. The curves in each figure represent probability distribution of strain rates ($\dot{\gamma}$) at different stresses (σ_{xy}/σ_0) at two different packing fractions: $\phi = 0.77$ (left) and $\phi = 0.80$ (right). The stresses at which the distributions are plotted are: $\sigma_{xy}/\sigma_0 = 0.5$ (blue), $\sigma_{xy}/\sigma_0 = 1.0$ (red), $\sigma_{xy}/\sigma_0 = 2.0$ (yellow), $\sigma_{xy}/\sigma_0 = 5.0$ (purple), $\sigma_{xy}/\sigma_0 = 10.0$ (green), $\sigma_{xy}/\sigma_0 = 20.0$ (cyan) and $\sigma_{xy}/\sigma_0 = 100.0$ (brown). The deviations from the Gaussian (black dashed) distribution are much more pronounced at $\phi = 0.80$, as compared to $\phi = 0.77$. The average strain rate ($\langle \dot{\gamma} \rangle$) and standard deviation ($\sigma_{\dot{\gamma}}$) of the NESS have been used to scale the distributions at different stresses.

A.2.2 STRAIN RATE DISTRIBUTIONS

The viscosity, and flow-state diagram summarized above, provide a description of the time-averaged properties of the DST transition that is now fairly well established [84, 126]. The flow curves are obtained by computing $\langle \dot{\gamma} \rangle$, the time average of $\dot{\gamma}$ calculated from Eq. A.4. A question that has not been explored in any great depth is how the fluctuations about the averaged quantities evolve with packing fraction and shear stress in this numerical model of DST. Experiments indicate large-temporal fluctuations of the stress detected by a rheometer under controlled shear rate [113].

In this section, we analyze the evolution of the temporal fluctuations of $\dot{\gamma}$ as ϕ and σ_{xy} are varied across the DST transition in Fig. A.2. As seen from Fig. A.3, the fluctuations of $\dot{\gamma}$ are distributed narrowly around the mean for ϕ in the CST regime ($\phi = 0.77$). In the DST regime ($\phi = 0.80$), however, one observes significant non-Gaussianity in the distributions. Although the system size in the simulations is relatively small and probably not sufficient to

establish the exact form of the distribution, the qualitative change we detect from $\phi = 0.77$ to $\phi = 0.80$ for a given system size points to the presence of longer-ranged correlations. It is to be noted that the non-Gaussian behavior is pronounced only within the DST region of the phase diagram where the viscosity is anomalously high, and is not a simple consequence of the $\dot{\gamma} = 0$ cutoff on the distribution, since that would occur at any density at low enough stresses.

The presence of anomalous (non-Gaussian) temporal fluctuations raises the question of what local interactions can lead to the system slowing down or speeding up as a whole. Earlier studies of pair correlations [83] of grains failed to identify any significant changes in positional correlations. This observation is not inconsistent with the model of DST based on the nature of contact forces changing from lubricated to frictional, since relatively small changes in positions of the grains are all that is required to trigger this transition. A representation that is sensitive to these changes in the contact forces are force-tiles (Maxwell-Cremona diagrams) [122, 147]. This was the representation previously used in constructing the statistical theory of the stress anisotropy [142]. In the next section, we review the construction of force-tiles and the evolution of correlations in this space across the DST transition.

A.3 CORRELATIONS IN FORCE SPACE

In steady state, flowing suspensions provide an ensemble of microscopic states that could constitute, in principle, the basis for a statistical mechanics description of the non-equilibrium transition associated to shear thickening. The equations of motion that generate those microscopic states are determined by the constraints of force balance. The idea that the forces acting on the grains and the constraints that emerge from mechanical stability can provide the right statistical ensemble to build a statistical mechanics frame-

work for athermal jammed systems has been developed and explored in the context of granular materials (a review appears in Ref. [13]), and recently extended to shear thickening suspensions [142]. In two-dimensional systems, the force balance constraints can be naturally accounted for by working in a dual space, known as a force tiling. In a force balanced configuration of grains with pairwise forces, the “vector sum” of forces on every grain, i.e. the force vectors arranged head to tail (with a cyclic convention), form a closed polygon. Next, because of Newton’s third law, every force vector in the system has an equal and opposite counterpart that belongs to its neighboring grain. This leads to the force polygons being exactly edge-matching. Extending this to all particles within the system leads to a force tiling [122, 147]. In this representation, the pairwise forces acting at each contact between two grains correspond to edges (or bonds). The vertices where the bonds meet identify vectors in this space, the vector height fields \vec{h} , such that the differences between two such vectors connected to the same bond gives the pairwise force acting on the contact represented by that bond (see Fig. A.4). The adjacency of the faces in the tiling is the adjacency of the grains, whereas the adjacency of the vertices is the adjacency of the voids (the heights are associated with the voids in the network). For the suspensions, in addition to the pairwise forces between grains, each particle experiences a hydrodynamic drag, which can be represented as a body force. Imposing the constraints of vectorial force balance in the presence of body forces leads to a unique solution for modified height fields, given the geometrical properties of the contact network [111].

It is important to notice that the height (or force space) representation is ideally suited for exploring the statistical properties of stresses, both local and global. In the continuum, the height fields define the local Cauchy stress tensor, by the relation $\sigma = \nabla \times \vec{h}$, and the area integral of σ , or the force moment tensor, Σ [58], in terms of difference of the height fields across the system:

$$\boldsymbol{\sigma} = \begin{pmatrix} \partial_y h_x & \partial_y h_y \\ -\partial_x h_x & -\partial_x h_y \end{pmatrix}; \boldsymbol{\Sigma} = \begin{pmatrix} L_y \Gamma_{yx} & L_y \Gamma_{yy} \\ -L_x \Gamma_{xx} & -L_x \Gamma_{xy} \end{pmatrix} \quad (\text{A.9})$$

where $\vec{\Gamma}_{x(y)}$ represents the sum of forces along the $x(y)$ directions, and $L_{x(y)}$ represents the linear dimensions of the system ($\boldsymbol{\sigma} = \boldsymbol{\Sigma}/L_x L_y$). Additionally, global torque balance implies $\Sigma_{xy} = \Sigma_{yx}$. In our simulations $L_x = L_y = L$, hence $\Gamma_{yy} = -\Gamma_{xx} = L\sigma_{xy}$.

At a microscopic level, each force tiling is specified by a set of vertices and a set of edges that connect these vertices. The distances between the vertices quantify the internal stress in the system, whereas the edges, which quantify the specific contact forces in a configuration, can be thought of, in a statistical sense, as fluctuating quantities, with connections between pairs of vertices chosen with some weights. We can therefore think of the vertices of the force tilings as the points of an interacting system of particles. The effective interactions between the vertices arise from the constraints of mechanical equilibrium, and from integrating out the edges.

Using the pair correlation function in force space (i.e. the pair correlation function of the height fields over the force tiling) one can construct an a priori probability distribution for the microscopic states (i.e. the different force tiles corresponding to the contact network of the grains under flow) and use it to define the relevant statistical ensemble to which the non-equilibrium steady states (NESS) in a dense suspension at a given σ_{xy} and ϕ can be mapped [142]. Such an ensemble has been proven to successfully describe the steady-state averages and the flow-state diagram. Here we pursue a similar approach, however, we devise an explicit coarse-graining scheme to construct an effective potential that describes the interactions of height vertices separated by distances that correspond, statistically, to the non-hydrodynamic contact forces. The coarse-graining scheme relies on a separation of scales that we identify using a clustering algorithm that is presented in the next section.

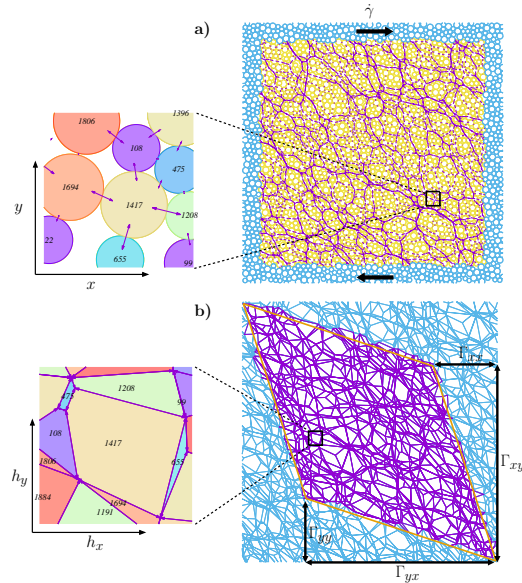


Figure A.4: Force tile construction. a) A snapshot of a suspension of 2000 soft frictional disks sheared at a variable strain rate $\dot{\gamma}$, with the shear stress σ_{xy} held fixed [142]. The lines represent the pair-wise (lubricated and frictional contact) force vectors between the individual grains. b) The force tiling associated with this flowing dense suspension. The bonds correspond to the pairwise forces, with larger polygons representing grains with higher stress. The vertices of the tiling represent height vectors $\vec{h} = (h_x, h_y)$, whose difference provides the pairwise force at each bond. $\vec{\Gamma}_x = (\Gamma_{xx}, \Gamma_{xy})$ and $\vec{\Gamma}_y = (\Gamma_{yx}, \Gamma_{yy})$ represent the sum of forces in the x and y directions respectively. The regions outside the parallelogram represents periodic copies of the system.

A.4 CLUSTERING IN REAL SPACE AND FORCE SPACE

As we have discussed at length, the phenomenon of DST arises primarily from the switching of lubricated contacts to solid-on-solid frictional contacts triggered by changes in the positions of grains that are minuscule compared to the size of the grains. This separation of scales necessitates a study of correlations in both real-space and force-space. As is visually evident from Fig. A.4, there are correlations that exist between the positions of particles, and between the positions of the height vertices. Two-point correlations char-

acterized by the pair correlations functions $g(\vec{r})$ and $g^*(\vec{h})$ provide the simplest measure of correlations. Although $g(\vec{r})$ is different from that of an ideal gas, and reflects strong excluded-volume effects, it does not evolve significantly with ϕ or σ_{xy} [85]. Pair correlations in force-space, $g^*(\vec{h})$, were used to construct an effective potential [142] and a statistical model for DST. However, the strong clustering, which creates a very large peak in $g^*(\vec{h})$ at small h , leads to a very deep minimum at $h \approx 0$ in the effective potential because of its form $(-\ln(g^*(\vec{h})))$ that we have chosen. This feature hindered attempts to carry out detailed numerical analysis of the phase behavior arising from the potential and thereby incorporate fluctuations beyond the meanfield analysis [142]. Our objective is to use the force-space approach, which provides a more sensitive measure of clustering and correlations, to construct a coarse-grained effective potential that can describe the correlations at h scales that are relevant to the DST transition. To this end, we use a clustering algorithm to identify relevant scales in both real-space and h space.

We perform a density based clustering analysis of both grain positions and vertices of force tiles using the DBSCAN algorithm [40]. In the DBSCAN technique, the set of points belonging to a single cluster consists of the union of points contained within an initial circle of probing radius s centered at a given point, those contained within all circles of the same radius s successively centered at all other points contained within the initial circle, and so on in an iterative sequence that continues until there are no new points contained within any subsequently-drawn circle (see Fig. A.5 for an illustration). This algorithm thereby ensures that all pairs of points from two different clusters are separated by distances greater than the probing radius s .

In usual implementations of DBSCAN, an optimum probing radius is determined to identify the most pronounced clustering tendencies [40]. Our aim is to use DBSCAN to identify characteristic clustering scales, and analyze how these evolve with packing fraction and stress. Therefore, we do not implement the optimization procedure but instead

identify the scales by measuring the number of clusters as a function of the probing radius. In addition, we do not discard any points as “noise” points, which is the normal practice in DBSCAN by requiring a minimum density in a cluster. In our implementation, the minimum number of points in a cluster is one such that all points in a pattern are included in some cluster.

The value of $N_c(s)$ as $s \rightarrow 0$ has to be the total number of points in the system since each point forms its own cluster. As $s \rightarrow$ system size, $N_c(s) \rightarrow 1$. Our algorithm probes the density distribution of point patterns at different length scales by monitoring the number of clusters, $N_c(s)$, as a function of the probe size s . For a point pattern with uniform density, $N_c(s)$ decreases continuously with s . In a periodic lattice, where the distance distribution of nearest neighbors is a delta function, $N_c(s)$ exhibits a jump discontinuity at the lattice spacing. For a complex pattern, we expect $N_c(s)$ to show significant changes in its derivatives at scales where the distance distribution has structure.

As seen from Fig. A.6, the clustering properties of the grain centers in the CST regime ($\phi = 0.76$) and the DST regime ($\phi = 0.80$) are virtually identical. The abrupt decreases in $N_c(s)$ at $s = 2, 2.4, 2.8$ correspond to the first layer or ordering of the nearest neighbor grains, with splitting due simply to the bidispersity. Beyond these scales, $N_c(s)$ decreases smoothly, and therefore, the density is uniform.

The situation is dramatically different for the clustering properties of height vertices (Fig. A.7). In the CST regime, $N_c(s^*)$ decays continuously with s^* , except for a small plateau region at intermediate values of s^* . In the DST regime, we can clearly identify three different decay regimes in $N_c(s^*)$: an initial, relatively fast decay to a plateau with very slow decay, followed by a smooth decay. The length of the plateau is sensitive to the stress, as is clearly evident in the plots of the derivatives. The plateau developing at larger packing fractions and stresses is a signature of the clustering of the small-scale clusters into meta-clusters. The length of the plateau is a measure of the scale of this meta-clustering. It is the

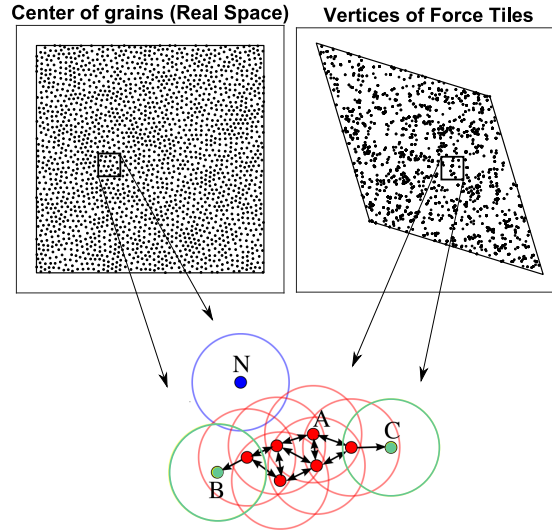


Figure A.5: DBSCAN algorithm. Top panel shows representative point patterns from the simulations in real space (centers of grains) and force-space (vertices of force tiles). The bottom panel illustrates the application of the DBSCAN algorithm [40] to such point patterns. The red points (A) belong to one cluster since all of these points can be reached by drawing circles with the probing radius s , centered at these points. The double-headed arrow between red points indicates that one can reach these points linked by the arrow traversing in multiple ways. The green points (B, C) are the endpoints of the cluster, and can be reached only from the penultimate particle as shown by a single-headed arrow. The blue point (N) is an example of a “noise” or isolated point. It is the lone point of the cluster, i.e., it is not reachable from any other point by drawing circles of the radius (s).

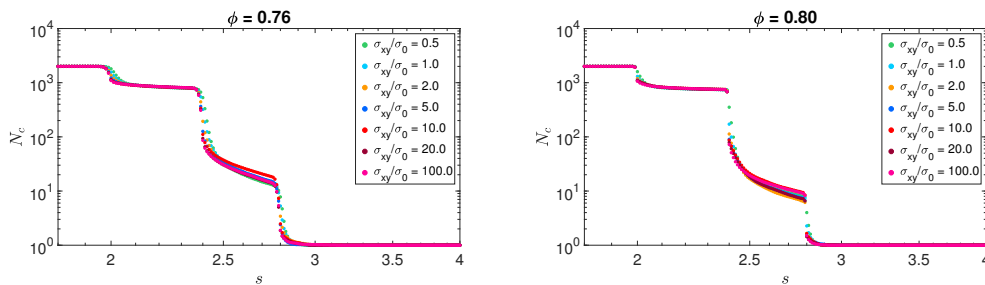


Figure A.6: Real space DBSCAN analysis. Number of clusters (N_c) obtained from the DBSCAN analysis for $\phi = 0.76$ (left) and for $\phi = 0.80$ (right) for different stresses (σ_{xy}/σ_0) as function of length scale (s), which is measured in units of the small-grain diameter. The DBSCAN analysis is performed on the point pattern of the centers of grains in a given configuration of the NESS. The results are then averaged over the ensemble of configurations sampled in the dynamics. The three sharp drops in $N_c(s)$ at $2 \leq s \leq 3$ are indicative of the bidispersity of grain sizes and a clear layering of nearest neighbors.

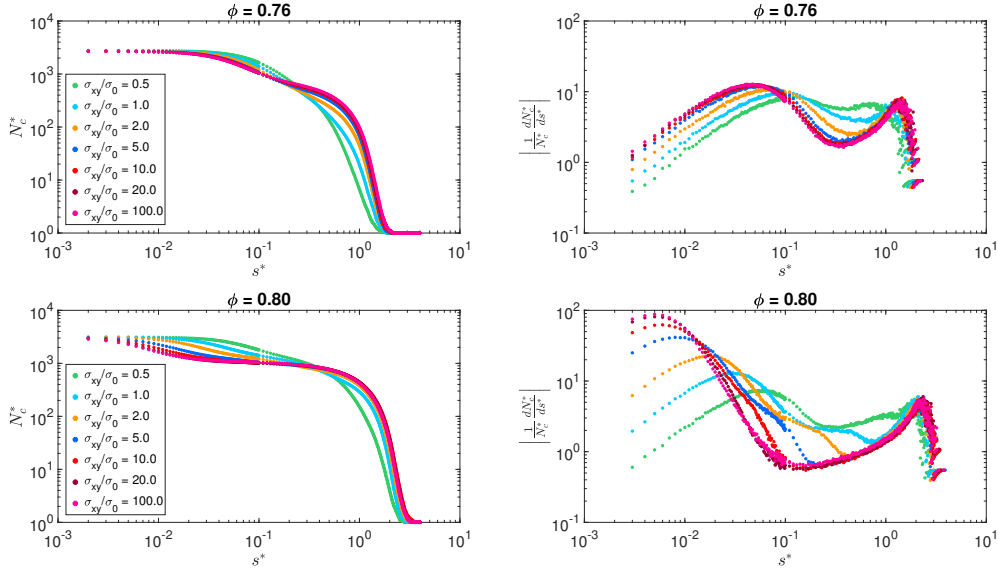


Figure A.7: Force space DBSCAN analysis. Number of clusters ($N_c^* \equiv N_c(s^*)$) obtained from the DBSCAN analysis (left) and its derivative with respect to the probing length (s^*) (right) for different packing fractions (ϕ) and stress (σ_{xy}/σ_0). Emergence of a separation of scales is evident in the derivative plots.

meta-clustering that shows significant changes across DST. An earlier analysis [121] led to similar conclusions. We note that vertices that are close to each other are not necessarily connected by an edge in the tiling. Therefore, the distance distribution is not equivalent to the contact force distribution.

The structure in $N_c(s^*)$ at small s^* reflects the small-scale clustering of height vertices that arise, statistically, from the small contact forces. As noted earlier, these forces arise primarily from distributing the hydrodynamic drag force between contacts, and we would like to exclude them from our statistical analysis. Our interest is in constructing an effective potential that captures the changes brought about by switching from lubricated to frictional forces. These occur at scales $s^* \geq 1$, which corresponds to forces that are comparable in magnitude to the boundary dimensions of the force tiles (Fig. A.4). In the next section,

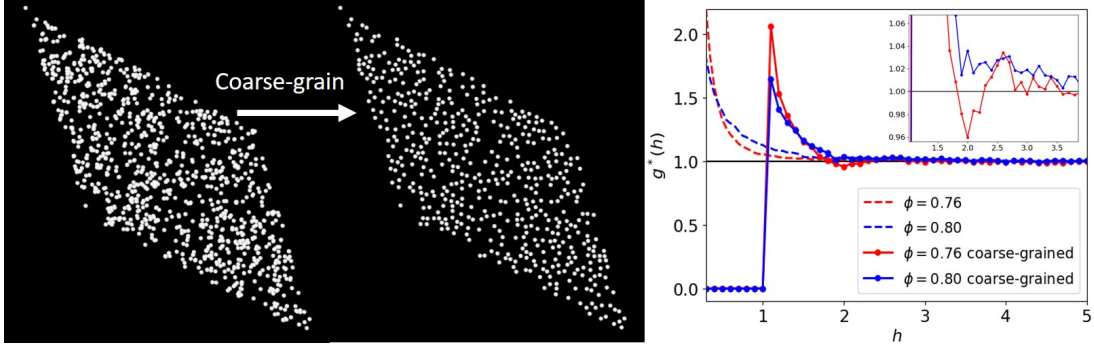


Figure A.8: Coarse-graining force vertex distributions. Snapshots show the change in our system after applying a coarse-graining procedure. While the point number has significantly decreased, the larger scale structures seem unaffected. Quantitatively, $g^*(h)$ shows that the low h peak has been cutoff at $h = 1.1$ (the size of the bins we used for our clustering) and is now able to capture longer range structure that was drowned out by the extreme short-range clustering.

we present our systematic coarse-graining approach, which leads to the desired effective potential.

A.5 CONSTRUCTING EFFECTIVE POTENTIALS

In order to focus on the larger forces, i.e. the larger length scale in force space as highlighted by the DBSCAN-based clustering analysis, we adopted a coarse-graining procedure for height vertices. The basic idea is to replace the tightly packed clusters of points with effective points representing these small clusters. This was carried out for each configuration by creating an empty replica, looping through the vertices randomly, and adding a point to the replica if its distance from any points already in the replica was $\geq l_{bin}$. Varying l_{bin} (expressed in units of $F_0\sigma_0/\sigma_{xy}$, defined in Section A.2) provides different extents of coarse-graining and may change the characteristics we discuss in the following. Nevertheless, a reasonable choice is a value of l_{bin} that preserves the structure in force space that

is indicated by the DBSCAN analysis (Fig.A.7) while removing the small-scale clustering associated primarily with hydrodynamic drag forces. In the following we discuss the results obtained for a binning size $l_{bin} = 1.1$ that satisfies this criterion. In particular we compare the results obtained for a packing fraction of the grains, $\phi = 0.76$, which corresponds to systems that lie in the CST part of the flow-state diagram for any value of the imposed shear stress, to those for $\phi = 0.80$, which corresponds to systems that undergo DST upon increasing the imposed stress (see Fig. A.2).

Analyzing the resulting coarse-grained height vertex configurations, we can see that the coarse-graining procedure decreases clumping at small distances while maintaining the same overall distribution at larger scales (Fig. A.8). Indeed, when we compute $g^*(h)$ we can clearly see the signs of longer-range structure, differently from the $g^*(h)$ computed before coarse-graining which was completely dominated by the peak near $h \approx 0$. Moreover we notice that the coarse-graining procedure reveals some qualitative differences between the pair correlations at volume fractions that correspond or not to a DST region of the flow-state diagram. In particular, compared to $\phi = 0.80$, there is a dip in the correlations around $h = 2$ for $\phi = 0.76$. Notably, this difference appears even in the radially-averaged $g^*(h)$ which ignores the anisotropy that was the primary focus of the earlier force-space based effective potential [142]. Without the coarse-graining procedure, the main difference that had been noted between volume fractions was the change in anisotropy. This observation provides an alternative approach to constructing a statistical mechanics framework based on a central potential, which facilitates numerical simulations beyond mean-field calculations.

We can now compute an effective pair potential from the pair correlation function of the coarse-grained height configurations as $V^*(h) = -\ln[g^*(h)]$. Since by coarse-graining we have erased the correlations at $h < l_{bin} = 1.1$, we avoid the problem of a very deep minimum at $h \approx 0$. Doing so reveals a short range well for both densities (i.e. both in the CST and DST regimes) and a repulsive shoulder in $V^*(h)$ around $h = 2$ for the $\phi = 0.76$ poten-

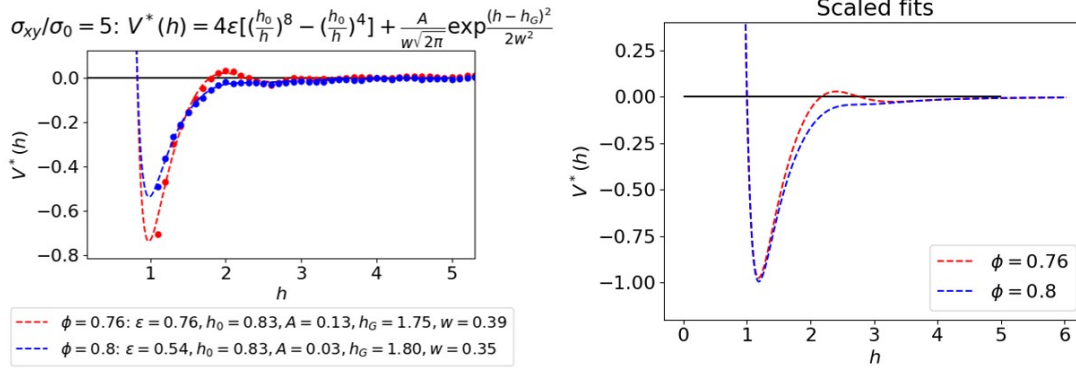


Figure A.9: Effective interaction potentials. From the measured $g^*(h)$, it is possible to construct a pair potential that goes as $V^*(h) = -\ln[g^*(h)]$. The dots in this plot represent this $V^*(h)$. To this, we fit an effective pair potential that consists of a LJ-style well plus a Gaussian bump. Fitting parameters are listed in legend. Scaling the potential by the LJ fit parameters shows the clear qualitative and quantitative differences in the shoulder at $h = 2$ that depends strongly on ϕ .

tial (Fig. A.9). This last feature appears instead to be dependent on ϕ and is suppressed in the DST regime—which holds true for systems across the full range of applied stresses. If we were to construct an analogous thermal system of particles interacting through such a potential, the presence of a short range minimum would produce a gas-liquid phase separation with clustered non-equilibrium states in various conditions [6]. These clustered states are typically isotropic for a central potential. The secondary length scale introduced by the repulsive shoulder, on the other hand, can qualitatively change the equilibrium phase diagram associated with the potential and, as a consequence, also the non-equilibrium states accessible under different conditions. A competing secondary length scale can in fact introduce different spatially modulated and even anisotropic equilibrium phases which may in turn favor spatially modulated non-equilibrium states [28, 64]. These changes in the phase diagram can suppress, in certain cases, the gas-liquid phase separation and quali-

tatively change the nature of the density fluctuations [18, 88]. A proper analogy between thermal systems and the force space representation of non-equilibrium steady states of shear-thickening suspensions is far from being worked out. However, the above observations suggest that the force space representation could be akin to a thermal system whose accessible microstates change with a change in the shape of the interaction potential, which occurs across the CST-DST boundary in sheared suspensions.

To illustrate the fact that the changes in the shape of the potential detected here can modify the microstates accessible to the force space representation of the suspension, we have turned the coarse-grained effective potentials into an analytical form that can be used in molecular dynamics (MD) numerical simulations. A Lennard-Jones (LJ) style attractive well plus a Gaussian bump provides a reasonable fit of all the potentials obtained from the force space representation of the shear thickened suspensions, as shown in Fig. A.9 (left). Scaling the fits by the LJ parameters (right) clearly shows that the repulsive bump (or shoulder) at $h \approx 2$ disappears in the DST region: the scaled fits obtained for different imposed stresses lie on top of each other for $\phi = 0.76$; however, they vary as a function of the stress for $\phi = 0.80$, with the maximum decreasing upon crossing into the DST region. We have then performed *NVT* MD simulations of point-like particles interacting through the coarse-grained effective potentials just discussed.¹

To explore the accessible states under different conditions, we vary the density and the temperature of this fictitious thermal system. The number of particles is varied between 1000 and 8000 while keeping the system size fixed. The particles are initially placed randomly and given a random velocity sampled from a Maxwell-Boltzmann distribution centered around the chosen temperature. The temperature used in the *NVT* simulations is set by the inverse energy scale, that corresponds to the maximum strength of the effective

¹We have used the LAMMPS library to perform simulations in a 2D square box with dimensions $L_x = L_y = 100$. [108]

potentials [45]. Starting with thermal energy equal to twice the potential well, we slowly reduce the temperature to the desired value. The rate is sufficiently slow that we do not see a rate dependence. Finally, we run the system at the final, fixed temperature.

Fig. A.10 shows state diagrams constructed from the two potentials of Fig. A.9, distinguishing clustered from non-clustered liquid states in force space, when the simulations are run in equivalent conditions, using exactly the same protocol and system size. The figure shows how clustering occurs under different conditions depending on the potential, and that the type of clustering can be qualitatively different. The effective potentials used are obtained for different densities of the suspension, and we know that varying the imposed load produces different densities of vertices in force space, but we do not yet have a clear understanding of what would play the role of temperature in the force space representation. Hence we cannot establish here a direct connection between the states sampled in the simulations (as for example shown in Fig. A.10) and those physically relevant to the force tiles of the sheared suspension. With respect to what variable in the hydrodynamic simulations maps most closely to the temperature in the NVT MD simulation of the points in force space, however, we note that the original force tiles from the hydrodynamic simulations are created from instantaneously force balanced states, which are explored under the external driving: the driving induces network rearrangements that allow the suspension to sample the microscopic states compatible with the force balance constraints. $V^*(h)$ is constructed with no information about the network reorganization, but contains information about the height vertex distribution. Is there a way to connect the sampling of the phase space associated with $V^*(h)$ via MD simulations to the way the suspension samples the microscopic NESS via real space dynamics due to the external driving? While this question requires a much deeper investigation, we speculate here that just as thermal fluctuations produce the noise that allows for phase space exploration in ordinary MD simulations, a similar role is played by the fluctuations in the shear rate of the suspensions subjected to an imposed shear

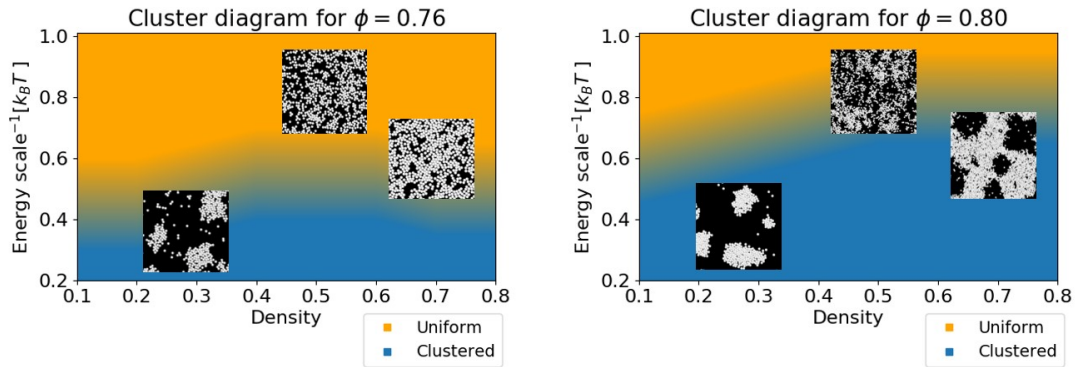


Figure A.10: State diagrams of the calculated potentials. We see a transition from a clustered to non-clustered fluid as we increase temperature. Snapshots illustrate the differences between the potentials when looking at the same temperature and density, with exactly the same simulation protocol. The types of clusters that form are different and the transition to the clustering regime happens at different temperatures.

stress. The fluctuations in the shear rate, such as the ones detected and discussed in Section A.2, are the manifestation of the system adjusting to the imposed driving by sampling the microstates compatible with the force balance constraints through network rearrangements. Since the network rearrangements are not explicitly included in the force space dynamics, they could translate into the noise needed to sample the force tiles associated to the real space dynamics of the grains.

The clustering of the points in force space obtained for the two effective potentials using the MD simulations (Fig. A.10) can be mainly ascribed to their short length-scale features [64]. Nevertheless, there are intriguing difference between the effective potentials at *larger* length-scales that can be better highlighted by analyzing the Fourier transform (Fig. A.11). The low q_h behavior can in general be fitted by a quartic polynomial, and plotting the q_h^2 coefficients as a function of stress in real space for the two volume fractions shows that the coefficients are always smaller for $\phi = 0.80$ and that they do not change much with the

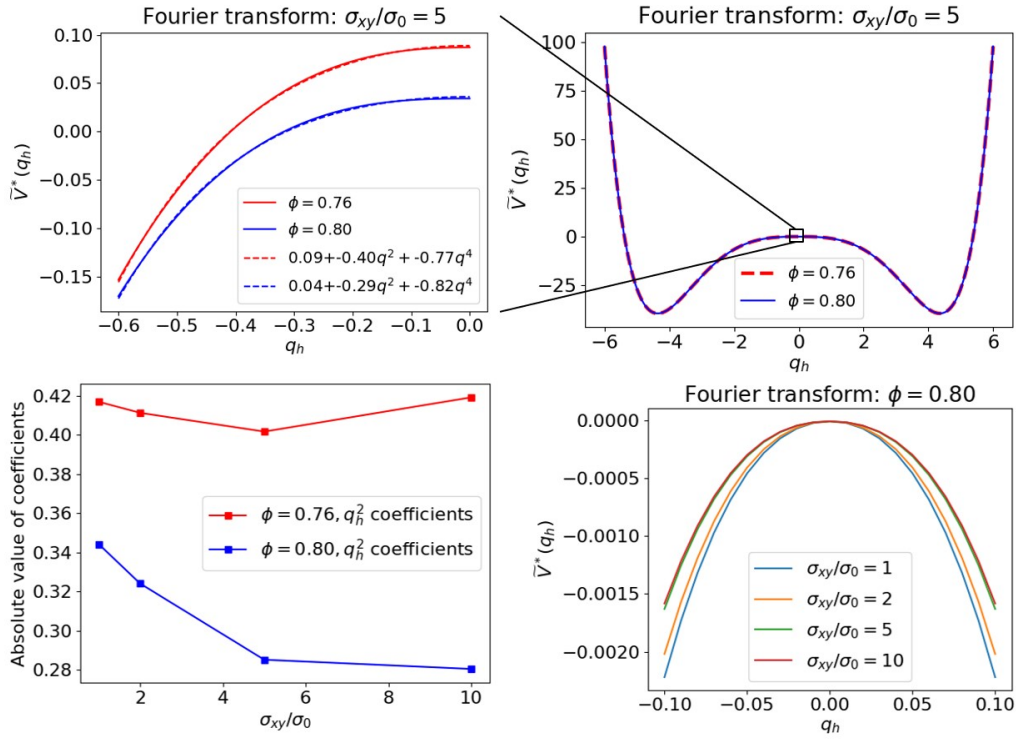


Figure A.11: Fourier analysis. Fourier transforms of potentials. **Top:** The transforms deviate only at low q_h , which corresponds to long distances. The large q_h behavior is virtually identical. At small q_h the potentials can be fit by a quartic polynomial. **Bottom:** Notably, the coefficients mainly differ for the q_h^2 terms. When plotting these for different stress σ_{xy}/σ_0 , we see that there is a significant drop in the DST region ($\phi = 0.80$) as stress increases. The lower q_h^2 coefficient corresponds to a flatter $\tilde{V}^*(q_h)$ near $q_h = 0$, as seen in the bottom right panel showing the transforms for different values of σ_{xy}/σ_0 . In this plot, a vertical shift has been applied to each transform so that $\tilde{V}^*(0) = 0$, making it easier to compare how the transforms approach this maximum for different σ_{xy}/σ_0 .

stress at $\phi = 0.76$, but they clearly decrease with the stress at $\phi = 0.80$. The decrease in the q_h^2 coefficient, while the q_h^4 coefficient remains steady, must correspond to a flattening of the potential. This difference can be seen when plotting the Fourier transforms at $\phi = 0.80$ for various stresses (Fig. A.11). These findings suggest that, in addition to density fluctuations associated to the minimum of $V^*(h)$, the change in the shape close to DST may promote fluctuations over larger scales. Thinking in terms of microstates that the dynamics could explore, the implications are that the shape of $\tilde{V}^*(q_h)$ can introduce a preferred pattern in the force tiles that is characterized by the q_h at which \tilde{V}^* has a minimum (q_h^{min}). If the q_h^2 coefficient is large, then a uniform configuration of contact forces will quickly reach a steady state characterized by the minimum. However, if the q_h^2 coefficient approaches zero, there could be long-lived transients with nearly uniform force distributions that will not resemble the structures corresponding to q_h^{min} .

Overall, the analysis performed in this section confirms the idea that the effective potential obtained with the coarse-graining procedure, albeit radially symmetric, can still capture some of the complexity of the spatial arrangement of the vertices in force space and contains important information about the physics of the different flow-states. Moreover, intriguing similarities with the dynamics of thermal systems suggest a possible path to sample the microscopic fluctuations of the shear thickening suspension in force space.

A.6 CONCLUSIONS

In this appendix we have sketched a possible path toward a statistical mechanics framework for shear thickening dense suspensions of grains that is based on the force space representation of the flowing suspension and naturally includes microscopic fluctuations. The overarching question is the nature of fluctuations and correlations close to DST beyond the mean field descriptions developed so far. Going beyond time-averaged properties, we

presented distributions of shear rates measured in microscopic simulations of a numerical model [84, 126] of suspensions undergoing DST. These distribution featured anomalous non-Gaussian fluctuations in the DST regime. While these fluctuations are suggestive of long-ranged microscopic correlations, microscopic measures of clustering of grain positions do not reveal any changes across the DST transition. However, while the clustering of particles in real space remained virtually unchanged on transitioning from CST to DST, the force-tile representation of the suspension, which is based on the network of forces acting between the grains, provided further insight. In this representation, the pair-wise forces are edges. The vertices where the edges meet define vectors in this space. The distance between the vertices quantify the internal stresses in the system. A clustering analysis, similar to the one applied in real space, revealed qualitative changes in the correlations between these height vertices as the suspension transitioned from CST to DST.

By implementing a coarse-graining procedure, we were able to filter out the hydrodynamic drag forces and focus on the contact forces that play the dominant role in DST. From the pair correlations of these coarse-grained points, we constructed an effective pair potential. Making an analogy between force vertices and point particles interacting through an effective potential, we probed the microscopic states accessible in force space in presence of these interactions and found that the changes detected in the potential shape far away from, and close to, DST may qualitatively change the type and degree of clustering that the force tiling can undergo. By analyzing the Fourier transform of the effective potentials, we detected intriguing differences in the low q_h behavior, signaling the possibility of long-ranged fluctuations. In particular, potentials constructed from force vertices in DST showed a change consistent with the presence of long-lived transients that are very different from the steady state—much like the anomalous strain rate fluctuations.

Building on this work, we will extend the MD simulations to explore the dynamical behavior more systematically. In particular, we need to better understand how the temper-

ature in the molecular dynamics simulations maps to network rearrangements and fluctuations in the flow of the suspension. The qualitative changes in $\tilde{V}^*(q_h)$ that accompany the CST to DST transition suggest that a fruitful avenue for going beyond mean-field theory is to construct the analog of a Ginzburg-Landau functional with the density in height space (force-tilings) serving as the order parameter [50]. Standard techniques can then be applied to compute correlation functions, and investigate singularities indicative of a non-equilibrium phase transition between the steady states of the suspension.

BIBLIOGRAPHY

- [1] José L.F. Abascal and Carlos Vega. Dipole-quadrupole force ratios determine the ability of potential models to describe the phase diagram of water. *Physical Review Letters*, 98(23):2005–2008, 2007. ISSN 00319007. doi: 10.1103/PhysRevLett.98.237801.
- [2] M. J. Abdolhosseini Qomi, K J Krakowiak, M Bauchy, K L Stewart, R Shahsavari, D Jagannathan, D B Brommer, A Baronnet, M J Buehler, S Yip, F. J. Ulm, K. J. Van Vliet, and R. J.M. Pellenq. Combinatorial molecular optimization of cement hydrates. *Nature Communications*, 5:1–10, 2014. ISSN 20411723. doi: 10.1038/ncomms5960. URL <http://dx.doi.org/10.1038/ncomms5960>.
- [3] A Allen, R Oberthur, D Pearson, P Schofield, and C Wilding. Development of the fine porosity and gel structure of hydrating cement systems. *Philosophical Magazine Part B*, 56:263–288, 1987. doi: 10.1080/13642818708221317#.VQzeVWZyOtM.
- [4] Andrew J. Allen, Jeffrey J. Thomas, and Hamlin M. Jennings. Composition and density of nanoscale calcium silicate hydrate in cement. *Nature Materials*, 6(4):311–316, 2007. ISSN 1476-1122. doi: 10.1038/nmat1871. URL <http://www.nature.com/doifinder/10.1038/nmat1871>.
- [5] M. P. Allen and D. J. Tildesley. *Computer Simulation of Liquids*. Oxford University Press, 1987. ISBN 978-0-19-855645-9.
- [6] Valerie J. Anderson and Henk N. W. Lekkerkerker. Insights into phase transition kinetics from colloid science. *Nature*, 416:811–815, 2002. doi: 10.1038/416811a.

- [7] Robbie M. Andrew. Global CO₂ emissions from cement production. *Earth System Science Data Discussions*, pages 1–52, 2018. ISSN 1866-3591. doi: 10.5194/essd-2017-77.
- [8] R. C. Ball and J. R. Melrose. A simulation technique for many spheres in quasi-static motion under frame-invariant pair drag and Brownian forces. *Phys. A*, 247(1–4):444–472, 1997.
- [9] V. Ballenegger and J.-P. P. Hansen. Dielectric permittivity profiles of confined polar fluids. *Journal of Chemical Physics*, 122(11):114711, 2005. ISSN 00219606. doi: 10.1063/1.1845431.
- [10] V. Baroghel-Bouny, M. Mainguy, T. Lassabatere, and O. Coussy. Characterization and identification of equilibrium and transfer moisture properties for ordinary and high-performance cementitious materials. *Cement and Concrete Research*, 29(8):1225–1238, 1999. ISSN 00088846. doi: 10.1016/S0008-8846(99)00102-7.
- [11] H. J. C. Berendsen, J. R. Grigera, and T. P. Straatsma. The missing term in effective pair potentials. *The Journal of Physical Chemistry*, 91(24):6269–6271, 1987. ISSN 0022-3654. doi: 10.1021/j100308a038. URL <http://pubs.acs.org/doi/abs/10.1021/j100308a038>.
- [12] Supriyo Bhattacharya and Keith E. Gubbins. Fast method for computing pore size distributions of model materials. *Langmuir*, 22(18):7726–7731, 2006. ISSN 07437463. doi: 10.1021/la052651k.
- [13] Dapeng Bi, Silke Henkes, Karen E. Daniels, and Bulbul Chakraborty. The Statistical Physics of Athermal Materials. *Annual Review of Condensed Matter Physics*, 6(1):63–83, 2015. ISSN 1947-5454. doi: 10.1146/annurev-conmatphys-031214-014336.

- [14] Patrick A. Bonnaud, Christophe Labbez, Ryuji Miura, Ai Suzuki, Naoto Miyamoto, Nozomu Hatakeyama, Akira Miyamoto, and Krystyn J. Van Vliet. Interaction grand potential between calcium silicate hydrate nanoparticles at the molecular level. *Nanoscale*, 8(7):4160–4172, 2016. ISSN 2040-3364. doi: 10.1039/C5NR08142D. URL <http://xlink.rsc.org/?DOI=C5NR08142D>.
- [15] Mehdi Bouzid and Emanuela Del Gado. Mechanics of Soft Gels: Linear and Nonlinear Response. In Wanda Andreoni and Sidney Yip, editors, *Handbook of Materials Modeling: Applications: Current and Emerging Materials*, pages 1–29. Springer International Publishing, Cham, 2019. ISBN 978-3-319-50257-1. doi: 10.1007/978-3-319-50257-1_129-2. URL https://doi.org/10.1007/978-3-319-50257-1_129-2.
- [16] Mehdi Bouzid, Jader Colombo, Lucas Vieira Barbosa, and Emanuela Del Gado. Elastically driven intermittent microscopic dynamics in soft solids. *Nature Communications*, 8(May):1–8, 2017. ISSN 20411723. doi: 10.1038/ncomms15846. URL <http://dx.doi.org/10.1038/ncomms15846>.
- [17] Mehdi Bouzid, Bavand Keshavarz, Michela Geri, Thibaut Divoux, Emanuela Del Gado, and Gareth H. McKinley. Computing the linear viscoelastic properties of soft gels using an optimally windowed chirp protocol. *Journal of Rheology*, 62(4):1037–1050, 2018. ISSN 0148-6055. doi: 10.1122/1.5018715. URL <http://dx.doi.org/10.1122/1.5018715><http://arxiv.org/abs/1805.07987><http://dx.doi.org/10.1122/1.5018715>.
- [18] S. A. Brazovskii. Phase transition of an isotropic system to a nonuniform state. In *30 Years of the Landau Institute – Selected Papers*, pages 109–113. aug 1996.

doi: 10.1142/9789814317344_0016. URL http://www.worldscientific.com/doi/abs/10.1142/9789814317344_{_}0016.

- [19] Sébastien Brisard and Pierre Levitz. Small-angle scattering of dense, polydisperse granular porous media: Computation free of size effects. *Physical Review E - Statistical, Nonlinear, and Soft Matter Physics*, 87(1):1–19, 2013. ISSN 15393755. doi: 10.1103/PhysRevE.87.013305.
- [20] Sebastien Brisard, Rosie S Chae, Isabelle Bihannic, Laurent Michot, Peter Guttman, Jürgen Thieme, Gerd Schneider, Paulo J M Monteiro, and Pierre Levitz. Morphological quantification of hierarchical geomaterials by X-ray nano-CT bridges the gap from nano to micro length scales. *American Mineralogist*, 97(2-3):480–483, feb 2012. ISSN 0003-004X. doi: 10.2138/am.2012.3985. URL <https://doi.org/10.2138/am.2012.3985>.
- [21] Eric Brown and Heinrich M Jaeger. Shear thickening in concentrated suspensions: phenomenology, mechanisms and relations to jamming. *Rep Prog Phys*, 77(4):046602, Apr 2014. doi: 10.1088/0034-4885/77/4/046602.
- [22] Jeffrey W Bullard, Hamlin M Jennings, Richard A Livingston, Andre Nonat, George W Scherer, Jeffrey S Schweitzer, Karen L Scrivener, and Jeffrey J Thomas. Mechanisms of cement hydration. *Cement and Concrete Research*, 41(12):1208–1223, 2011. ISSN 0008-8846. doi: 10.1016/j.cemconres.2010.09.011. URL <http://dx.doi.org/10.1016/j.cemconres.2010.09.011>.
- [23] R A Buswell, W R Leal De Silva, S Z Jones, and J Dirrenberger. 3D printing using concrete extrusion : A roadmap for research. *Cement and Concrete Research*, 112:37–49, 2018. ISSN 0008-8846. doi: 10.1016/j.cemconres.2018.05.006. URL <https://doi.org/10.1016/j.cemconres.2018.05.006>.

- [24] Benoit Carrier. *Influence of water on the short-term and long-term mechanical properties of swelling clays : experiments on self-supporting films and molecular simulations*. PhD thesis, Universite Paris-Est, 2014.
- [25] Michael E Cates and Matthieu Wyart. Granulation and bistability in non-brownian suspensions. *Rheologica Acta*, 53(10-11):755–764, 2014.
- [26] R. N. Chacko, R. Mari, M. E. Cates, and S. M. Fielding. Dynamic vorticity banding in discontinuously shear thickening suspensions. *Phys. Rev. Lett.*, 121:108003, Sep 2018. doi: 10.1103/PhysRevLett.121.108003. URL <https://link.aps.org/doi/10.1103/PhysRevLett.121.108003>.
- [27] Wei Shan Chiang, Emiliano Fratini, Piero Baglioni, Dazhi Liu, and Sow Hsin Chen. Microstructure determination of calcium-silicate-hydrate globules by small-angle neutron scattering. *Journal of Physical Chemistry C*, 116(8):5055–5061, 2012. ISSN 19327447. doi: 10.1021/jp300745g.
- [28] A. Ciach, J. Pękalski, and W. T. Gózdź. Origin of similarity of phase diagrams in amphiphilic and colloidal systems with competing interactions. *Soft Matter*, 9(27):6301, 2013. ISSN 1744-683X. doi: 10.1039/c3sm50668a. URL <http://xlink.rsc.org/?DOI=c3sm50668a>.
- [29] Jader Colombo and Emanuela Del Gado. Stress localization, stiffening, and yielding in a model colloidal gel. *Journal of Rheology*, 58(5):1089–1116, 2014. ISSN 0148-6055. doi: 10.1122/1.4882021. URL <http://dx.doi.org/10.1122/1.4882021>.
- [30] Jean Comtet, Guillaume Chatté, Antoine Niguès, Lydéric Bocquet, Alessandro Siria, and Annie Colin. Pairwise frictional profile between particles determines discontinuous shear thickening transition in non-colloidal suspensions. *Nat. Comm.*, 8:15633, 2017.

- [31] Jean Comtet, Guillaume Chatté, Antoine Niguès, Lydéric Bocquet, Alessandro Siria, and Annie Colin. Pairwise frictional profile between particles determines discontinuous shear thickening transition in non-colloidal suspensions. *Nature Communications*, 8:15633, 2017. doi: <https://doi.org/10.1038/ncomms15633>.
- [32] Georgios Constantinides and Franz Josef Ulm. The effect of two types of C-S-H on the elasticity of cement-based materials: Results from nanoindentation and micromechanical modeling. *Cement and Concrete Research*, 34(1):67–80, 2004. ISSN 00088846. doi: 10.1016/S0008-8846(03)00230-8.
- [33] P. A. Cundall and O. D. L. Strack. A discrete numerical model for granular assemblies. *Geotechnique*, 29:47–65, 1979.
- [34] Randall T. Cygan, Jian-Jie Liang, and Andrey G. Kalinichev. Molecular Models of Hydroxide, Oxyhydroxide, and Clay Phases and the Development of a General Force Field. *The Journal of Physical Chemistry B*, 108(4):1255–1266, 2004. ISSN 1520-6106. doi: 10.1021/jp0363287. URL <http://pubs.acs.org/doi/abs/10.1021/jp0363287>.
- [35] E. Del Gado, K. Ioannidou, E. Masoero, A. Baronnet, R. J M Pellenq, F. J. Ulm, and S. Yip. A soft matter in construction approach Statistical physics approach to formation and mechanics of C-S-H gels in cement. *European Physical Journal: Special Topics*, 223(11):2285–2295, 2014. ISSN 19516401. doi: 10.1140/epjst/e2014-02264-1.
- [36] A. Delville, R. J.-M. Pellenq, and J. M. Caillol. A Monte Carlo (N,V,T) study of the stability of charged interfaces: A simulation on a hypersphere. *The Journal of Chemical Physics*, 106(17):7275–7285, 1997. ISSN 0021-9606. doi: 10.1063/1.473689. URL <http://aip.scitation.org/doi/10.1063/1.473689>.

- [37] B. Derjaguin and L.D. Landau. Theory of the Stability of Strongly Charged Lyophobic Sols and of the Adhesion of Strongly Charged Particles in Solutions of Electrolytes. *Acto Physicochimica U.R.S.S.*, 14:633–662, 1941.
- [38] Shalaka Dewan, Vincenzo Carnevale, Arindam Bankura, Ali Eftekhari-Bafrooei, Giacomo Fiorin, Michael L. Klein, and Eric Borguet. Structure of water at charged interfaces: A molecular dynamics study. *Langmuir*, 30(27):8056–8065, 2014. ISSN 15205827. doi: 10.1021/la5011055.
- [39] Chamila Chathuranga Dharmawardhana and Toshiko Ichiye. Building better water models using the shape of the charge distribution of a water molecule. *The Journal of Chemical Physics*, 147(19):194103, 2017. doi: 10.1063/1.4986070. URL <http://aip.scitation.org/doi/10.1063/1.4986070>.
- [40] Martin Ester, Hans-Peter Kriegel, Jiirg Sander, and Xiaowei Xu. A density-based algorithm for discovering clusters in large spatial databases with noise. *AAAI Press*, 226, 1996.
- [41] P.P. Ewald. Die Berechnung optischer und elektrostatischer Gitterpotentiale. *Ann. Physik*, 64:253, 1921.
- [42] Nicolas Fernandez, Roman Mani, David Rinaldi, Dirk Kadau, Martin Mosquet, H el ene Lombois-Burger, Juliette Cayer-Barrioz, Hans J. Herrmann, Nicholas D. Spencer, and Lucio Isa. Microscopic mechanism for shear thickening of non-Brownian suspensions. *Phys. Rev. Lett.*, 111:108301, 2013.
- [43] Nicolas Fernandez, Roman Mani, David Rinaldi, Dirk Kadau, Martin Mosquet, H el ene Lombois-Burger, Juliette Cayer-Barrioz, Hans J. Herrmann, Nicholas D. Spencer, and Lucio Isa. Microscopic mechanism for shear thickening of non-brownian suspensions. *Phys. Rev. Lett.*, 111:108301, Sep 2013. doi: 10.

1103/PhysRevLett.111.108301. URL <https://link.aps.org/doi/10.1103/PhysRevLett.111.108301>.

- [44] Eric Ferrage, Fabien Hubert, Alain Baronnet, Olivier Grauby, Emmanuel Tertre, Alfred Delville, Isabelle Bihannic, Dimitri Prêtt, Laurent J. Michot, and Pierre Levitz. Influence of crystal structure defects on the small-angle neutron scattering/diffraction patterns of clay-rich porous media. *Journal of Applied Crystallography*, 51(5):1311–1322, 2018. ISSN 16005767. doi: 10.1107/S160057671801052X.
- [45] Daan Frenkel and Berend Smit. *Understanding Molecular Simulation*. Academic Press, San Diego, 2nd edition, 2002.
- [46] S. Garrault, E. Finot, E. Lesniewska, and A. Nonat. Study of C-S-H growth on C3S surface during its early hydration. *Materials and Structures*, 38(278):435–442, 2005. ISSN 1359-5997. doi: 10.1617/14343. URL <https://www.rilem.net/boutique/fiche.php?cat=journal{&}reference=1843>.
- [47] Ellis M. Gartner. A proposed mechanism for the growth of C-S-H during the hydration of tricalcium silicate. *Cement and Concrete Research*, 27(5):665–672, 1997. ISSN 00088846. doi: 10.1016/S0008-8846(97)00049-5.
- [48] Nicolas Giovambattista, Peter J. Rossky, and Pablo G. Debenedetti. Phase transitions induced by nanoconfinement in liquid water. *Physical Review Letters*, 102(5):6–9, 2009. ISSN 00319007. doi: 10.1103/PhysRevLett.102.050603.
- [49] A. Gmira, M. Zabat, R. J.M. Pellenq, and H. Van Damme. Microscopic physical basis of the poromechanical behavior of cement-based materials. *Materials and Structures/Materiaux et Constructions*, 37(265):3–14, 2004. ISSN 13595997. doi: 10.1617/14101.

- [50] N Goldenfeld. *Lectures on Phase Transitions and the Renormalization Group*. Addison-Wesley, New York, NY, 1992.
- [51] Abhay Goyal, Ivan Palaia, Katerina Ioannidou, Emmanuel Trizac, Roland J.-M. Pellenq, and Emanuela Del Gado. The physics of cement cohesion. *Preprint*, 2020.
- [52] C. G. Gray, Y. S. Sainger, C. G. Joslin, P. T. Cummings, and S. Goldman. Computer simulation of dipolar fluids. Dependence of the dielectric constant on system size: A comparative study of Ewald sum and reaction field approaches. *The Journal of Chemical Physics*, 85(3):1502, 1986. ISSN 00219606. doi: 10.1063/1.451189. URL <http://scitation.aip.org/content/aip/journal/jcp/85/3/10.1063/1.451189>.
- [53] J. K. Gregory, D. C. Clary, K. Liu, M. G. Brown, and R. J. Saykally. The Water Dipole Moment in Water Clusters. *Science*, 275(5301):814–817, 1997. ISSN 00368075. doi: 10.1126/science.275.5301.814. URL <http://www.sciencemag.org/cgi/doi/10.1126/science.275.5301.814>.
- [54] A Guinier and G Fournet. *Small-angle scattering of X-rays*. Wiley, New York, 1955. doi: 10.1016/0146-3535(89)90023-3.
- [55] B. M. Guy, M. Hermes, and W. C. K. Poon. Towards a unified description of the rheology of hard-particle suspensions. *Phys. Rev. Lett.*, 115:088304, Aug 2015.
- [56] Endao Han, Matthieu Wyart, Ivo R. Peters, and Heinrich M. Jaeger. Shear fronts in shear-thickening suspensions. *Phys. Rev. Fluids*, 3:073301, Jul 2018. doi: 10.1103/PhysRevFluids.3.073301. URL <https://link.aps.org/doi/10.1103/PhysRevFluids.3.073301>.

- [57] J.-P. Hansen and I.R. McDonald. *Theory of Simple Liquids*. Academic Press, 3rd edition, 2006.
- [58] Silke Henkes and Bulbul Chakraborty. Statistical mechanics framework for static granular matter. *Physical Review E*, 79(6):061301, 2009.
- [59] Michiel Hermes, Ben M. Guy, Wilson C. K. Poon, Guilhem Poy, Michael E. Cates, and Matthieu Wyart. Unsteady flow and particle migration in dense, non-Brownian suspensions. *J. Rheol.*, 60(5):905–916, 2016.
- [60] Michiel Hermes, Ben M Guy, Wilson CK Poon, Guilhem Poy, Michael E Cates, and Matthieu Wyart. Unsteady flow and particle migration in dense, non-brownian suspensions. *Journal of Rheology*, 60(5):905–916, 2016.
- [61] Lilian C. Hsiao, Safa Jamali, Emmanouil Glynos, Peter F. Green, Ronald G. Larson, and Michael J. Solomon. Rheological state diagrams for rough colloids in shear flow. *Phys. Rev. Lett.*, 119:158001, Oct 2017. doi: 10.1103/PhysRevLett.119.158001. URL <https://link.aps.org/doi/10.1103/PhysRevLett.119.158001>.
- [62] International Energy Agency (IEA) for the Global Alliance for Buildings and Construction (GlobalABC). Global Alliance for Buildings and Construction 2018 Global Status Report. Technical report, UN Environment Programme, 2018. URL http://www.ren21.net/wp-content/uploads/2018/06/17-8652{}_GSR2018{}_FullReport{}_web{}_final{}.pdf.
- [63] Katerina Ioannidou, Roland J.-M. Pellenq, and Emanuela Del Gado. Controlling local packing and growth in calcium silicate hydrate gels. *Soft Matter*, 10(8):1121–1133, 2014. ISSN 1744-683X. doi: 10.1039/C3SM52232F. URL <http://xlink.rsc.org/?DOI=C3SM52232F>.

- [64] Katerina Ioannidou, Matej Kanduč, Lunna Li, Daan Frenkel, Jure Dobnikar, and Emanuela Del Gado. The crucial effect of early-stage gelation on the mechanical properties of cement hydrates. *Nature Communications*, 7:12106, 2016. ISSN 2041-1723. doi: 10.1038/ncomms12106. URL <http://www.nature.com/doifinder/10.1038/ncomms12106>.
- [65] Katerina Ioannidou, Konrad J. Krakowiak, Mathieu Bauchy, Christian G. Hoover, Enrico Masoero, Sidney Yip, Franz-Josef Ulm, Pierre Levitz, Roland J.-M. Pellenq, and Emanuela Del Gado. Mesoscale texture of cement hydrates. *Proceedings of the National Academy of Sciences*, 113(8):2029–2034, 2016. ISSN 0027-8424. doi: 10.1073/pnas.1520487113. URL <http://www.pnas.org/lookup/doi/10.1073/pnas.1520487113>.
- [66] Jacob Israelachvili. *Intermolecular and Surface Forces*. Academic Press, third edition, 2011. ISBN 978-0-12-375182-9.
- [67] Jacob Israelachvili and Håkan Wennerström. Role of hydration and water structure in biological and colloidal interactions, 1996. ISSN 0028-0836. URL <http://www.nature.com/doifinder/10.1038/379219a0>.
- [68] Safa Jamali and John F. Brady. Alternative frictional model for discontinuous shear thickening of dense suspensions: Hydrodynamics. *Phys. Rev. Lett.*, 123:138002, Sep 2019. doi: 10.1103/PhysRevLett.123.138002. URL <https://link.aps.org/doi/10.1103/PhysRevLett.123.138002>.
- [69] D. J. Jeffrey. The calculation of the low Reynolds number resistance functions for two unequal spheres. *Phys. Fluids A*, 4:16–29, 1992.

- [70] Y. S. Jho, R. Brewster, S. A. Safran, and P. A. Pincus. Long-range interaction between heterogeneously charged membranes. *Langmuir*, 27(8):4439–4446, 2011. ISSN 07437463. doi: 10.1021/la1050282.
- [71] Scott Jones. No Title. *Private Communication*, 2020.
- [72] B Jönsson, H Wennerström, and B Halle. Ion distribution in lamellar liquid crystals. A comparison between Monte Carlo simulations and solutions of the Poisson-Boltzmann equation. *J. Phys. Chem.*, 84:2179–2185, 1980.
- [73] B. Jönsson, H. Wennerström, A. Nonat, and B. Cabane. Onset of cohesion in cement paste. *Langmuir*, 20(16):6702–6709, 2004. ISSN 07437463. doi: 10.1021/la0498760.
- [74] Bo Jonsson, A Nonat, C Labbez, B Cabane, and H Wennerstrom. Controlling the Cohesion of Cement Paste. *Langmuir*, 21(20):9211–9221, 2005. doi: 10.1021/la051048z.
- [75] Gunnar Karlström, Joakim Stenhammar, and Per Linse. Effects of different boundary conditions on the long-range structure of polar liquids. *Journal of Physics Condensed Matter*, 20(49), 2008. ISSN 09538984. doi: 10.1088/0953-8984/20/49/494204.
- [76] S. Koneshan, Jayendran C. Rasaiah, R. M. Lynden-Bell, and S. H. Lee. Solvent Structure, Dynamics, and Ion Mobility in Aqueous Solutions at 25 ÅC. *The Journal of Physical Chemistry B*, 102(21):4193–4204, 1998. ISSN 1520-6106. doi: 10.1021/jp980642x. URL <http://pubs.acs.org/doi/abs/10.1021/jp980642x>.
- [77] Christophe Labbez, Bo Jönsson, Isabelle Pochard, André Nonat, and Bernard Cabane. Surface charge density and electrokinetic potential of highly charged

minerals: Experiments and Monte Carlo simulations on calcium silicate hydrate. *Journal of Physical Chemistry B*, 110(18):9219–9230, 2006. ISSN 15206106. doi: 10.1021/jp057096+.

- [78] Samuel Lesko, Eric Lesniewska, André Nonat, Jean Claude Mutin, and Jean Pierre Goudonnet. Investigation by atomic force microscopy of forces at the origin of cement cohesion. *Ultramicroscopy*, 86(1-2):11–21, 2001. ISSN 03043991. doi: 10.1016/S0304-3991(00)00091-7.
- [79] Pierre Levitz and D Tchoubar. Disordered porous solids : from chord distributions to small angle scattering. *Journal de Physique I*, 2(6):771–790, jun 1992. ISSN 1155-4304. doi: 10.1051/jp1:1992174. URL <http://www.edpsciences.org/10.1051/jp1:1992174>.
- [80] D. Lootens, P. Hébraud, E. Lécolier, and H. Van Damme. Gelation, shear-thinning and shear-thickening in cement slurries. *Oil and Gas Science and Technology*, 59(1):31–40, 2004. ISSN 12944475. doi: 10.2516/ogst:2004004.
- [81] Barbara Lothenbach and Frank Winnefeld. Thermodynamic modelling of the hydration of Portland cement. *Cement and Concrete Research*, 36(2):209–226, 2006. ISSN 00088846. doi: 10.1016/j.cemconres.2005.03.001.
- [82] S. Luding. Cohesive, frictional powders: contact models for tension. *Granular Matter*, 10:235–246, 2008.
- [83] R. Mari, R. Seto, J. F Morris, and M. M. Denn. Shear thickening, frictionless and frictional rheologies in non-brownian suspensions. *Journal of Rheology*, 58(6):1693–1724, 2014.

- [84] Romain Mari, Ryohei Seto, Jeffrey F. Morris, and Morton M. Denn. Shear thickening, frictionless and frictional rheologies in non-Brownian suspensions. *J. Rheol.*, 58(6):1693–1724, 2014.
- [85] Romain Mari, Ryohei Seto, Jeffrey F. Morris, and Morton M. Denn. Shear thickening, frictionless and frictional rheologies in non-brownian suspensions. *Journal of Rheology*, 58(6):1693–1724, 2014. doi: 10.1122/1.4890747. URL <https://doi.org/10.1122/1.4890747>.
- [86] Romain Mari, Ryohei Seto, Jeffrey F. Morris, and Morton M. Denn. Nonmonotonic flow curves of shear thickening suspensions. *Phys. Rev. E*, 91(5):052302, May 2015. doi: 10.1103/PhysRevE.91.052302.
- [87] Pekka Mark and Lennart Nilsson. Structure and Dynamics of the TIP3P , SPC , and SPC / E Water Models at 298 K. *The Journal of Physical Chemistry A*, 105(43):9954–9960, 2001. ISSN 1089-5639. doi: 10.1021/jp003020w. URL <http://pubs.acs.org/doi/abs/10.1021/jp003020w>.
- [88] C. M. Marques and M. E. Cates. Hexagonal and lamellar mesophases induced by shear . *J. Phys. France*, 51:1733–1747, 1990. doi: 10.1051/jphys:0199000510160173300.
- [89] Saeed Masoumi, Hamid Valipour, and Mohammad Javad Abdolhosseini Qomi. Intermolecular Forces between Nanolayers of Crystalline Calcium-Silicate-Hydrates in Aqueous Medium. *Journal of Physical Chemistry C*, 121(10):5565–5572, 2017. ISSN 19327455. doi: 10.1021/acs.jpcc.6b10735.
- [90] Saeed Masoumi, Siavash Zare, Hamid Valipour, and Mohammad Javad Abdolhosseini Qomi. Effective Interactions between Calcium-Silicate-Hydrate Nanolayers.

Journal of Physical Chemistry C, 123(8):4755–4766, 2019. ISSN 19327455. doi: 10.1021/acs.jpcc.8b08146.

- [91] J Mewis and Norman Joseph Wagner. *Colloidal suspension rheology*. Cambridge series in chemical engineering. Cambridge University Press, Cambridge, 2012. ISBN 9780521515993. URL <http://www.loc.gov/catdir/enhancements/fy1214/2011029383-t.html>.
- [92] R. Sh. Mikhail, L. E. Copeland, and Stephen Brunauer. Pore structures and surface areas of hardened portland cement pastes by Nitrogen adsorption. *Can J Chem*, 42(2):426–438, 1964.
- [93] Paramita Mondal, Surendra R. Shah, and Laurence D. Marks. Nanoscale characterization of cementitious materials. *ACI Materials Journal*, 105(2):174–179, 2008. ISSN 0889325X. doi: 10.1007/978-3-319-17088-6_5.
- [94] Joseph Monti, Patricia Marie McGuiggan, and Mark O. Robbins. Effect of roughness and elasticity on interactions between charged colloidal spheres. *Langmuir*, 0(ja): null, 0. doi: 10.1021/acs.langmuir.9b02161. URL <https://doi.org/10.1021/acs.langmuir.9b02161>. PMID: 31574219.
- [95] André G. Moreira and Roland R. Netz. Binding of similarly charged plates with counterions only. *Physical Review Letters*, 87(7):78301–1–78301–4, 2001. ISSN 10797114. doi: 10.1103/PhysRevLett.87.078301.
- [96] Christopher Ness and Jin Sun. Shear thickening regimes of dense non-Brownian suspensions. *Soft Matter*, 12(3):914–924, 2016.

- [97] André Nonat. The structure and stoichiometry of C-S-H. *Cement and Concrete Research*, 34(9):1521–1528, 2004. ISSN 00088846. doi: 10.1016/j.cemconres.2004.04.035.
- [98] John F. Ouyang and Ryan P. A. Bettens. Modelling Water: A Life-time Enigma. *CHIMIA International Journal for Chemistry*, 69(3):104–111, 2015. ISSN 00094293. doi: 10.2533/chimia.2015.104. URL <http://openurl.ingenta.com/content/xref?genre=article&issn=0009-4293&volume=69&issue=3&spage=104>.
- [99] Ivan Palaia. *Charged systems in, out of, and driven to equilibrium : from nanocapacitors to cement*. PhD thesis, University Paris-Saclay, 2019.
- [100] Sungham Park, David E Moilanen, and M D Fayer. Water Dynamics-The Effects of Ions and Nanoconfinement. *J. Phys. Chem. B*, 112:5279–5290, 2008.
- [101] R. J.-M. Pellenq, J. M. Caillol, and A. Delville. Electrostatic Attraction between Two Charged Surfaces: A (N,V,T) Monte Carlo Simulation. *The Journal of Physical Chemistry B*, 101(42):8584–8594, 1997. ISSN 1520-6106. doi: 10.1021/jp971273s. URL <http://dx.doi.org/10.1021/jp971273s> <http://pubs.acs.org/doi/full/10.1021/jp971273s> <http://pubs.acs.org/doi/pdf/10.1021/jp971273s>.
- [102] R. J.M. Pellenq, N. Lequeux, and H. van Damme. Engineering the bonding scheme in C-S-H: The iono-covalent framework. *Cement and Concrete Research*, 38(2): 159–174, 2008. ISSN 00088846. doi: 10.1016/j.cemconres.2007.09.026.
- [103] R. J.M. M Pellenq and P. E. Levitz. Capillary condensation in a disordered mesoporous medium: a grand canonical Monte Carlo study. *Molecular Physics*, 100(13): 2059–2077, 2002. ISSN 00268976. doi: 10.1080/00268970210129265.

- [104] Roland J.-M. Pellenq and David Nicholson. Intermolecular Potential Function for the Physical Adsorption of Rare Gases in Silicalite. *The Journal of Physical Chemistry*, 98(50):13339–13349, 1994. ISSN 0022-3654. doi: 10.1021/j100101a039. URL <http://pubs.acs.org/doi/abs/10.1021/j100101a039>.
- [105] Roland J.-M. Pellenq and Henri Van Damme. Why Does Concrete Set?: The Nature of Cohesion Forces in Hardened Cement-Based Materials. *MRS Bulletin*, 29(05): 319–323, 2004. ISSN 0883-7694. doi: 10.1557/mrs2004.97. URL http://www.journals.cambridge.org/abstract_{_}S0883769400015384.
- [106] Roland J.-M. Pellenq, Akihiro Kushima, Rouzbeh Shahsavari, Krystyn J Van Vliet, Markus J Buehler, Sidney Yip, and Franz-Josef Ulm. A realistic molecular model of cement hydrates. *Proceedings of the National Academy of Sciences of the United States of America*, 106(38):16102–16107, 2009. ISSN 0027-8424. doi: 10.1073/pnas.0902180106.
- [107] Cedric Plassard, Eric Lesniewska, Isabelle Pochard, and André Nonat. Nanoscale Experimental Investigation of Particle Interactions at the Origin of the Cohesion of Cement. *Langmuir*, 21(16):7263–7270, 2005.
- [108] S. Plimpton. Fast Parallel Algorithms for Short-Range Molecular Dynamics. *Journal of Computational Physics*, 117(June 1994):1–19, 1995. ISSN 00219991. doi: 10.1006/jcph.1995.1039. URL <http://lammps.sandia.gov>.
- [109] T.C. Powers. Structure and Physical Properties of Hardened Portland Cement Paste. *Journal of the American Ceramic Society*, 41(1):1–6, 1958. ISSN 1551-2916. doi: 10.1111/j.1151-2916.1958.tb13494.x. URL <http://dx.doi.org/10.1111/j.1151-2916.1958.tb13494.x>.

- [110] Elizaveta Pustovgar, Rahul P. Sangodkar, Andrey S. Andreev, Marta Palacios, Bradley F. Chmelka, Robert J. Flatt, and Jean-Baptiste d’Espinose de Lacaillerie. Understanding silicate hydration from quantitative analyses of hydrating tricalcium silicates. *Nature Communications*, 7:10952, 2016. ISSN 2041-1723. doi: 10.1038/ncomms10952. URL <http://www.nature.com/doifinder/10.1038/ncomms10952>.
- [111] Kabir Ramola and Bulbul Chakraborty. Stress response of granular systems. *Journal of Statistical Physics*, 169(1):1–17, 2017.
- [112] Vikram Rathee, Daniel L. Blair, and Jeffrey S. Urbach. Localized stress fluctuations drive shear thickening in dense suspensions. *Proceedings of the National Academy of Sciences*, 114(33):8740–8745, 2017. ISSN 0027-8424. doi: 10.1073/pnas.1703871114. URL <https://www.pnas.org/content/114/33/8740>.
- [113] Vikram Rathee, Daniel L. Blair, and Jeffrey S. Urbach. Localized transient jamming in discontinuous shear thickening, 2019.
- [114] R. Renou, A. Szymczyk, and A. Ghoufi. Tunable dielectric constant of water at the nanoscale. *Physical Review E - Statistical, Nonlinear, and Soft Matter Physics*, 91(3):1–6, 2015. ISSN 15502376. doi: 10.1103/PhysRevE.91.032411.
- [115] I. G. Richardson. Nature of C-S-H in hardened cements. *Cement and Concrete Research*, 29(8):1131–1147, 1999. ISSN 00088846. doi: 10.1016/S0008-8846(99)00168-4.
- [116] Ioulia Rouzina and Victor a. Bloomfield. Macroion Attraction Due to Electrostatic Correlation between Screening Counterions. 1. Mobile Surface-Adsorbed Ions and Diffuse Ion Cloud. *The Journal of Physical Chemistry*, 100(23):9977–9989, 1996.

ISSN 0022-3654. doi: 10.1021/jp960458g. URL <http://pubs.acs.org/doi/abs/10.1021/jp960458g>.

- [117] John R Royer, Daniel L Blair, and Steven D Hudson. Rheological signature of frictional interactions in shear thickening suspensions. *Physical review letters*, 116(18): 188301, 2016.
- [118] Brice Saint-Michel, Thomas Gibaud, and Sébastien Manneville. Uncovering instabilities in the spatiotemporal dynamics of a shear-thickening cornstarch suspension. *Phys. Rev. X*, 8:031006, Jul 2018. doi: 10.1103/PhysRevX.8.031006. URL <https://link.aps.org/doi/10.1103/PhysRevX.8.031006>.
- [119] Ladislav Šamaj and Emmanuel Trizac. Ground state of classical bilayer Wigner crystals. *Epl*, 98(3), 2012. ISSN 02955075. doi: 10.1209/0295-5075/98/36004.
- [120] Ladislav Samaj, Martin Trulsson, and Emmanuel Trizac. Strong-coupling theory of counterions between symmetrically charged walls: from crystal to fluid phases. *Soft Matter*, 14:4040–4052, 2018. doi: 10.1039/c8sm00571k.
- [121] S. Sarkar, E. Shatoff, K. Ramola, R. Mari, J. Morris, and B. Chakraborty. Shear-induced organization of forces in dense suspensions: signatures of discontinuous shear thickening. *EPJ Web of Conferences*, 140, 09045, 2017.
- [122] Sumantra Sarkar, Dapeng Bi, Jie Zhang, RP Behringer, and Bulbul Chakraborty. Origin of rigidity in dry granular solids. *Physical review letters*, 111(6):068301, 2013.
- [123] Alexander Schlaich, Ernst W. Knapp, and Roland R. Netz. Water Dielectric Effects in Planar Confinement. *Physical Review Letters*, 117(4):1–5, 2016. ISSN 10797114. doi: 10.1103/PhysRevLett.117.048001.

- [124] Francesco Sciortino, Alfons Geiger, and H. Eugene Stanley. Effect of defects on molecular mobility in liquid water. *Nature*, 354(6350):218–221, 1991. ISSN 0028-0836. doi: 10.1038/354218a0.
- [125] Christian Sendner, Dominik Horinek, Lyderic Bocquet, and Roland R. Netz. Interfacial water at hydrophobic and hydrophilic surfaces: Slip, viscosity, and diffusion. *Langmuir*, 25(18):10768–10781, 2009. ISSN 07437463. doi: 10.1021/la901314b.
- [126] Ryohei Seto, Romain Mari, Jeffrey F. Morris, and Morton M. Denn. Discontinuous shear thickening of frictional hard-sphere suspensions. *Phys. Rev. Lett.*, 111:218301, 2013.
- [127] Ryohei Seto, Abhinendra Singh, Bulbul Chakraborty, Morton M. Denn, and Jeffrey F. Morris. Shear jamming and fragility in dense suspensions. *Granular Matter*, 21(3):1–8, 2019. ISSN 14347636. doi: 10.1007/s10035-019-0931-5. URL <https://doi.org/10.1007/s10035-019-0931-5>.
- [128] A. Singh, S. Pednekar, J. Chun, M. M Denn, and J. F Morris. From yielding to shear jamming in a cohesive frictional suspension. *Physical Rev. Lett.*, 122(9):098004, 2019.
- [129] Abhinendra Singh, Vanessa Magnanimo, Kuniyasu Saitoh, and Stefan Luding. The role of gravity or pressure and contact stiffness in granular rheology. *New J. Phys.*, 17(4):043028, 2015.
- [130] Abhinendra Singh, Romain Mari, Morton M Denn, and Jeffrey F Morris. A constitutive model for simple shear of dense frictional suspensions. *Journal of Rheology*, 62(2):457–468, 2018.

- [131] E R Smith. Electrostatic Energy in Ionic Crystals. *Proceedings of the Royal Society of London. Series A, Mathematical and Physical Sciences*, 375(1763):475–505, 1981. ISSN 00804630. doi: 10.2307/2990334. URL <http://www.jstor.org/stable/2990334>.
- [132] Michiel Sprik. Hydrogen bonding and the static dielectric constant in liquid water. *The Journal of Chemical Physics*, 95(9):6762–6769, 1991. ISSN 00219606. doi: 10.1063/1.461515. URL <http://link.aip.org/link/JCPA6/v95/i9/p6762/s1?Agg=doi>.
- [133] Paul J. Steinhardt, David R. Nelson, and Marco Ronchetti. Bond-orientational order in liquids and glasses. *Physical Review B*, 28(2):784–805, 1983. ISSN 01631829. doi: 10.1103/PhysRevB.28.784.
- [134] M. J. Stevens and M. O. Robbins. Density functional theory of ionic screening when do like charges attract. *Epl*, 12(1):81–86, 1990. ISSN 12864854. doi: 10.1209/0295-5075/12/1/015.
- [135] Yuya Suda, Tatsuhiko Saeki, and Tsuyoshi Saito. Relation between chemical composition and physical properties of C-S-H generated from cementitious materials. *Journal of Advanced Concrete Technology*, 13(5):275–290, 2015. ISSN 13468014. doi: 10.3151/jact.13.275.
- [136] I. M. Svishchev and P. G. Kusalik. Dynamics in liquid water, water-d₂, and water-t₂: a comparative simulation study. *The Journal of Physical Chemistry*, 98(3):728–733, 2005. ISSN 0022-3654. doi: 10.1021/j100054a002.
- [137] K T Tang. Upper and lower bounds of two- and three-body dipole, quadrupole, and octupole van der Waals coefficients for hydrogen, noble gas, and alkali atom interactions. *The Journal of Chemical Physics*, 64(7):3063, 1976. ISSN 00219606. doi:

10.1063/1.432569. URL <http://scitation.aip.org/content/aip/journal/jcp/64/7/10.1063/1.432569>.

- [138] H.F.W. Taylor. *Cement Chemistry*. Thomas Telford, London, 1997.
- [139] Paul D. Tennis and Hamlin M. Jennings. Model for two types of calcium silicate hydrate in the microstructure of Portland cement pastes. *Cement and Concrete Research*, 30(6):855–863, 2000. ISSN 00088846. doi: 10.1016/S0008-8846(00)00257-X.
- [140] O. Teschke, G. Ceotto, and E. F. de Souza. Interfacial water dielectric-permittivity-profile measurements using atomic force microscopy. *Physical Review E - Statistical Physics, Plasmas, Fluids, and Related Interdisciplinary Topics*, 64(1):10, 2001. ISSN 1063651X. doi: 10.1103/PhysRevE.64.011605.
- [141] Jeffrey J. Thomas, Hamlin M. Jennings, and Jeffrey J. Chen. Influence of nucleation seeding on the hydration mechanisms of tricalcium silicate and cement. *Journal of Physical Chemistry C*, 113(11):4327–4334, 2009. ISSN 19327447. doi: 10.1021/jp809811w.
- [142] Jetin E. Thomas, Kabir Ramola, Abhinendra Singh, Romain Mari, Jeffrey F. Morris, and Bulbul Chakraborty. Microscopic origin of frictional rheology in dense suspensions: Correlations in force space. *Phys. Rev. Lett.*, 121:128002, Sep 2018. doi: 10.1103/PhysRevLett.121.128002. URL <https://link.aps.org/doi/10.1103/PhysRevLett.121.128002>.
- [143] Jetin E Thomas, Abhay Goyal, Deshpreet Singh Bedi, Abhinendra Singh, and Emanuela Del Gado. Investigating the Nature of Discontinuous Shear Thickening : Beyond a Mean-Field Description. 329:1–13, 2020. doi: 10.1122/1.5132317.

- [144] J.J. Thomas, H.M. Jennings, and a.J. Allen. the Surface Area of Cement Paste As Measured By Neutron. *Cement and Concrete Research*, 28(6):897–905, 1998.
- [145] J.J. Thomas, H.M. Jennings, and A.J. Allen. The surface area of hardened cement paste as measured by various techniques. *Concrete Science and Engineering*, 1 (March):45–64, 1999. ISSN 00088846. doi: 10.1016/S0008-8846(98)00049-0.
- [146] Aidan P. Thompson, Steven J. Plimpton, and William Mattson. General formulation of pressure and stress tensor for arbitrary many-body interaction potentials under periodic boundary conditions. *Journal of Chemical Physics*, 131(15):1–6, 2009. ISSN 00219606. doi: 10.1063/1.3245303.
- [147] Brian P Tighe, Adrienne RT van Eerd, and Thijs JH Vlugt. Entropy maximization in the force network ensemble for granular solids. *Physical review letters*, 100(23): 238001, 2008.
- [148] M. Vandamme and F.-J. Ulm. Nanogranular origin of concrete creep. *Proceedings of the National Academy of Sciences*, 106(26):10552–10557, 2009. ISSN 0027-8424. doi: 10.1073/pnas.0901033106. URL <http://www.pnas.org/cgi/doi/10.1073/pnas.0901033106>.
- [149] E.J.W. Verwey and J.Th.G. Overbeek. *Theory of the stability of lyophobic colloids*. Elsevier, Amsterdam, 1948.
- [150] B. Widom. Some Topics in the Theory of Fluids. *The Journal of Chemical Physics*, 39(11):2808–2812, 1963. ISSN 0021-9606. doi: 10.1063/1.1734110.
- [151] E. Wigner. On the interaction of electrons in metals. *Physical Review*, 46(11):1002–1011, 1934. ISSN 0031899X. doi: 10.1103/PhysRev.46.1002.

- [152] Douglas N. Winslow, John M. Bukowski, and J. Francis Young. The early evolution of the surface of hydrating cement. *Cement and Concrete Research*, 24(6):1025–1032, 1994. ISSN 00088846. doi: 10.1016/0008-8846(94)90025-6.
- [153] Matthieu Wyart and ME Cates. Discontinuous shear thickening without inertia in dense non-brownian suspensions. *Physical review letters*, 112(9):098302, 2014.
- [154] In-Chul Yeh and Max L. Berkowitz. Ewald summation for systems with slab geometry. *The Journal of Chemical Physics*, 111(7):3155–3162, 1999. ISSN 0021-9606. doi: 10.1063/1.479595. URL <http://aip.scitation.org/doi/10.1063/1.479595>.
- [155] Ronen Zangi. Water confined to a slab geometry: a review of recent computer simulation studies. *Journal of Physics: Condensed Matter*, 16(45):S5371–S5388, 2004. ISSN 0953-8984. doi: 10.1088/0953-8984/16/45/005. URL <http://stacks.iop.org/0953-8984/16/i=45/a=005?key=crossref.76c65ed66412e8c3cd07bed2a9f2587f>.
- [156] Yuan Zhuang, Kai Zhang, and Patrick Charbonneau. Equilibrium Phase Behavior of a Continuous-Space Microphase Former. *Physical Review Letters*, 116(9):1–5, 2016. ISSN 10797114. doi: 10.1103/PhysRevLett.116.098301.